

University of Alberta

Micromechanical Study of Borehole Breakout Mechanism

by

Hossein Rahmati

A thesis submitted to the Faculty of Graduate Studies and Research
in partial fulfillment of the requirements for the degree of

Doctor of Philosophy

in

Petroleum Engineering

Department of Civil and Environmental Engineering

©Hossein Rahmati

Spring 2013

Edmonton, Alberta

Permission is hereby granted to the University of Alberta Libraries to reproduce single copies of this thesis and to lend or sell such copies for private, scholarly or scientific research purposes only. Where the thesis is converted to, or otherwise made available in digital form, the University of Alberta will advise potential users of the thesis of these terms.

The author reserves all other publication and other rights in association with the copyright in the thesis and, except as herein before provided, neither the thesis nor any substantial portion thereof may be printed or otherwise reproduced in any material form whatsoever without the author's prior written permission.

Dedication

To my parents

Abstract

Borehole breakouts are zones of enlargements of the wellbore cross section that form as a result of rock failure at the wellbore wall during drilling. The analysis of borehole breakout is essential in addressing wellbore stability, well completion, and sand production problems.

This research numerically investigates the effect of the material micro and macro-parameters on the failure mechanism and the geometry of the wellbore breakout. A three-dimensional discrete element method was used in the simulations.

In this research, a systematic methodology was developed for calibrating material micro-properties. Next, the calibration performance was assessed by simulating thick walled cylinder tests and comparing the model results against laboratory measurements. The model was also verified against analytical solutions for a TWC sample under plane strain axisymmetric conditions.

The numerical tool was then used in a series of parametric simulations of drilling conditions. These simulations allowed the relating of the breakout type to the sandstone's micro-properties. To be able to relate the breakout type to the macro-mechanical properties, a series of triaxial testing simulations were conducted to relate the micro and macro-mechanical material properties together.

The results showed that the geometry of the breakout was affected by micro-parameters such as the particle contact modulus, the parallel bond normal and shear strengths, the particle crushing strength, and the particle size distribution. In

addition, it was found that the macro Young's modulus, friction and dilation angles, and the uniaxial compressive strength also affect the type of breakouts.

The triaxial testing simulations showed that: (a) Young's modulus is not just affected by the particle contact modulus, but also the friction coefficient between particles and the percentage of bonded contacts, (b) the dilation angle is a function of the particle contact modulus, percentage of bonded contacts and inter-particle friction, (c) the friction angle is not only affected by the friction coefficient between particles, but also by bond strengths, (d) cohesion is not just affected by bond strengths and the percentage of bonded contacts, but also by the friction coefficient between particles, and (e) the post-peak modulus is affected by the percentage of bonded contacts and inter-particle friction.

Acknowledgments

I sincerely thank my parents and brothers for their love, devotion, and continued encouragement to gain further education.

I am very thankful to my supervisor, Dr. Alireza Nouri, for having faith in me, for giving me an opportunity to work on this project, for all of his encouragement and support, and for granting me freedom to explore my ideas.

I wish to extend my deep gratitude to Dr. Dave Chan for the many interesting technical discussions I had with him over the course of this project and for his advice and feedback. I would like also to express my sincere thanks to Dr. Hans Vaziri from BP America for sharing his experience and expertise in this area and also for providing laboratory data.

I would also like to thank all of my committee members, Dr. Jozef Szymanski, Dr. Derek Apel, Dr. Japan Trivedi, Dr. Chong-Qing Ru, and Dr. John McLennan, for their valuable suggestions to improve my thesis.

I would like to acknowledge NSERC for providing the funding for this research through their Discovery Grants Program as well as the financial support provided by the FS Chia PhD Scholarship. I also thank BP for their technical advice and for providing and permitting the publication of their laboratory data.

Finally, I would like to thank all those who collaborated with me throughout my research.

Table of Contents

Chapter 1: General introduction.....	1
1.1 Introduction	1
1.2 Problem statement	3
1.3 Research objectives	4
1.4 Thesis layout	5
1.5 Significance of the work	6
Chapter 2: A review of borehole breakout prediction methods	8
2.1 Introduction	8
2.1.1 Rock disaggregation mechanisms.....	8
2.1.2 Morphology of cavity growth	9
2.2 Factors affecting the failure morphology around the borehole	11
2.2.1 Material properties	11
2.2.2 Size effect.....	13
2.2.3 Far-field stress anisotropy.....	13
2.2.4 Fluid flow	14
2.3 Numerical modeling of borehole breakout.....	16
2.3.1 Numerical models based on a continuum approach	16
2.3.2 Numerical models based on a discontinuum approach.....	19
2.4 Conclusions	20
Chapter 3: Discrete Element Method.....	21
3.1 Introduction	21
3.2 Distinct Element Method (DEM).....	21
3.2.1 Force-displacement law	23

3.2.2	Law of motion.....	29
3.3	Mechanical time step determination.....	31
3.4	Mechanical damping	32
3.5	Contact models.....	32
3.5.1	Linear contact model.....	32
3.5.2	Parallel bond model	33
3.6	Interpretation techniques	37
3.6.1	Coordination number	37
3.6.2	Porosity	37
3.6.3	Stress	38
3.6.4	Strain rate	40
3.7	Initial and boundary conditions.....	40
3.8	Relationship between micro-parameters of the parallel bond model and actual micro-properties	42
3.9	Conclusions	42
Chapter 4: Systematic calibration procedure for DEM parallel bond models		44
4.1	Introduction	44
4.2	Calibration process	46
4.2.1	Specimen generation.....	47
4.2.2	Calibration of the micromechanical parameters	49
4.3	Triaxial test simulation.....	50
4.4	Verification of the calibration process	57
4.5	Validation of the calibration by simulating the TWC response	60
4.6	Uniqueness of the calibration.....	62
4.6.1	Effect of particle contact modulus and parallel bond modulus (E_c and E_{pb}).....	63

4.6.2	Effect of percentage of bonded contacts (λ)	65
4.6.3	Effect of bond strengths	66
4.6.4	Effect of friction between particles (μ)	69
4.6.5	Effect of radius multiplier (α)	70
4.6.6	Effect of $\frac{K^N}{K^S}$ and $\frac{K_{pb}^N}{K_{pb}^S}$	71
4.7	Suggested procedure for calibration of micro-properties.....	72
4.8	Conclusions	74
Chapter 5: Simulation of drilling induced compaction bands using Discrete Element Method.....		76
5.1	Introduction	76
5.2	The grain crushing modeling scheme.....	77
5.3	The numerical modeling case.....	79
5.3.1	Verification of the DEM model	81
5.4	Numerical results.....	84
5.5	Borehole breakout at isotropic stress conditions.....	91
5.6	Conclusions	95
Chapter 6: The relationship between the rock macro- and micro-properties and wellbore breakout type.....		97
6.1	Introduction	97
6.2	Numerical model	97
6.3	Numerical results.....	99
6.3.1	Effect of particle contact modulus (E_c).....	100
6.3.2	Effect of cement strength	103
6.3.3	Effect of the percentage of bonded contacts (λ)	106
6.3.4	Effect of the friction coefficient between particles (μ).....	108

6.3.5	Effect of particle crushing strength.....	112
6.3.6	Effect of porosity	112
6.3.7	Discussion.....	113
6.4	Conclusions	115
Chapter 7: Conclusion.....		118
7.1	DEM sandstone model development and calibration.....	118
7.2	DEM model development for the simulation of borehole breakouts ...	118
7.3	Micromechanical study of borehole breakout mechanism.....	119
7.4	Recommendations for future work.....	120
Bibliography		122
Appendix A: Analytical expressions for the stresses around a wellbore		133
A.1	Analytical solutions for the effective stresses	133
A.2	Analytical solutions for the stresses around a wellbore developed by Risnes et al. (1982)	133
Appendix B: Summary of 3D DEM calibration for Castlegate sandstone		136
B.1	Calibration process	137
B.2	Triaxial test simulation.....	139
Appendix C: The evaluation of macromechanical properties for the base case .		141
C.1	Elastic properties	141
C.2	Plastic properties	142

List of Tables

Table 2.1 Failure patterns associated with material properties	13
Table 4.1 Calibrated micro-parameters for the SWS sandstone DEM model	50
Table 4.2 Elastic properties assessed from the laboratory data and the DEM model	53
Table 4.3 Plastic properties assessed from the laboratory data and the DEM model	53
Table 4.4 Simulation investigating the effect of bond strengths.....	67
Table 5.1 Calibrated micro-parameters for the Castlegate sandstone DEM model	80
Table 6.1 Mechanical properties for the base case	98
Table 6.2 Mechanical properties for investigating the effect of E_c	102
Table 6.3 Simulation investigating the effect of bond strengths.....	103
Table 6.4 Mechanical properties for investigating the effect of bond strengths.	105
Table 6.5 Mechanical properties for investigating the effect of the percentage of bonded contacts.....	108
Table 6.6 Mechanical properties for investigating the effect of the friction coefficient between particles.....	111
Table B.1 Calibrated micro-parameters for the Castlegate sandstone DEM model	139

List of Figures

Figure 1.1 Borehole breakout (Guenot, 1989)	1
Figure 2.1 Shear bands around a hole	9
Figure 2.2 Failure pattern of the hole in hollow cylinder sand production tests: (a) uniform hole failure, (b) V-shaped breakout, and (c) fracture-like breakout (Lavrov et al., 2005).....	11
Figure 2.3 Failure pattern of the hole in perforation test (Tronvol and Fjaer, 1994)	15
Figure 3.1 DEM calculation flow chart (Itasca, 2008)	22
Figure 3.2 Ball-ball contact (Itasca, 2008).....	24
Figure 3.3 Ball-wall contact (Itasca, 2008).....	25
Figure 3.4 Determination of normal direction for ball-wall contact (Itasca, 2008)	26
Figure 3.5 Parallel bond representation (Itasca, 2008)	34
Figure 4.1 Stress-strain curves for SWS sandstone at different confining stresses	46
Figure 4.2 Comparison between the actual SWS PSD and the DEM specimen PSD	47
Figure 4.3 Triaxial test specimen	49
Figure 4.4 SWS sandstone micro-properties	50
Figure 4.5 Comparison between triaxial data and numerical simulations	52
Figure 4.6 The number of parallel bonds that fail in either tension or shear at different confining stresses	56
Figure 4.7 Vertical cross section of the specimen failure patterns	56
Figure 4.8 Vertical cross section of the specimen at residual strength.....	57
Figure 4.9 The bilinear yield function for the SWS sandstone.....	59
Figure 4.10 Comparison of the stresses around the wellbore between the DEM model and the analytical solution developed by Risnes et al. (1982).....	59
Figure 4.11 Coordination number around the hole.....	60
Figure 4.12 Comparison between TWC laboratory data and the numerical simulation.....	61

Figure 4.13 Failure pattern around the hole in TWC test for the SWS sandstone	62
Figure 4.14 Sensitivity of the macro response to E_{pb}	63
Figure 4.15 Sensitivity of the macro response to E_c	64
Figure 4.16 The impact of the particle contact and parallel bond moduli on dilation angle	64
Figure 4.17 Sensitivity of response to the percentage of bonded contacts	65
Figure 4.18 The impact of the percentage of bonded contacts on Poisson's ratio	66
Figure 4.19 The impact of the percentage of bonded contacts on dilation angle	66
Figure 4.20 Sensitivity of response to normal bond strength	67
Figure 4.21 Sensitivity of response to shear bond strength	68
Figure 4.22 Sensitivity of volumetric strain to bond strengths	69
Figure 4.23 Sensitivity of response to inter-particle friction	70
Figure 4.24 Sensitivity of response to radius multiplier (α)	71
Figure 4.25 The impact of ratio of the normal to shear stiffness of the particles and cement on Poisson's ratio	72
Figure 5.1 Comparison between the actual Castlegate PSD and the DEM specimen PSD	80
Figure 5.2 Comparison of the stresses at the wellbore wall between the DEM model and the analytical solution developed by Zoback (2007)	82
Figure 5.3 Comparison of the stresses around the wellbore between the DEM model and the analytical solutions developed by Risnes et al. (1982)	83
Figure 5.4 Borehole cross section of Castlegate sandstone showing a fracture-like breakout ($\sigma_v=30$ MPa)	85
Figure 5.5 Density of broken bonds within the compaction band ($\sigma_h=20$ MPa, $\sigma_v=30$ MPa, $\sigma_H=50$ MPa)	86
Figure 5.6 The MC failure criterion for Castlegate sandstone and the state of stress inside the breakout	87
Figure 5.7 Borehole cross section of Castlegate sandstone at different far-field stresses (a) $\sigma_h=20$ MPa, $\sigma_v=30$ MPa, $\sigma_H=45$ MPa (b) $\sigma_h=20$ MPa, $\sigma_v=30$ MPa, $\sigma_H=60$ MPa (c) $\sigma_h=30$ MPa, $\sigma_v=35$ MPa, $\sigma_H=50$ MPa	87

Figure 5.8 Variation of normalized breakout length (L/r) in Castlegate sandstone as a function of σ_H/σ_h	88
Figure 5.9 Variation of micro cracks and crushed grains as function of mean stress and stress anisotropy	89
Figure 5.10 Variation of micro cracks and crushed grains as function of stress anisotropy and mean stress	90
Figure 5.11 Borehole cross section of Castlegate sandstone with pre-existing cracks under isotropic stress conditions.....	92
Figure 5.12 Borehole cross section of Castlegate sandstone without the flaw under isotropic stress conditions	93
Figure 5.13 Borehole cross section under anisotropic stress conditions showing a V-shaped breakout ($\sigma_v=30$ MPa)	93
Figure 5.14 Borehole cross section under isotropic stress conditions showing a V-shaped breakout	94
Figure 5.15 Borehole cross section without pre-existing flaws under isotropic stress conditions	95
Figure 6.1 Borehole cross section of Castlegate sandstone (base case) showing fracture-like breakout ($\sigma_v=30$ MPa).....	99
Figure 6.2 Borehole cross section (a) $E_c = 1.5$ GPa and (b) $E_c =15$ GPa.....	101
Figure 6.3 Stress-strain curves with varying E_c at different confining stresses .	102
Figure 6.4 Borehole cross section (a) test 3 ($S_{pb}^N = 120$ MPa, $S_{pb}^S = 270$ MPa) (b) test 4 ($S_{pb}^N = 200$ MPa, $S_{pb}^S = 450$ MPa) (c) test 5 ($S_{pb}^N = 600$ MPa, $S_{pb}^S = 1350$ MPa)	104
Figure 6.5 Borehole cross section (a) test 6 ($\lambda=0.2$) (b) test 7 ($\lambda=0.45$)	106
Figure 6.6 The effect of degree of bonding on (a) broken bonds and broken particles (b) the length of the compaction band.....	107
Figure 6.7 Borehole cross section (a) test 8 ($\mu=0.75$) (b) test 9 ($\mu=3$).....	109
Figure 6.8 The effect of inter-particle friction on (a) broken bonds and broken particles (b) the length of the compaction band.....	110
Figure 6.9 Borehole cross section for (a) particle crushing strength = 60 MPa, (b) particle crushing strength = 40 MPa	112

Figure 6.10 Borehole cross section for the sample with (a) initial porosity of 0.34, (b) initial porosity of 0.40	113
Figure 6.11 The effect of micro-parameters on borehole breakouts.....	114
Figure 6.12 The effect of macro-parameters on borehole breakouts from DEM studies	115
Figure A.1 Configuration of problem (Risnes et al., 1982).....	134
Figure B.1 Stress-strain curves for Castlegate sandstone at different confining stresses	136
Figure B.2 Comparison between the actual Castlegate PSD and the DEM specimen PSD	137
Figure B.3 The SEM image for the Castlegate sandstone (Cheung, 2010)	138
Figure B.4 Comparison between triaxial DEM model and laboratory results....	140
Figure C.1 Stress-strain curves for the base case at different confining stresses	141
Figure C.2 Peak stresses for the base case at different confining stresses.....	142
Figure C.3 Post-peak modulus	143

Nomenclature

A	area of the disk (m^2)
D	particle diameter (m)
D_{\max}	diameter of the largest particle (m)
D_{\min}	diameter of the smallest particle (m)
e_{ijk}	the permutation symbol
E_c	particle contact modulus (Pa)
E_{pb}	Young's modulus of the cement (Pa)
F_i^n	normal contact force (N)
F_i^s	shear contact force (N)
$F_i^{[\Phi^j]}$	force sum for entity Φ^j (N)
\bar{F}_i	total force associated with the parallel bond (N)
$F^{(\omega)}$	force applied by a particle on the wall (N)
G	gain parameter
g_i	body force acceleration (m/sec^2)
H_i	angular momentum (N.m.sec)
I	moment of inertia (m^4)
I_i	principal moment of inertia of the particle about the principal axes of i ($kg.m^2$)
J	polar moment of inertia (m^4)
K^n	normal stiffness (N/m)
k^s	shear stiffness (N/m)
k_{pb}^n	parallel bond normal stiffness (Pa/m)

k_{pb}^S	parallel bond shear stiffness (Pa/m)
$\frac{K^N}{K^S}$	ratio of normal to shear stiffness of the particles
$\frac{K_{pb}^N}{K_{pb}^S}$	ratio of normal to shear stiffness of the cement
m	mass of the particle (kg)
\bar{M}_i	total moment associated with the parallel bond (Nm)
$M_i^{[\Phi^j]}$	moment sum for entity Φ^j (Nm)
n	porosity
N	coordination number
N_c	number of contacts
N_p	number of particles
n_i	unit normal vector
N	coordination number
N_c	number of contacts
N_p	number of particles
n	porosity
P_c	confining stress (Pa)
$R^{[\emptyset]}$	radius of ball \emptyset (m)
R_c	the extent of plastic zone (m)
S_{pb}^n	parallel bond normal strength (Pa)
S_{pb}^S	parallel bond shear strength (Pa)
t	time (sec)
U^n	overlap (m)

V_i	contact velocity (m/sec)
V^{void}	void volume (m ³)
V^{reg}	measurement-region volume (m ³)
V^{mat}	volume of material (m ³)
$V^{(P)}$	volume of particle P (m ³)
$V^{(c)}$	overlap volume of the two particles at contact c (m ³)
$\tilde{V}_i^{(P)}$	mean relative velocity for the N_p particles within a measurement region (m/sec)
$\tilde{x}_i^{(P)}$	centroid location values for the N_p particles within a measurement region (m)
$x_i^{[c]}$	coordination of a contact point (m)
$\dot{x}_i^{[\Phi^j]}$	translational velocity of entity Φ^j (m/sec)
α	radius multiplier
$\dot{\alpha}_{ij}$	strain rate tensor
Δt	time step (sec)
δ_{ij}	the Kronecker delta
λ	percentage of bonded contacts
μ	inter-particle friction coefficient
ρ	density (kg/m ³)
σ_h	minimum horizontal stress (MPa)
σ_H	maximum horizontal stress (MPa)
σ_v	vertical stress (MPa)
σ_{max}	maximum tensile stress acting on the bond (Pa)
$\bar{\sigma}_{ij}$	average stress (Pa)

- $\sigma^{(\omega)}$ wall stress (Pa)
- $\sigma^{(t)}$ desired target wall stress (Pa)
- σ_{ch} characteristic stress (Pa)
- σ_{crush} crushing strength (Pa)
- σ_{rr} radial stress (Pa)
- $\sigma_{\theta\theta}$ tangential stress (Pa)
- σ_{zz} vertical stress (Pa)
- τ_{max} maximum shear stress acting on the bond (Pa)
- $\omega_j^{[\Phi^j]}$ rotational velocity of entity Φ^j (rad/sec)

Abbreviations

2D	Two Dimensional
3D	Three Dimensional
BEM	Boundary Element Method
CD	Contact Dynamics
DDA	Discontinuous Deformation Analysis
DEM	Distinct Element Method
FDM	Finite Difference Method
FEM	Finite Element Method
HC	Hollow Cylinder
MC	Mohr-Coulomb
PFC	Particle Flow Code
PSD	Particle Size Distribution
SEM	Scanning Electron Microscope
SWS	Salt Wash South sandstone
TWC	Thick Walled Cylinder
UCS	Uniaxial Compressive Strength

Chapter 1: General introduction

1.1 Introduction

The term “borehole breakout” is normally associated with borehole cross-sectional elongations resulting from preferential rock failure at and behind the borehole wall during or after drilling (Haimson and Song, 1998). Figure 1.1 shows the formation of borehole breakouts during laboratory testing of carboniferous sandstone performed by Guenot (1989). Observations of sidewall spalling in horizontal shafts at great depths in the Witwaterdrand gold mines were first reported by Leeman (1964). This phenomenon is common in many other circular opening such as boreholes, tunnels, shafts, and drifts in areas of high *in situ* stresses. A substantial number of deep wells around the world have been logged for breakouts using the four-arm dipmeter (Bell, 1990; Bell and Babcock, 1986; Bell et al., 1992; Gough and Bell, 1981) and the borehole televiewer (Hickman et al., 1985; Mastin et al., 1991; Plumb and Hickman, 1985; Zoback et al., 1985).

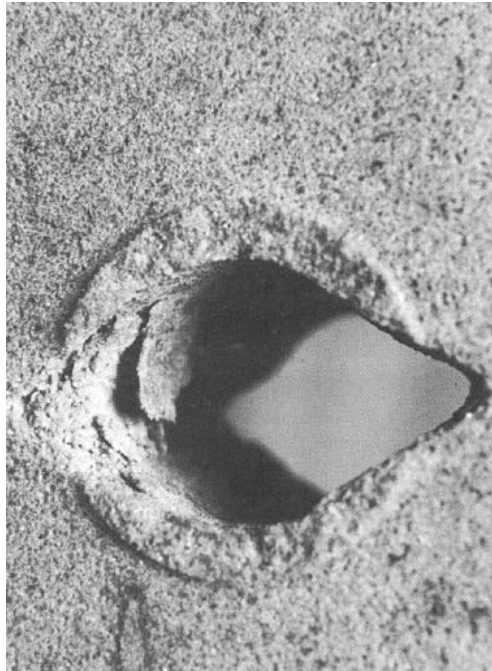


Figure 1.1 Borehole breakout (Guenot, 1989)

A systematic correlation between the breakout orientation and the direction of the regional σ_h was first observed by Bell and Gough (1979) in Alberta, Canada, and was later confirmed by independent laboratory results (e.g., Haimson and Herrick, 1989; Mastin, 1984). Detailed field measurements of the cross sectional dimensions of breakouts, such as angular span and maximum depth, can be made by the digital data processing of ultrasonic borehole televiewer logs (Barton, 1988). Laboratory experiments have not only verified the alignment between the breakout and σ_h directions, but they have also strongly indicated a definite correlation between the breakout dimensions and *in situ* stress magnitudes (Haimson and Herrick, 1989; Herrick and Haimson, 1994).

Several attempts have been made to investigate the failure pattern around the borehole through experimental and theoretical work, but discussions are still ongoing about what controls the failure mechanism and breakout morphology.

There are two types of numerical models that can be used for simulating the degradation process around the borehole: continuum-based models and discontinuum-based models.

Analytical and computational models formulated by standard continuum descriptions are inefficient in modeling rock degradation caused by the natural development of cracks and rupture surfaces, which are of discontinuous in nature (Cundall, 1971). Continuum-based models utilize only the average measures of material degradation in constitutive relationships to represent microstructural damage (Potyondy and Cundall, 2004), and their employment during simulations of material degradation leads to (1) the inability to recover the effect of the hole diameter on the rock response around the well (size effect); and (2) dependency of the results on numerical mesh design (Crook et al., 2003). This major deficiency can be overcome by employing the Distinct Element Method (DEM), which is a discontinuum approach, in the modeling of rock degradation, which is a discontinuum phenomenon. In the DEM, the model consists of an assembly of particles that displace independently from each other and interact at particle contacts that can be bonded (for cemented grains) or unbonded (for

unconsolidated sand). The mechanical behavior of this system is obtained by the application of (1) Newton's second law of translational and rotational motion, which relates particle displacements and rotations to the applied forces, body forces, damping forces, and inter-particle forces and moments; and (2) the force-displacement law at each contact.

The DEM model will also allow an in-depth and fundamental investigation of the degradation process for various conditions. It will be used to study rock fragmentation around the hole in relation to several factors such as rock and fluid properties, and operational conditions, among others. This aspect of the investigation will be further elaborated in this research.

1.2 Problem statement

Over the past few decades, considerable efforts have been made in investigating the mechanisms involved in borehole breakout during drilling. However, much room still remains in furthering our understanding of breakout mechanisms and improving the reliability of the borehole breakout predictive methods.

Rock failure that leads to borehole breakout is a continuous and dynamic process that occurs at the microscopic scale and is discontinuous in nature. Such particle-level phenomena are not captured by the models that are based on continuum approaches. A description of the discrete structure of the particle packing is required to capture the particle-level mechanisms and phenomena.

Three different breakout patterns have been observed in laboratory tests: (1) uniform failure of the hole; (2) V-shaped breakouts; and (3) fracture-type breakouts (Germanovich and Dyskin, 2000; Haimson, 2007; Lavrov et al., 2005).

Physical and mechanical rock properties appear to greatly influence the breakout mechanism and geometry. Previous works are inconclusive in relating material properties (e.g., strength, ductility, and dilatancy) to the type of breakout.

1.3 Research objectives

Significant progress has been achieved in the last decade in understanding the mechanisms of borehole breakout. However, there still are significant ambiguities about the effects of material properties, stress state, and fluid flow on the breakout mechanism and morphology.

This research aims to assess the feasibility of using the DEM to simulate the rock disaggregation and breakout formation process around a hole in sandstone rocks.

Additional goals of this research are to find answers to the following questions:

1. Are fracture-like breakouts created due to the formation of compaction bands?
2. What is the nature and structure of these breakouts?
3. What is the effect of far-field stresses on the size of breakouts?
4. How is the breakout geometry affected by the cement and grain micro-properties?
5. How is the breakout morphology affected by the rock macro-properties?

This research is designed to address the abovementioned questions in understanding of the failure mechanism at the micro scale based on parametric numerical studies at the laboratory scale. The results will help to predict and analyze the breakout morphology as a function of the material properties and applied stress. In order to reach such a goal, this research focuses on the following aspects:

1. Utilize the DEM in furthering the understanding of the physics of rock degradation around boreholes.
2. Develop a breakout model that can be used to reliably and accurately assess the failure mechanism at the laboratory scale.
3. Study the nature and structure of fracture-like breakouts at the micro scale using the breakout model.
4. Study the effect of parameters such as rock porosity, grain and cement stiffness and strength, the amount of cement, and applied stresses on the rock failure mechanism, growth of cavity zone, and breakout morphology.

5. Investigate the effect of material macro-properties on the breakout geometry and failure mechanism by conducting a series of triaxial testing simulations and relating the micro-properties to the corresponding macro-mechanical properties.

1.4 Thesis layout

The research methodology consists of numerical model development, model verification against analytical solutions, model validation against laboratory testing data, and the investigation of borehole breakouts around a borehole at the laboratory scale.

The numerical modeling platform used is PFC3D (PFC = particle flow code), which works based on DEM.

The work in this research is divided into six chapters:

Chapter 1 (the current chapter) provides the background and the scope of this research.

Chapter 2 contains a literature review on the borehole breakout problem. This review presents state-of-the-art information on the factors that affect the failure mechanism and the breakout geometry. A review of current numerical models for borehole breakout investigations is also presented.

Chapter 3 presents the theory of the DEM and the interpretation techniques that can be applied to the DEM results.

Chapter 4 describes in detail the calibration, verification, and validation of a three-dimensional (3D) DEM model using laboratory experiments and analytical solutions. For calibration, 3D discrete element modeling of triaxial tests on Salt Wash South (SWS) sandstone is carried out using the parallel bond model concept in PFC3D. The micromechanical properties of the DEM model are evaluated such that a match is obtained between the DEM results and the macroscopic response of the physical material in triaxial tests under different confining stresses. The pre-peak, peak, and post-peak responses are investigated numerically by conducting parametric studies. In addition, the calibration performance is assessed

by simulating thick walled cylinder (TWC) tests and comparing the model results against laboratory measurements for SWS sandstone. The model is also verified against analytical solutions for a plane strain TWC case. At the end of the chapter, a calibration procedure is suggested by combining the existing knowledge in the literature and the outcome of the sensitivity analysis conducted in this section.

Chapter 5 presents the results of numerical simulations of borehole breakouts using 3D DEM models to investigate the mechanism of fracture-like breakouts and to identify the role of far-field stresses on breakout dimensions. The numerical tool is first verified against analytical solutions. It is then utilized to investigate the failure mechanism and breakout geometry for drilled cubic rock samples (hereafter called drilling experiments) of Castlegate sandstone subjected to different pre-existing far-field stresses.

Chapter 6 numerically investigates the effect of the material micro- and macro-parameters on the failure mechanism and the geometry of the wellbore breakout. The numerical tool is used in simulating the drilling experiments in cubic rock samples subjected to pre-existing far-field stresses. In addition, a series of triaxial testing simulations are conducted to relate the micromechanical parameters to the macromechanical material properties and, hence, relate the breakout type to the rock macro properties.

Chapter 7 summarizes the major findings of this research and presents suggestions for future research on this topic.

1.5 Significance of the work

The study of failure mechanism and breakout morphology will greatly enhance the understanding of various important wellbore phenomena and will enable more accurate predictions in areas such as wellbore stability and sand production.

Wellbore stability problems occur during the drilling of a wellbore. Stability problems amount to 5-10% of drilling costs in exploration and production in the petroleum industry, resulting in a worldwide cost of hundreds of millions of dollars every year. The formation of breakouts results in an irregularity in

borehole shape that leads to large uncertainties in the required cement volumes during the casing job. Further, it may become difficult to run wireline logs or interpret them when the wellbore has an irregular face. However, the main consequence of stability issues is the loss of time, since remedial actions may require reaming and sidetracking, which are time consuming and costly. A better understanding of wellbore breakouts can lead to improved drilling procedures to reduce the size of breakouts and enhance wellbore stability.

Estimates indicate that 70% of the world's hydrocarbon reserves are in sand-prone reservoirs (Bianco and Halleck, 2001). Sanding is estimated to cost the oil industry billions of dollars every year (Kenter and Currie, 1998). Sanding erodes production equipment due to quartz abrasiveness and may lead to casing collapse – a safety as well as an economical problem. Produced sand can damage pumps and even block flow passages. Further, sanding can impact the environment due to the production of sand contaminated by reservoir fluids. The produced sand must be cleaned or injected into deep formations, both being expensive options. On the other hand, sanding can boost productivity by removing wellbore skin developed by formation damage, wax deposition, and fine migration (Geilikman et al., 1994; Vaziri et al., 2002).

Sanding is a two-stage process. In the first stage, *in situ* stresses fail and degrade the rock around the wellbore as a result of drilling-induced stress concentration, pressure drawdown, and reservoir pressure depletion during production. In the second stage, fluid flow may remove/erode the degraded rock, inducing sanding. Sanding cannot occur from intact rock, even if it is poorly consolidated, because flowing fluid in typical wellbore operation limits does not provide sufficient drag to pull sand grains out of the intact rock (Charlez, 1997). Any reliable sanding model should accurately capture this two-stage process. This research will result in an improved understanding of the degradation process, which is precursory to sand production. This knowledge can be used to improve sanding models through enhancing the simulation of the degradation process and through formulating more accurate sanding criteria.

Chapter 2: A review of borehole breakout prediction methods

2.1 Introduction

Analytical and numerical models have been used to analyze wellbore stability. However, conventional models assume wellbore collapse occurs as soon as the wellbore face reaches initial yielding conditions. Such practices lead to conservative wellbore production designs manifested by prescribed high overbalance pressures. The advent of powerful computers and significant advances in computational methods have made it possible to set the criteria for wellbore collapse at conditions beyond the initial yielding of the wellbore wall.

There are two general types of numerical models: continuum based and discontinuum based. Continuum-based approaches have limited capacity in capturing breakout mechanisms accurately. This is because borehole breakouts are discontinuous in nature. Some researchers have recently used methods that are based on discrete element approaches for studying borehole breakouts.

In this chapter, the current literature on borehole breakouts, the stress conditions associated with breakout development, and current breakout prediction methods are presented. The knowledge gap surrounding breakout mechanisms is also reviewed. The review was used in designing the objectives and methodologies used in this research.

2.1.1 Rock disaggregation mechanisms

In the geomechanical context, rock failure mechanisms are listed as tensile failure, shear failure, and compressive failure (also known as pore collapse).

Tensile failure around a borehole occurs when one of the effective stresses is equal to the tensile strength of the formation rock. This mechanism is sometimes related to seepage forces which are proportional to pressure gradients (Bratli and Risnes, 1979).

Shear failure may occur when some planes in the vicinity of the wellbore are subjected to higher shear stress than they can sustain (Figure 2.1). This mechanism is dominant in cemented sands and may lead to buckling when

combined with tensile cracks (Coates and Denoo, 1981; Edwards et al., 1983; Stein, 1988).

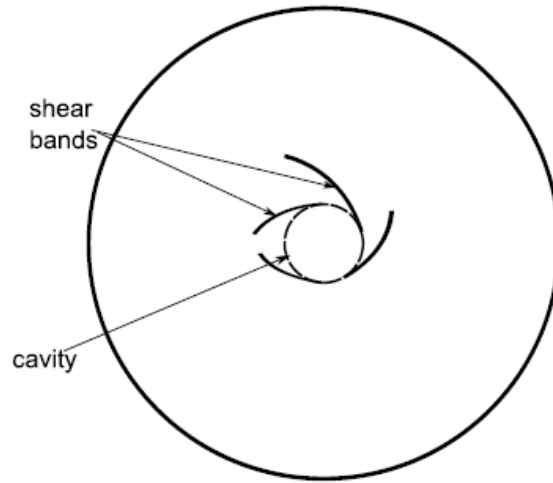


Figure 2.1 Shear bands around a hole

With the depletion of reservoir pressure, effective stresses acting on the formation rock increase. At a certain stress level, pore collapse may occur, and this may lead to borehole breakout. As a result, it is necessary to consider the compactive mode of failure by using a cap in the constitutive law. Detournay (2009), using numerical experiments, showed that the sand production model, enhanced with a cap constitutive law, is capable of reproducing certain cavity morphologies qualitatively. This is called a fracture-like breakout, which has been observed in laboratory tests and has been related to compactive failure.

Failure mechanisms can sometimes be a combination of shear, tensile, and compactive modes that result in different failure morphologies around the borehole or perforations (Crook et al., 2003).

2.1.2 Morphology of cavity growth

Three different breakout patterns have been observed in laboratory tests (Germanovich and Dyskin, 2000; Haimson, 2007; Lavrov et al., 2005): (1) uniform failure of the hole; (2) V-shaped breakouts; and (3) fracture-type breakouts (Figure 2.2).

During uniform failure around the wellbore, the deformation of the surface around the opening is almost uniform, and the cavity remains nearly circular after failure. Using X-ray CT scan images, Lavrov et al. (2005) showed shear bands are localized uniformly around the cavity in this type of breakout (Figure 2.2a).

Figure 2.2b shows a typical V-shaped breakout where diametrically opposed failed zones develop at the borehole wall. This type of breakout has been described to be caused by either tensile spalling or shear fracturing or the combination of the two in the direction of the minimum principal stress (Guenot, 1989; Vardoulakis et al., 1988). In the case of tensile spalling, the rock breakage starts in the vicinity of the borehole as a result of tensile crack initiation and propagation in the direction of the maximum compressive principal stress. Although the propagation of fractures is dominated by tensile failure in this case, shear failure can play an important role in the path of propagation (Shen et al., 2002).

In V-shaped breakouts dominated by shear fracturing, shear failure along one or more shear bands extends from the borehole wall into the rock. Shen et al. (2002) observed limited tensile failure in this process. However, they did not find tensile failure to be crucial in altering the path of fracture propagation and the shape of the breakouts.

Haimson and Song (1998) and Haimson (2001) found that in highly porous sandstone, fracture-like failure bands can develop in the direction of the minimum principal stress (Figure 2.2c). Later Klaetch and Haimson (2002) and Haimson and Lee (2004) observed similar fracture-like failure patterns in St. Peter sandstone and Mansfield sandstone. Scanning Electron Microscope (SEM) images showed that fracture-like breakouts developed by the formation of a narrow compacted band ahead of the breakout tip. Grains were either crushed or broken and repacked within the compacted band, leading to significant porosity reduction. Based on numerical simulations, Lavrov et al. (2005) concluded that elongated slits are associated with tensile failure at the tip of the slit in contrast to Haimson's observations.

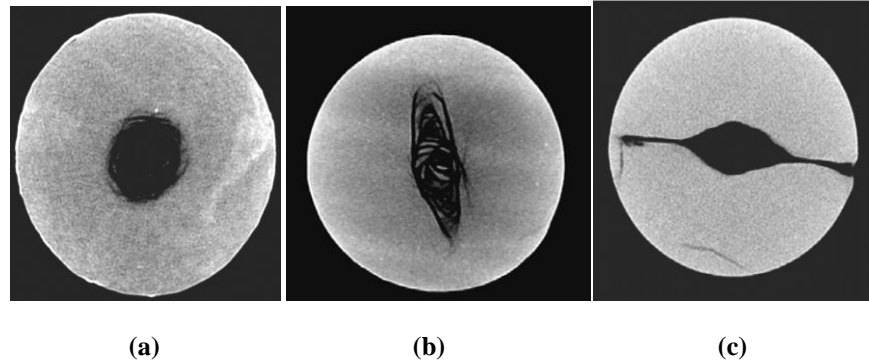


Figure 2.2 Failure pattern of the hole in hollow cylinder sand production tests: (a) uniform hole failure, (b) V-shaped breakout, and (c) fracture-like breakout (Lavrov et al., 2005)

2.2 Factors affecting the failure morphology around the borehole

Several researchers have investigated the failure pattern around the borehole based on field and laboratory observations, but it is not yet clear what factors govern the failure mechanism and breakout morphology.

It is believed that material properties, hole size, boundary conditions, *in situ* stress magnitude and anisotropy, intrinsic rock anisotropy, and fluid flow are the most important factors that control the failure mechanism and the shape of borehole breakouts.

2.2.1 Material properties

Physical and mechanical rock properties appear to greatly influence the breakout mechanism and geometry (Cerasi et al., 2005).

Based on experimental results, Cerasi et al. (2005) and Li et al. (2006) showed that compactive and relatively weak sandstones with ductile behavior tend to develop uniform hole failure under isotropic stress conditions.

Lee and Haimson (1993) and Shen et al. (2002) concluded that tensile spalling is typical for hard crystalline rocks such as granite. Shear fracturing, on the other hand, was observed in the laboratory in soft limestone, sandstone and dolomite rocks (Zoback et al., 1985; Guenot, 1989). Based on experimental results, Cerasi et al. (2005) showed that moderately strong sandstones tend to develop V-shaped breakouts. Based on laboratory results, Li et al. (2006) also showed the V-shaped breakout development in a ductile and dilatant sandstone.

Based on laboratory experiments, Haimson and Lee (2004) and Haimson (2007) observed the formation of narrow slits in high porosity, weak and quartz-rich sandstones. In contrast, Li et al. (2006) and Cerasi et al. (2005) experimentally concluded that this type of breakout is associated with relatively strong and brittle sandstone. Based on numerical results, Lavrov et al. (2005) showed that fracture-like breakouts are associated with tensile failure at the tip of the slit and develop in brittle and dilatant sandstones.

The size and distribution of micro cracks or voids inside the rock appear to play an important role in the failure mode and the breakout geometry (Rawlings et al., 1993). Rawlings et al. (1993), based on laboratory experiments, showed that large but sparse micro cracks are more likely to form splitting failure mode as they propagate in tension in the direction of maximum compressive principal stress; small but dense micro cracks (voids) tend to form shear failure as they are easier to coalesce in the direction of maximum shearing. This may explain why more shear-induced breakouts are commonly observed in rock types such as sandstone (Kutter and Rehse, 1996; Rawlings et al., 1993).

Table 2.1 summarizes the observations of breakout geometries associated with material properties based on the literature. It shows that material properties control the breakout around the wellbore. However, a certain material property (i.e., strength, ductility, and dilatancy) alone may not be sufficient to accurately predict the failure pattern. For example, fracture-like breakouts can be seen in both weak and competent rocks.

There is no consensus in the literature about the parameters that govern failure mechanisms (Shen et al., 2002). One of the major objectives in this research is to identify the factors that affect the failure pattern and mechanism around the hole based on the existing knowledge in the literature and numerical analysis.

Table 2.1 Failure patterns associated with material properties

	Strength		Ductility		Dilatancy	
	Weak	Competent	Ductile	Brittle	Dilatant	Compactive
Uniform failure	X		X			X
V-shaped		X	X		X	
Fracture-like	X	X		X	X	

2.2.2 Size effect

Laboratory Hollow Cylinder (HC) tests have shown that the breakout failure mechanism depends not only on the material properties, but also on the hole size (van den Hoek et al., 1994). Based on the results of laboratory HC tests on 8-178 mm diameter holes, van den Hoek et al. (1994) concluded a splitting failure mechanism for Castlegate sandstone. In contrast, the failure mechanism in the tight Berea sandstone changed from splitting to shear failure with increasing hole sizes. Size dependency was only observed below a certain inner-hole diameter. These observations were also reproduced numerically in the theoretical work of van den Hoek et al. (2000). They showed that large cavities (e.g., boreholes) always fail in compression, whereas small cavities (e.g., perforations) may fail either in compression or in tension, depending on material properties and moisture content (oven-dried versus moist rocks).

In high-porosity Berea sandstone, Haimson and Kovacich (2003) found that the slit length increases substantially at higher borehole diameters. When scaling up the laboratory slit hole sizes to petroleum well diameters, it is conceivable that slit lengths could reach several meters and be a source of substantial sand production (Haimson, 2007).

2.2.3 Far-field stress anisotropy

Experimental studies on borehole stability under anisotropic stresses have been performed on limestones (e.g., Haimson and Herrick, 1989; Haimson and Song,

1993), granites (e.g., Lee and Haimson, 1993; Martin et al., 1994), and sandstone (e.g., Haimson and Lee, 2004; Haimson and Song, 1998; Wu et al., 2005). These studies focused primarily on the effect of lateral stress anisotropy on borehole failure stress and on the breakout geometry. For example, the laboratory study by Lee and Haimson (1993) revealed distinct and sharp breakouts in specimens of Lac du Bonnet granite. The size of the breakouts increased with σ_H at constant σ_h , and the shape of the breakouts remained similar, independent of the state of far-field stresses. A two-dimensional (2D) numerical simulation by Shen et al. (2002) also showed the stress ratio affects size of the breakouts. Increased stress anisotropy leads, generally, to breakouts on diametrically opposite sides of the wellbore.

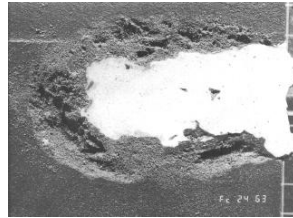
Papamichos et al. (2010) examined the effect of both axial and lateral stress anisotropies on the hole stability of Red Wildmoor sandstone through a series of HC tests. The axial stress anisotropy was found to have a significant effect on the borehole failure mode of Red Wildmoor sandstone. Lateral hole failure was observed in plane strain HC tests under radial loading and in polyaxial tests where the axial over major lateral stress ratio was between 0.5 and 1. In these cases, the tangential stress at the hole was found to be the largest compressive principal stress, and breakout occurred in planes normal to the hole axis. On the other hand, in HC tests in which axial stress at the hole was the largest compressive principal stress, failure occurred in planes parallel to the tangential stress direction.

One of the objectives in this research is to study the effect of stress anisotropy on the breakout length and shape in cubic laboratory rock samples.

2.2.4 Fluid flow

Fluid flow has been observed to influence the size and mode of failure. Fluid flow can remove the disaggregated materials and, therefore, grow the disaggregation zone. Fluid flow has a high impact in the case of fracture-type failure. Shen et al. (2002) showed that narrow slits are developed by the removal of loose grains and grain fragments that were debonded in the process of compaction band formation.

Tronvol and Fjaer (1994) examined the effect of fluid flow on the failure zone evolution around the perforation cavity. One outcrop sandstone (Red Wildmoor sandstone) and three field sandstones from the North Sea (Core No. 1, Core No. 2, and Core No. 3) were used in the study. In cavity failure experiments without fluid flow, breakouts were extended laterally from the cavity wall. Both two-fold (Redwildmoor and Core No. 1, which were weak rocks) and three-fold (Core No. 2 and No. 3, which were strong rocks) symmetry were observed. In the case of two-fold symmetry, pure shear failure or a combined shear-spalling process seemed to occur; whereas, in the case of three-fold symmetry, a combination of shear and extension fractures were observed. Generally, two types of failure zones were observed with fluid flow. In the tests with fluid flow on Redwildmoor sandstone and Core No. 1, a continuous failure zone of altered porosity extended a few millimeters into the surrounding rock from the cavity surface. In case of Redwildmoore sandstone, the rock was totally plastified in this zone (Figure 2.3a); whereas, in case of Core No. 1, the zone was relatively intact (Figure 2.3b). Also, a failure zone propagating from the cavity bottom in the axial direction of the rock specimen was observed in the tests with fluid flow.



(a) Cavity failure pattern for Red Wildmoor sandstone



(b) Cavity failure pattern for Core No. 1

Figure 2.3 Failure pattern of the hole in perforation test (Tronvol and Fjaer, 1994)

2.3 Numerical modeling of borehole breakout

It is crucial to reproduce the mechanism of breakout formation numerically to be able to describe the field and laboratory observations and improve the prediction tools for phenomena such as wellbore breakouts and sand production. Over the past few decades, considerable efforts have been made in developing numerical methods that can describe the degradation process around the hole under various reservoir and operational conditions. Many researchers have attempted to model this physical phenomenon by analytical and numerical techniques to relate the breakout type to the rock and fluid properties, *in situ* stresses, wellbore geometry, and fluid and solid skeleton interaction and deformation. In general, such numerical models are classified into continuum and discontinuum approaches.

2.3.1 Numerical models based on a continuum approach

In continuum approaches, reservoir rock is treated as a continuous medium. The assumption of continuity indicates that the material cannot be torn or broken into pieces except at predetermined locations and, in the presence of discontinuity, the deformation along or across the discontinuity has the same order of magnitude as that of the solid matrix.

Bell and Gough (1979) proposed that breakouts resulted from episodic spalling of triangular rock fragments enclosed by two conjugate shear fractures. The shear fractures in their model formed when the tangential stress at the borehole wall reached the rock strength as defined by the Mohr-Coulomb (MC) failure criterion. The model was successful in modeling dog-ear breakouts along the σ_h as had been observed in Alberta oilfields wellbores (Bell and Gough, 1979). They concluded that the final breakout shape and size does not depend on the *in situ* stress magnitude, rather it depends on the friction angle. However, Haimson and Herrick (1989) found that the breakout dimensions depended on the far-field stresses.

Zheng et al. (1989) developed a numerical model using the boundary element method (BEM). They simulated the evolution of borehole breakouts (initiation, growth, and stabilization) by assuming breakouts were created by extensile splitting, following the observation made by Haimson and Herrick (1989).

Breakouts generated by the model were only V-shaped breakouts, and the size of the breakout was related only to far-field stress magnitudes.

Several researchers have used the finite difference method (FDM), finite element method (FEM), and BEM along with elasto-plastic models in conjunction with laboratory tests for research on borehole breakout problems (e.g., Detournay et al., 2009; Mastin, 1984; Papamichos and Malmanger, 2001; Zheng et al., 1989). However, there are some limitations to these approaches:

1. Classical elasto-plastic continuum models are inefficient in modeling localization phenomena due to their discontinuous nature.
2. The predictions carried out using these approaches are heavily dependent on the choice of constitutive material model used and the complexity of the model. Complex models might be required to capture the rock damage and changes in permeability.

Using the bifurcation theory, van den Hoek et al. (2000) showed that the employment of such models in simulation of material degradation leads to inability in recovering size dependency and dependency of the results on numerical mesh design. This problem can be addressed by pursuing two distinct solutions: 1) using discontinuum models that will be discussed in the next section; and 2) enriching the standard continuum description by regularization methods, such as the Cosserat continuum, gradient plasticity, and fracture energy regularization method or by using non-local models (Crook et al., 2003).

In a Cosserat continuum, individual points possess, in addition to their translational degrees of freedom, independent rotational degrees of freedom (Muhlhaus and Vardoulakis, 1987). In a detailed study of borehole instability using the Cosserat continuum model in conjunction with the bifurcation theory, Papanastasiou and Vardoulakis (1992) showed that the micro-rotations play an important role in borehole stability computations. Micro-rotations are insignificant in the trivial axisymmetric solutions but they become significant in the localized secondary solution. Papanastasiou and Vardoulakis (1992) also showed that whilst the computational results are imperfection sensitive, the

predicted failure pattern is persistent. However, the Cosserat continuum is only effective as a regularization method when frictional slip is dominant (Sluys, 1992). For example, micro-polar rotations have no influence on Mode I failure in uniaxial tension. This is a potential weakness of the methodology for more complex material models that include direct modeling of the Mode I fracture associated with axial splitting (Crook et al., 2003).

The essential feature of the gradient plasticity theory is that the evolution of the yield function is dependent on both the damage variable and the spatial gradients of the damage variable (Muhlhaus and Aifantis, 1991; Pamin, 1994). The presence of these higher order gradients in a macroscopic constitutive model is associated with non-local interaction at the microstructural level. The methodology is equally applicable to Mode I and Mode II localization problems and has been applied to the study of borehole stability (Sulem et al., 1995). However, it should be noted that this method is effective if the shear/fracture band is larger than the element size, necessitating fine mesh discretizations or adaptive mesh refinement upon shear band initiation. Additionally, as in the case of the Cosserat continuum approach, the extension to finite strains and complex material models is not trivial (Crook et al., 2003).

The non-local concept was originally developed to study elastic materials with randomly heterogeneous microstructure (Eringen, 1966) by relating non-local spatial averages of both continuum stress and strain over a statistically representative volume. By using this method, fine discretizations are required to ensure sufficient material points within the representative volume used for computation of the non-local variables (Crook et al., 2003).

The standard continuum may be regularized by incorporating fracture energy as a material constant in the equations governing state variable evolution (Bazant and Oh, 1983). Among different regularization techniques, the fracture energy approach is the most pragmatic because it could be implemented in the numerical modeling scheme without modifying the standard numerical techniques.

2.3.2 Numerical models based on a discontinuum approach

Several researchers have identified particle-based DEM as a useful tool in the investigation of breakout morphology and sand production. DEM is a numerical modeling method where particles and their interactions are modeled explicitly, instead of treating the material as a continuum. DEM can directly model grain-scale processes and capture the effects of bonding on particle mechanics, as well as the relative translation, sliding, and rotation between the particles.

At first, Rawlings et al. (1993) investigated the influence of natural fractures, stress anisotropy, and wellbore orientation on wellbore stability and breakout geometry. Their model was based on direct simulation of block movements using a DEM code called UDEC (Itasca, 2000) to investigate the mechanism of uniform and V-shaped breakouts in heavily pre-fractured rocks.

Li et al. (2006) used a 2D commercial DEM code, PFC2D (Itasca, 2004), to simulate HC tests with fluid flow and to study sanding and breakout geometry. PFC2D simulates an assembly of circular disks with the bonds inserted between them. They found three typical breakout geometries in the simulations similar to those observed in laboratory tests. The fracture-like breakout was observed when the material is prone to localized compressive failure. However, the compacted zone of reduced porosity was not observed at the breakout tip. For the cases where the material was weak and the tensile strength was low, uniform failure around the borehole was observed along with a rather uniform hole enlargement. In the cases with relatively competent rock properties, which were unlikely to fail in localized compaction, V-shaped breakout failure patterns were observed.

Only two force components and one moment component exist in 2D DEM models. However, three force components and three moment components are considered in 3D DEM models. Since borehole breakouts are a 3D problem with complex geometry, where cement bonds and arching of particles are important, this problem must be modeled using 3D DEM.

2.4 Conclusions

Laboratory and numerical investigations have shown that material properties, hole size, boundary conditions, *in situ* stress magnitude and anisotropy, and fluid flow are among the most important factors that control the failure mechanism and the shape of borehole breakouts. However, there still are significant disagreements and ambiguities on what factors govern the failure mechanism and breakout morphology and how.

Only a limited number of natural rocks has been used in laboratory tests, which is inadequate for drawing a comprehensive conclusion about the factors that affect borehole breakouts. This is particularly true considering multiple factors including the rock micro and macromechanical properties that impact borehole breakouts.

Continuum-based numerical models for borehole breakout problems are inefficient in modeling localization phenomena due to their discontinuous nature. The predictions carried out using these approaches are heavily dependent on the choice of constitutive material model.

Several researchers have identified particle-based DEM as a useful tool in the investigation of breakout morphology and sand production. So far, only a few 2D DEM models have been utilized in borehole breakout research. Using a 3D DEM model is necessary for the simulation of borehole breakouts that, generally, are 3D entities with complex geometry.

Chapter 3: Discrete Element Method

3.1 Introduction

Discrete element modeling is a numerical method that explicitly models the interaction between blocks or between particles. It can be used to simulate problems where large deformation occurs (e.g., slope failure or when localization develops in the borehole breakout problem). O’Sullivan (2002) provided an overview of different discrete element modeling tools and their features, including the particle-based DEM, Discontinuous Deformation Analysis (DDA), and Contact Dynamics (CD) method. Among these methods, the particle-based DEM proposed by Cundall and Strack (1979) is the most popular discrete element modeling tool that is used in geotechnical engineering.

Simpson and Tatsuoka (2008) and Zdravkovic and Carter (2008) noted that a key application of DEM is to improve the understanding of fundamental soil behavior from the micromechanical perspective. Li et al. (2006) used 2D DEM models to demonstrate DEM’s potential in capturing borehole breakouts. As described in Chapter 2, simulating the borehole breakout problem using 3D DEM is more appropriate. In addition, analyzing the micromechanical data (particle-scale information) from DEM simulations can provide further insight into the evolution of the mechanisms leading to the development of a borehole breakout around a hole.

In this chapter, an overview of the DEM theory is given, and the contact models and the boundary conditions are summarized. Also, methods to interpret DEM results are discussed. Most DEM formulations in this chapter are adopted from Itasca (2008).

3.2 Distinct Element Method (DEM)

A particle-based DEM analysis involves modeling a granular material using particles that usually have simple geometries (e.g., spheres in 3D DEM or disks in 2D DEM) and explicitly simulating the interactions between them. These ideal particles are usually assumed rigid, but small overlaps (referred to as soft

contacts) are allowed at the contact points. These overlaps are analogous to the deformations that occur at real particle contacts of geomaterials. At any inter-particle contact, a contact stiffness model is used to relate the contact force to this overlap. This model allows particles to lose contact if overlap between the particles no longer exists.

The calculation cycle in PFC3D is based on a time stepping algorithm that requires the repeated application of the law of motion to each particle, a force-displacement law at each contact, and a constant updating of the position of the so-called walls which are used to apply boundary conditions. Contacts, which may exist between two balls or between a ball and a wall can be formed and broken automatically during the course of a simulation. The calculation cycle is illustrated in Figure 3.1.

At the start of each time step, the set of contacts is updated from the known particle and wall positions. The force-displacement law is then applied to each contact to update the contact forces based on the relative motion between the two entities at the contact and the contact constitutive model. Next, the law of motion is applied to each particle to update its velocity and position based on the resultant force and moment arising from the contact forces and body forces acting on the particle. Also, the wall positions are updated based on the specified wall velocities. The calculations performed in each of the two boxes of Figure 3.1 can be done in parallel.

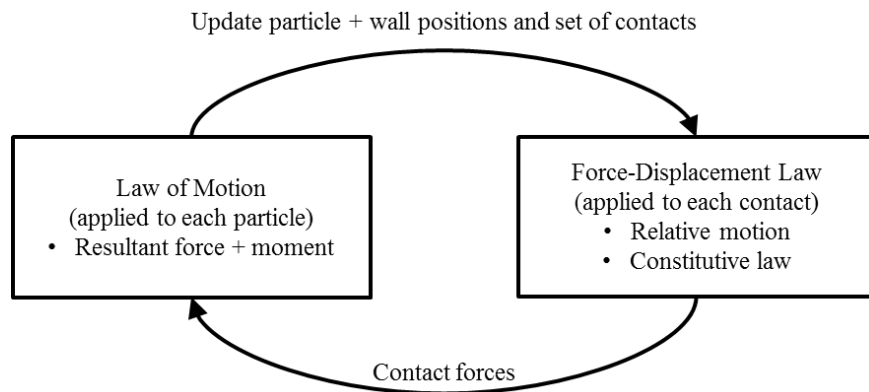


Figure 3.1 DEM calculation flow chart (Itasca, 2008)

During each calculation cycle, the dynamic equilibrium of the system is attained and the responses of materials under quasi-static conditions are obtained. In quasi-static conditions, the system is in static equilibrium and the particle velocities and accelerations are small. Low particle resultant forces indicate the system is balanced and static equilibrium is achieved.

The magnitudes of the particle resultant forces, often referred to as the unbalanced forces, can be tracked during the analysis. A criterion can be developed to terminate the DEM calculations automatically when the magnitudes of these unbalanced forces are low (e.g., 1% of the average contact forces in the system). This is particularly useful in solving the geotechnical problems in which a steady state or quasi-static condition is required.

In the next sections, the force-displacement law is described, followed by a description of the law of motion. The formulation will be presented for general 3D problems.

3.2.1 Force-displacement law

The force-displacement law relates the relative displacement between two entities at a contact to the contact force acting on the entities. For both ball-ball and ball-wall contacts, this contact force arises from contact occurring at a point. For ball-ball contact, an additional force and moment arising from the deformation of the cementitious material represented by a parallel bond can also act on each particle. The calculation for parallel bonds will be discussed later in this chapter.

The force-displacement law operates at a contact and can be described in terms of a contact point, $x_i^{[c]}$, lying on a contact plane that is defined by a unit normal vector, n_i . The contact point is within the interpenetration volume of the two entities. For ball-ball contact, the normal vector is directed along the line between ball centers; for ball-wall contact, the normal vector is directed along the line defining the shortest distance between the ball center and the wall. The contact force is decomposed into a normal component acting in the direction of the normal vector and a shear component acting in the contact plane. The force-displacement law relates these two components of force to the corresponding

components of the relative displacement via the normal and shear stiffnesses at the contact.

The force-displacement law is described for both ball-ball and ball-wall contacts. For ball-ball contact, the relevant equations are presented for two spherical particles labeled A and B in Figure 3.2. For ball-wall contact, the relevant equations are presented for a spherical particle and a wall labeled b and w, respectively, in Figure 3.3. In both cases, U^n denotes overlap.

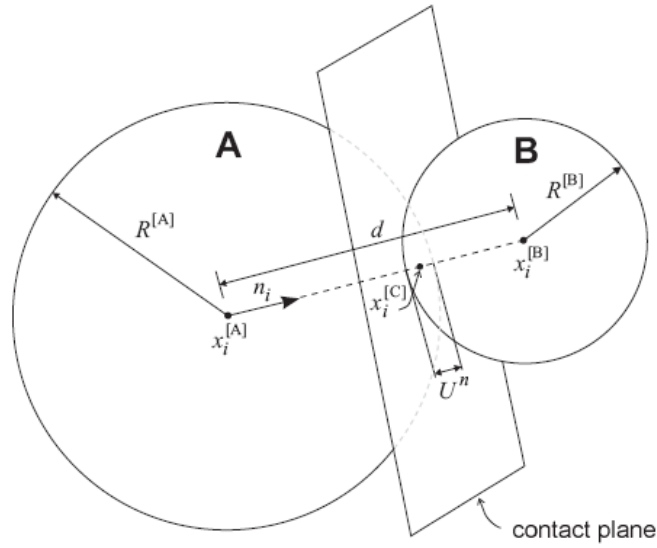


Figure 3.2 Ball-ball contact (Itasca, 2008)

For ball-ball contact, the unit normal, n_i , that defines the contact plane is given by

$$n_i = \frac{x_i^{[B]} - x_i^{[A]}}{d} \quad (\text{ball-ball}) \quad (3.1)$$

where $x_i^{[A]}$ and $x_i^{[B]}$ are the position vectors of the centers of Balls A and B, and d is the distance between the ball centers.

$$d = |x_i^{[B]} - x_i^{[A]}| = \sqrt{(x_i^{[B]} - x_i^{[A]})(x_i^{[B]} - x_i^{[A]})} \quad (\text{ball-ball}) \quad (3.2)$$

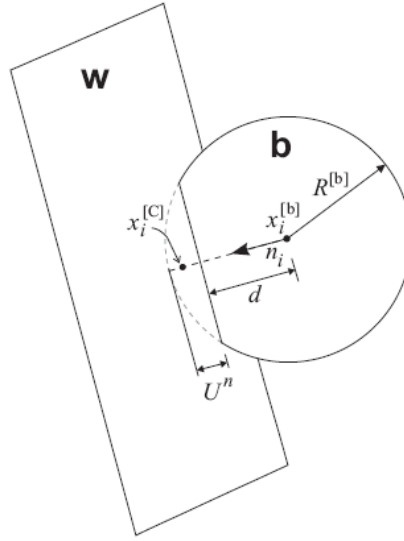


Figure 3.3 Ball-wall contact (Itasca, 2008)

For ball-wall contact, n_i is directed along the line defining the shortest distance, d , between the ball center and the wall. This direction is found by mapping the ball center into a relevant portion of space defined by the wall. The idea is illustrated in Figure 3.4 for a 2D wall composed of two line segments (\overline{AB} and \overline{BC}). All spaces on the active side of this wall can be decomposed into five regions by extending a line normal to each wall segment at its end points. If the ball center lies in Region 2 or 4, it will contact the wall along its length, and n_i will be normal to the corresponding wall segment. However, if the ball center lies in Region 1, 3, or 5, it will contact the wall at one of its end points, and n_i will lie along the line joining the end point and the ball center.

The overlap U^n , defined to be the relative contact displacement in the normal direction, is given by

$$U^n = \begin{cases} R^{[A]} + R^{[B]} - d & (\text{ball} - \text{ball}) \\ R^{[b]} - d & (\text{ball} - \text{wall}) \end{cases} \quad (3.3)$$

where $R^{[\emptyset]}$ is the radius of ball \emptyset .

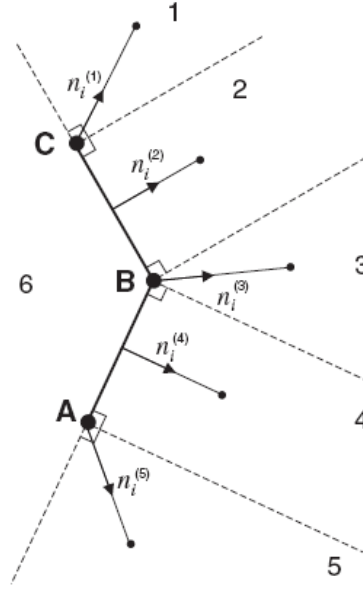


Figure 3.4 Determination of normal direction for ball-wall contact (Itasca, 2008)

The location of the contact point is given by

$$x_i^{[C]} = \begin{cases} x_i^{[A]} + \left(R^{[A]} - \frac{1}{2}U^n\right)n_i \text{ (ball-ball)} \\ x_i^{[b]} + \left(R^{[b]} - \frac{1}{2}U^n\right)n_i \text{ (ball-wall)} \end{cases} \quad (3.4)$$

The contact force vector F_i (which represents the action of Ball A on Ball B for ball-ball contact and the action of the ball on the wall for ball-wall contact) can be resolved into normal and shear components with respect to the contact plane as

$$F_i = F_i^n + F_i^s \quad (3.5)$$

where F_i^n and F_i^s denote the normal and shear component vectors, respectively.

The normal contact force vector is calculated by

$$F_i^n = K^n U^n n_i \quad (3.6)$$

where K^n is the normal stiffness (force/displacement) at the contact. The value of K^n is determined by the current contact-stiffness model.

Note that the normal stiffness, K^n , is a secant modulus in that it relates total displacement and force. The shear stiffness, k^s , on the other hand, is a tangent modulus in that it relates incremental displacement and force (see Eq. 3.14). An uppercase K will be used to denote a secant modulus, and a lowercase k will be

used to denote a tangent modulus. The computation of the normal contact force from the geometry alone makes the code less prone to numerical drift and able to handle arbitrary placement of balls and changes in ball radii after a simulation has begun.

The shear contact force is computed in an incremental fashion. When the contact is formed, the total shear contact force is initialized to zero. Each subsequent relative shear-displacement increment results in an increment of elastic shear force that is added to the current value. The motion of the contact must be considered during this procedure.

The motion of the contact is accounted for by updating n_i and $x_i^{[c]}$ every time step. Since the shear contact force vector F_i^S is stored as a vector in global coordinates, it must also be updated to account for contact motion. F_i^S is updated by calculating two rotations: the first is about the line common to the old and new contact planes; and the second is about the new normal direction. The equations assume that the rotations are small. The first rotation is expressed by

$$\{F_i^S\}_{rot.1} = F_j^S \left(\delta_{ij} - e_{ijk} e_{kmn} n_m^{[old]} n_n \right) \quad (3.7)$$

where $n_m^{[old]}$ is the old unit normal to the contact plane. The second rotation is expressed by

$$\{F_i^S\}_{rot.2} = \{F_j^S\}_{rot.1} \left(\delta_{ij} - e_{ijk} \langle \omega_k \rangle \Delta t \right) \quad (3.8)$$

where $\langle \omega_k \rangle$ is the average angular velocity of the two contacting entities about the new normal direction

$$\langle \omega_i \rangle = \frac{1}{2} \left(\omega_j^{[\Phi^1]} + \omega_j^{[\Phi^2]} \right) n_j n_i \quad (3.9)$$

where $\omega_j^{[\Phi^j]}$ is the rotational velocity of entity Φ^j given by

$$\{\Phi^1, \Phi^2\} = \begin{cases} \{A, B\} & (ball - ball) \\ \{b, w\} & (ball - wall) \end{cases} \quad (3.10)$$

The relative motion at the contact, or the contact velocity V_i (which is defined as the velocity of Ball B relative to Ball A at the contact point for ball-ball contact and the velocity of the wall relative to the ball at the contact point for ball-wall contact), is given by

$$V_i = (\dot{x}_i^{[C]})_{\Phi^2} - (\dot{x}_i^{[C]})_{\Phi^1} = \left(\dot{x}_i^{[\Phi^2]} + e_{ijk}\omega_j^{[\Phi^2]} (x_k^{[C]} - x_k^{[\Phi^2]}) \right) - \left(\dot{x}_i^{[\Phi^1]} + e_{ijk}\omega_j^{[\Phi^1]} (x_k^{[C]} - x_k^{[\Phi^1]}) \right) \quad (3.11)$$

where $\dot{x}_i^{[\Phi^j]}$ is the translational velocity of entity Φ^j from Eq. 3.10. (Note that $\omega_i^{[w]}$ is the rotational velocity of the wall with respect to $x_i^{[w]}$, the center of rotation of the wall.)

The contact velocity can be resolved into normal and shear components with respect to the contact plane. Denoting these components by V_i^n and V_i^s for the normal and shear components, respectively, the shear component of the contact velocity can be written as

$$V_i^s = V_i - V_i^n = V_i - V_j n_j n_i \quad (3.12)$$

The shear component of the contact displacement-increment vector, occurring over a time step of Δt , is calculated by

$$\Delta U_i^s = V_i^s \Delta t \quad (3.13)$$

and is used to calculate the shear elastic force-increment vector

$$\Delta F_i^s = -k^s \Delta U_i^s \quad (3.14)$$

where k^s is the shear stiffness (force/displacement) at the contact. The value of k^s is determined by the current contact stiffness model. The shear stiffness is a tangent modulus and is thus denoted using a lowercase k .

The new shear contact force is found by summing the old shear force vector at the start of the time step (after it has been rotated to account for the motion of the contact plane) with the shear elastic force-increment vector

$$F_i^S = \{F_i^S\}_{rot.2} + \Delta F_i^S \quad (3.15)$$

The values of normal and shear contact force determined by Eqs. (3.6) and (3.15) are adjusted to satisfy the contact constitutive relations. After this adjustment, the contribution of the final contact force to the resultant force and moment on the two entities in contact is given by

$$F_i^{[\Phi^1]} \leftarrow F_i^{[\Phi^1]} - F_i$$

$$F_i^{[\Phi^2]} \leftarrow F_i^{[\Phi^2]} - F_i$$

$$M_i^{[\Phi^1]} \leftarrow M_i^{[\Phi^1]} - e_{ijk} \left(x_j^{[C]} - x_j^{[\Phi^1]} \right) F_k \quad (3.16)$$

$$M_i^{[\Phi^2]} \leftarrow M_i^{[\Phi^2]} + e_{ijk} \left(x_j^{[C]} - x_j^{[\Phi^2]} \right) F_k$$

where $F_i^{[\Phi^j]}$ and $M_i^{[\Phi^j]}$ are the force and moment sums for entity Φ^j from Eq. (3.10), and F_i is given by Eq. (3.5).

3.2.2 Law of motion

The motion of a single rigid particle is determined by the resultant force and moment vectors acting upon it and can be described in terms of the translational motion of a point in the particle and the rotational motion of the particle. The translational motion of the center of mass is described in terms of its position, x_i , velocity, \dot{x}_i , and acceleration, \ddot{x}_i ; the rotational motion of the particle is described in terms of its angular velocity, ω_i , and angular acceleration, $\dot{\omega}_i$.

The equations of motion can be expressed as two vector equations: one relates the resultant force to the translational motion, and the other relates the resultant moment to the rotational motion. The equation for translational motion can be written in the vector form

$$F_i = m(\ddot{x}_i - g_i) \quad (\text{translational motion}) \quad (3.17)$$

where F_i is the resultant force, the sum of all externally applied forces acting on the particle; m is the total mass of the particle; and g_i is the body force acceleration vector (e.g., gravity loading).

The equation for rotational motion can be written in the vector form

$$M_i = \dot{H}_i \quad (3.18)$$

where M_i is the resultant moment acting on the particle, and H_i is the angular momentum of the particle. This equation is used in a local coordinate system that is attached to the particle at its center of mass. If this local system is oriented such that it lies along the principal axes of inertia of the particle, then Eq. (3.18) reduces to Euler's equation of motion

$$\begin{aligned} M_1 &= I_1 \dot{\omega}_1 + (I_3 - I_2) \omega_3 \omega_2 \\ M_2 &= I_2 \dot{\omega}_2 + (I_1 - I_3) \omega_1 \omega_3 \\ M_3 &= I_3 \dot{\omega}_3 + (I_2 - I_1) \omega_2 \omega_1 \end{aligned} \quad (3.19)$$

where I_1 , I_2 , and I_3 are the principal moments of inertia of the particle; $\dot{\omega}_1$, $\dot{\omega}_2$, and $\dot{\omega}_3$ are the angular accelerations about the principal axes; and M_1 , M_2 , and M_3 are the components of the resultant moment referred to the principal axes.

For a spherical particle of radius R , whose mass is distributed uniformly throughout its volume, the center of mass coincides with the sphere center. Any local-axis system attached to the center of mass is a principal-axis system, and the three principal moments of inertia are equal to one another. Thus, for a spherical particle, Eq. (3.19) can be simplified and referred to the global-axis system as

$$M_i = I \dot{\omega}_i = \left(\frac{2}{5} m R^2\right) \dot{\omega}_i \quad (\text{rotational motion}) \quad (3.20)$$

The equations of motion, given by Eqs. (3.17) and (3.20), are integrated using a centered finite-difference procedure involving a time step of Δt . The quantities \dot{x}_i and ω_i are computed at the mid-intervals of $t \pm n\Delta t/2$, while the quantities x_i , \ddot{x}_i , $\dot{\omega}_i$, F_i , and M_i are computed at the primary intervals of $t \pm n\Delta t$.

The following expressions describe the translational and rotational accelerations at time t in terms of the velocity values at mid-intervals. The accelerations are calculated as

$$\ddot{x}_i^{(t)} = \frac{1}{\Delta t} \left(\dot{x}_i^{(t+\Delta t/2)} - \dot{x}_i^{(t-\Delta t/2)} \right) \quad (3.21)$$

$$\dot{\omega}_i^{(t)} = \frac{1}{\Delta t} \left(\omega_i^{(t+\Delta t/2)} - \omega_i^{(t-\Delta t/2)} \right)$$

Inserting these expressions into Eqs. (3.17) and (3.20), and solving for the velocities at time $(t + \Delta t/2)$, results in

$$\begin{aligned} \dot{x}_i^{(t+\Delta t/2)} &= \dot{x}_i^{(t-\Delta t/2)} + \left(\frac{F_i^{(t)}}{m} + g_i \right) \Delta t \\ \omega_i^{(t+\Delta t/2)} &= \omega_i^{(t-\Delta t/2)} + \left(\frac{M_i^{(t)}}{I} \right) \Delta t \end{aligned} \quad (3.22)$$

Finally, the velocities in Eq. (3.22) are used to update the position of the particle center as

$$x_i^{(t+\Delta t)} = x_i^{(t)} + \dot{x}_i^{(t+\Delta t/2)} \Delta t \quad (3.23)$$

The calculation cycle for the law of motion can be summarized as follows: given the values of $\dot{x}_i^{(t-\Delta t/2)}$, $\omega_i^{(t-\Delta t/2)}$, $x_i^{(t)}$, $F_i^{(t)}$, and $M_i^{(t)}$, Eq. (3.22) is used to obtain $\dot{x}_i^{(t+\Delta t/2)}$ and $\omega_i^{(t+\Delta t/2)}$. Then, Eq. (3.23) is used to obtain $x_i^{(t+\Delta t)}$. The values of $F_i^{(t+\Delta t)}$ and $M_i^{(t+\Delta t)}$, to be used in the next cycle, are obtained by application of the force-displacement law.

3.3 Mechanical time step determination

The equations of motion are integrated in PFC3D using a centered finite-difference scheme expressed by Equations (3.21) and (3.22). The computed solution produced by these equations will remain stable only if the time step does not exceed a critical time step that is related to the minimum Eigen-period of the total system. However, global eigenvalue analyses are impractical to apply to the

large and constantly changing systems typically encountered in a PFC3D simulation. Therefore, a simplified procedure is implemented in PFC3D to estimate the critical time step at the start of each cycle (Itasca, 2008).

3.4 Mechanical damping

The idea of damping is to dissipate the energy in real situations that is not already incorporated in the DEM model via frictional contacts or bond breakages.

There are local damping and viscous damping in PFC3D to dissipate kinetic energy. Local damping acts on each ball, while viscous damping acts at each contact. Local damping applies a damping force, with magnitude proportional to unbalanced force, to each ball. Viscous damping adds normal and shear dashpots at each contact. These dashpots act in parallel with the existing contact model and provide forces that are proportional to the relative velocity difference between the two contacting entities (ball-ball or ball-wall).

For compact assemblies, local damping, using the default parameter setting in PFC3D, is the most appropriate form to establish equilibrium and to conduct quasi-static deformation simulations (Itasca, 2008).

3.5 Contact models

The constitutive behavior of a material is simulated in PFC3D by associating a contact model with each contact. In addition to the contact model, there may also be a parallel bond. These components define the contact force-displacement behavior. PFC3D provides two standard contact models (linear and Hertz) and several alternative contact models. The linear contact model and the parallel bond model were used in this research that are described in Sections 3.5.1 and 3.5.2, respectively.

3.5.1 Linear contact model

The linear contact model can be envisioned as linear normal and shear springs and represents the load displacement relationship between two contacting bodies. The input parameters of the linear contact model are the particle normal and shear stiffnesses, K^N and K^S , respectively, and the inter-particle friction coefficient, μ .

The contact stiffness (normal or shear), K , between the contacting bodies (A and B) can be calculated from the particle normal or shear stiffness, K_A and K_B , as follows

$$K = \frac{K_A \times K_B}{K_A + K_B} \quad (3.24)$$

The normal and shear contact forces, F_i^n and F_i^s are calculated using Eqs. (3.6) and (3.14), respectively.

Slip behavior is also provided by enforcing a relationship between shear and normal force, such that the two contacting entities may slip relative to one another. The relation provides no normal strength in tension and allows slip to occur by limiting the shear force.

The contact is checked for slip conditions by calculating the maximum allowable shear contact force

$$F_{max}^s = \mu |F_i^n| \quad (3.25)$$

If $|F_i^s| > F_{max}^s$ then slip is allowed to occur by setting the magnitude of F_i^s equal to F_{max}^s .

3.5.2 Parallel bond model

In addition to the contact model, there may also be a parallel bond, which is meant to mimic the behavior of the cementitious material deposited between particles. It acts as a set of springs with normal and shear stiffnesses as well as shear and tensile strengths that work in parallel with the contact model. A parallel-bond can transmit both forces and moments providing a stiffer system at the contact and restricting the contacting particles from rolling.

Potyondy and Cundall (2004) concluded that the parallel bond model could be an appropriate model for modeling rock such as granite. Later Fakhimi and Villegas (2007) used the model to analyze sandstone response to loading.

The following five parameters are required to define a parallel bond: parallel bond normal and shear stiffnesses, k_{pb}^n and k_{pb}^s (stress/displacement); normal and shear

strengths, S_{pb}^n and S_{pb}^s (stress); and the radius multiplier used to set the parallel bond radius, α .

\bar{F}_i and \bar{M}_i denote the total force and moment associated with the parallel bond, respectively, with the convention that this force and moment represent the action of the bond on Ball B of Figure 3.5.

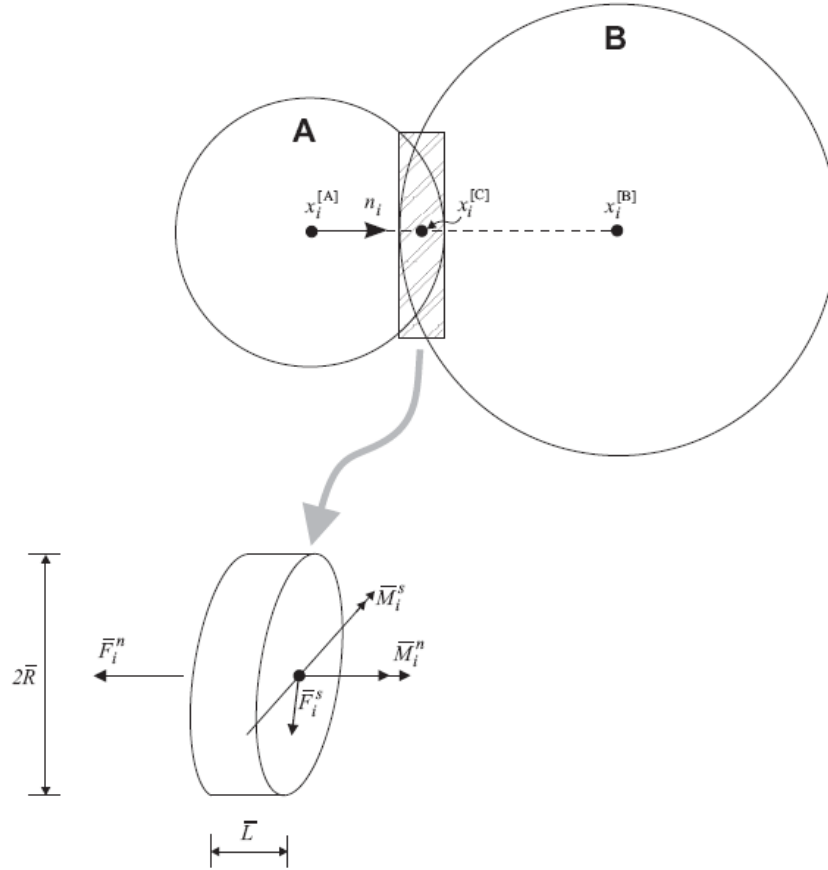


Figure 3.5 Parallel bond representation (Itasca, 2008)

Each of these vectors can be decomposed into normal and shear components with respect to the contact plane as (Figure 3.5)

$$\begin{aligned}\bar{F}_i &= \bar{F}_i^n + \bar{F}_i^s \\ \bar{M}_i &= \bar{M}_i^n + \bar{M}_i^s\end{aligned}\tag{3.26}$$

The normal component vectors can be expressed in terms of the scalar values \bar{F}^n and \bar{M}^n via

$$\begin{aligned}\bar{F}_i^n &= \bar{F}^n n_i \\ \bar{M}_i^n &= \bar{M}^n n_i\end{aligned}\tag{3.27}$$

When the bond is formed, \bar{F}_i and \bar{M}_i are initialized to zero. Each subsequent relative displacement and rotation-increment at the contact results in an increment of elastic force and moment that is added to the current values. The elastic force-increments and the elastic moment-increments occurring over a time step of Δt are calculated by

$$\begin{aligned}\Delta \bar{F}_i^n &= (-k_{pb}^n A \Delta U^n) n_i \\ \Delta \bar{F}_i^s &= -k_{pb}^s A \Delta U_i^s \\ \text{with } \Delta U_i &= V_i \Delta t \\ \Delta \bar{M}_i^n &= (-k_{pb}^s J \Delta \theta^n) n_i \\ \Delta \bar{M}_i^s &= -k_{pb}^n I \Delta \theta_i^s\end{aligned}\tag{3.28}$$

$$\text{with } \Delta \theta_i = \left(\omega_i^{[B]} - \omega_i^{[A]} \right) \Delta t$$

where the contact velocity is calculated using Eq. (3.11); A is the area of the bond disk; J is the polar moment of inertia of the disk; and I is the moment of inertia of the disk cross section about an axis through the contact point in the direction of $\Delta \theta_i^s$.

The parameters are given by

$$\begin{aligned}A &= \pi \bar{R}^2 \\ J &= \frac{1}{2} \pi \bar{R}^4 \\ I &= \frac{1}{4} \pi \bar{R}^4\end{aligned}\tag{3.29}$$

$$\text{with } \bar{R} = \alpha \min(R_A, R_B)$$

The new force and moment vectors associated with the parallel bond are found by summing the old values existing at the start of the time step with the elastic force- and moment-increment vectors.

Using the beam theory, the maximum tensile and shear stresses acting on the bond periphery are calculated by

$$\begin{aligned}\sigma_{max} &= \frac{-\bar{F}^n}{A} + \frac{|\bar{M}_i^s|}{I} \bar{R} \\ \tau_{max} &= \frac{|\bar{F}_i^s|}{A} + \frac{|\bar{M}^n|}{J} \bar{R}\end{aligned}\quad (3.30)$$

If the maximum tensile stress exceeds the normal strength ($\sigma_{max} \geq S_{pb}^n$) or the maximum shear stress exceeds the shear strength ($\tau_{max} \geq S_{pb}^s$), then the parallel bond breaks.

If the bond remains intact, then the contribution of the final force and moment vectors to the resultant force and moment on each of the two balls is given by

$$\begin{aligned}F_i^{[A]} &\leftarrow F_i^{[A]} - \bar{F}_i \\ F_i^{[B]} &\leftarrow F_i^{[B]} + \bar{F}_i \\ M_i^{[A]} &\leftarrow M_i^{[A]} - e_{ijk} (x_j^{[C]} - x_j^{[A]}) \bar{F}_k - \bar{M}_i \\ M_i^{[B]} &\leftarrow M_i^{[B]} + e_{ijk} (x_j^{[C]} - x_j^{[B]}) \bar{F}_k + \bar{M}_i\end{aligned}\quad (3.31)$$

where $F_i^{[\Phi]}$ and $M_i^{[\Phi]}$ are the total force and moment for particle Φ .

Potyondy and Cundall (2004) concluded that the particle and parallel bond stiffnesses can be considered independent of particle size using Young's modulus of the particle and the parallel bond, E_c and E_{pb} , respectively, and the ratio of normal to shear stiffness of the particle and the parallel bond, $\frac{K^n}{K^s}$ and $\frac{k_{pb}^n}{k_{pb}^s}$, respectively.

$$\begin{aligned}K_\emptyset^n &= 4R^{[\emptyset]} E_c \\ K_\emptyset^s &= \frac{K_\emptyset^n}{\frac{K^n}{K^s}} \\ k_{pb}^n &= \frac{E_{pb}}{R^{[A]} + R^{[B]}}\end{aligned}\quad (3.32)$$

$$K_{pb}^s = \frac{K_{pb}^n}{\frac{k_{pb}^n}{k_{pb}^s}}$$

3.6 Interpretation techniques

The DEM model computes contact forces between the particles and particle displacements and rotations. These quantities are useful when studying the material behavior at the microscale, but they cannot be transferred directly to a continuum model. Therefore to interpret the results, it is essential to evaluate macro continuum quantities, such as porosity, stress, and strain, using the particle-scale results. This can be done by performing a statistical averaging technique over a representative volume.

3.6.1 Coordination number

The coordination number, N , is the average number of contacts per particle and is computed as

$$N = \frac{2N_c}{N_p} \quad (3.33)$$

where N_c and N_p are the number of contacts and particles, respectively, within the measurement region.

3.6.2 Porosity

The porosity, n , is defined as the ratio of total void volume, V^{void} , within the measurement domain to the measurement-region volume, V^{reg} , as follows

$$n = \frac{V^{void}}{V^{reg}} = 1 - \frac{V^{mat}}{V^{reg}} \quad (3.34)$$

where V^{mat} is the volume of material in the measurement region that is calculated by

$$V^{mat} = \sum_{N_p} V^{(P)} - \sum_{N_c} V^{(c)} \quad (3.35)$$

where N_p is the number of particles that lie fully within or intersect the measurement region; $V^{(P)}$ is the volume of particle P given by Eq. (3.36); N_c is

the number of active contacts that lie in the measurement region; and $V^{(c)}$ is the overlap volume of the two particles at contact c .

The particle volume is given by

$$V^{(P)} = \frac{4}{3}\pi R^3 \quad (3.36)$$

3.6.3 Stress

The average stress, $\bar{\sigma}_{ij}$, in a specific region of the material with known volume, V , is calculated as

$$\bar{\sigma}_{ij} = \frac{1}{V} \int_V \sigma_{ij} dV \quad (3.37)$$

where σ_{ij} is the stress acting throughout the volume. For a particulate material consisting of spherical particles, stresses exist only in these bodies; thus, the integral can be replaced by a sum over the N_p particles contained within V as

$$\bar{\sigma}_{ij} = \frac{1}{V} \sum_{N_p} \bar{\sigma}_{ij}^{(P)} V^{(P)} \quad (3.38)$$

where $\bar{\sigma}_{ij}^{(P)}$ is the average stress in particle P . In a similar way, the average stresses in each body, P , can be written as

$$\bar{\sigma}_{ij}^{(P)} = \frac{1}{V^{(P)}} \int_{V^{(P)}} \sigma_{ij}^{(P)} dV^{(P)} \quad (3.39)$$

The identity

$$S_{ij} = (x_i S_{kj})_{,k} - x_i S_{kj,k} \quad (3.40)$$

holds for any tensor S_{ij} . Applying this identity to the stress in each body results in

$$\bar{\sigma}_{ij}^{(P)} = \frac{1}{V^{(P)}} \int_{V^{(P)}} \left[(x_i \sigma_{kj}^{(P)})_{,k} - x_i \sigma_{kj,k}^{(P)} \right] dV^{(P)} = \frac{1}{V^{(P)}} \{ (I_{ij})_1 - (I_{ij})_2 \} \quad (3.41)$$

The first integral is rewritten as a surface integral by applying the Gauss divergence theorem such that

$$(I_{ij})_1 = \int_{V^{(P)}} \left[(x_i \sigma_{kj}^{(P)})_{,k} \right] dV^{(P)} = \int_{S^{(P)}} x_i \sigma_{kj}^{(P)} n_k dS^{(P)} = \int_{S^{(P)}} x_i t_j^{(P)} dS^{(P)} \quad (3.42)$$

where $S^{(P)}$ is the body surface; n_k is the unit outward normal to the surface; and $t_j^{(P)}$ is the traction vector. If the moment carried by each parallel bond is neglected, then each body is loaded by point forces acting at discrete contact locations, and the above integral can be replaced by a sum over the $N_c^{(P)}$ contacts as

$$(I_{ij})_1 = \sum_{N_c^{(P)}} x_i^{(c)} F_j^{(c,P)} \quad (3.43)$$

where $x_i^{(c)}$ is the location and $F_j^{(c,P)}$ is the force acting on body (P) at contact (c). $F_j^{(c,P)}$ includes both the contact and parallel-bond forces.

The contact locations can be expressed as

$$x_i^{(c)} = x_i^{(P)} + (x_i^{(c)} - x_i^{(P)}) \quad (3.44)$$

where $x_i^{(P)}$ is the location of the particle centroid. By substituting Eq. (3.44) into Eq. (3.43), we have

$$(I_{ij})_1 = \sum_{N_c^{(P)}} x_i^{(P)} F_j^{(c,P)} + \sum_{N_c^{(P)}} (x_i^{(c)} - x_i^{(P)}) F_j^{(c,P)} \quad (3.45)$$

In the absence of body forces and externally applied forces, the equation of motion for body (P) is

$$\sigma_{kj,k} = \rho a_j = \frac{F_j}{V} \quad (3.46)$$

where ρ is density; a_j is the acceleration; and F_j is the resultant force acting at the center of the particle. This equation allows us to rewrite the second integral as

$$(I_{ij})_2 = \int_{V^{(P)}} [x_i \sigma_{kj,k}^{(P)}] dV^{(P)} = F_j^{(P)} x_i^{(P)} \quad (3.47)$$

By substituting Eqs. (3.47) and (3.45) into Eq. (3.41) and combining with Eq. (3.38), the average stress in a measurement region is given by

$$\bar{\sigma}_{ij} = \left(\frac{1-n}{\sum_{N_P} V^{(P)}} \right) \left(\sum_{N_P} \sum_{N_c^{(P)}} (x_i^{(c)} - x_i^{(P)}) F_j^{(c,P)} \right) \quad (3.48)$$

3.6.4 Strain rate

The procedure used to measure local strain rate within a region differs from that used to measure stress. This is because it is incorrect to use the velocities in a similar way to evaluate the average strain rate, since the velocities in the voids are nonzero.

O’Sullivan et al. (2003) carried out a review on the methods that have been used to calculate the strains within a granular medium from the particle displacements and rotations from DEM simulations. In the current study, the strain calculation method proposed by Potyondy and Cundall (2004) has been used. In this method, instead of assuming a velocity field in the voids, a strain-rate tensor is determined based on a best-fit procedure that minimizes the error between the predicted and measured velocities of all balls with centroids contained within the measurement sphere (Potyondy and Cundall, 2004). The strain-rate tensor components are obtained by solving the following matrix

$$\begin{bmatrix} \sum_{N_p} \tilde{x}_1^{(P)} \tilde{x}_1^{(P)} & \sum_{N_p} \tilde{x}_2^{(P)} \tilde{x}_1^{(P)} & \sum_{N_p} \tilde{x}_3^{(P)} \tilde{x}_1^{(P)} \\ \sum_{N_p} \tilde{x}_1^{(P)} \tilde{x}_2^{(P)} & \sum_{N_p} \tilde{x}_2^{(P)} \tilde{x}_2^{(P)} & \sum_{N_p} \tilde{x}_3^{(P)} \tilde{x}_2^{(P)} \\ \sum_{N_p} \tilde{x}_1^{(P)} \tilde{x}_3^{(P)} & \sum_{N_p} \tilde{x}_2^{(P)} \tilde{x}_3^{(P)} & \sum_{N_p} \tilde{x}_3^{(P)} \tilde{x}_3^{(P)} \end{bmatrix} \begin{bmatrix} \dot{\alpha}_{i1} \\ \dot{\alpha}_{i2} \\ \dot{\alpha}_{i3} \end{bmatrix} = \begin{bmatrix} \sum_{N_p} \tilde{V}_i^{(P)} \tilde{x}_1^{(P)} \\ \sum_{N_p} \tilde{V}_i^{(P)} \tilde{x}_2^{(P)} \\ \sum_{N_p} \tilde{V}_i^{(P)} \tilde{x}_3^{(P)} \end{bmatrix} \quad (3.49)$$

where $\dot{\alpha}_{ij}$ is the velocity-gradient tensor which is referred to the strain-rate tensor and $\tilde{V}_i^{(P)}$ and $\tilde{x}_i^{(P)}$ are the mean relative velocity and centroid location values for the N_p particles within a measurement region, respectively.

3.7 Initial and boundary conditions

In PFC3D, boundary and initial conditions can be specified for both walls and balls. For each ball, either the applied force and/or moment acting through its center or the initial velocity can be specified. The applied force and/or moment are added to the contact force and moment acting on the particles throughout the simulation. If the ball velocities are specified, boundary forces will be altered automatically during the next time step, based on the contact forces and the integration of the law of motion.

These basic boundary conditions cannot be easily and practically applied to a system with thousands of particles. Consequently, in DEM simulations the most widely employed boundary type is a rigid boundary. These rigid boundaries are described by surfaces that can be planar or curved. They have no inertia, thus the contact forces determined at ball-wall contacts are only used to update the particle coordinates. Therefore, they are similar to displacement boundary conditions used in the FEM, and they are suitable to model the rigid top and bottom platens in triaxial tests.

In addition, the numerical servo-controlled mechanism can be used to control the wall velocity in order to maintain a specific wall stress. The wall stress arises from the particles in the assembly that are in contact with the wall and is given by

$$\sigma^{(\omega)} = \frac{\sum N_c F^{(\omega)}}{A} \quad (3.50)$$

where $F^{(\omega)}$ is the force applied by a particle on the wall; A is the area of the wall that is in contact with the particle assembly; and N_c is the number of particles that are in contact with the wall.

The wall velocity is adjusted in such a way as to reduce the difference between the current wall stress and the desired target wall stress, $\sigma^{(t)}$. The wall velocity is given by

$$\dot{u}^{(\omega)} = G(\sigma^{(\omega)} - \sigma^{(t)}) = G\Delta\sigma \quad (2.51)$$

where G is the gain parameter.

In order to avoid oscillation and instability in the system, the absolute value of the change in the wall stress must be less than the absolute value of the difference between the measured and target stresses. This condition implies a restriction on choosing the gain parameter, which is given by

$$G \leq \frac{\alpha A}{K_n \Delta t} \quad (3.52)$$

where α is the relaxation factor (set to 0.5 by default) and K_n is the sum of the contact stiffnesses of all contacts with the wall.

3.8 Relationship between micro-parameters of the parallel bond model and actual micro-properties

It is not practical to model every single grain in the DEM simulations with the current computational power. Therefore, the DEM material consists of particles that represent rock volumes rather than individual grains. Thus, the particle micro-properties of the DEM model (e.g., K^n and k^s) represent the properties of an assembly of grains rather than single grains.

Further, PFC3D uses spherical particles to model the particulate media. Generally speaking, the shape of natural granular materials such as sandstone is non-spherical or irregular. The non-spherical shape of particles results in resistance to particle rotation and slip while in the PFC3D model, the spherical particles can rotate with less resistance. Therefore, the inter-particle friction coefficient in the PFC3D model should be selected higher than the actual friction coefficient at the actual grain contacts for an improved representation of the inter-particle friction.

The parallel bonds provide the force-displacement behavior of a finite-sized piece of cementitious material deposited between two particles. These bonds act in parallel with the contact-bond model described above. Inter-particle forces are thus deemed to be partly transferred through the particle contacts and partly through the cement bonding between the particles.

3.9 Conclusions

DEM models can provide valuable information on the interaction between particles in granular materials. DEM analyses have made significant contributions to advance the understanding of soil and rock responses.

The parallel bond models are able to transmit both forces and moments just as the cementing materials do at real contacts. The input parameters of the parallel bond DEM model are the particle and cement micro-properties. Particle micro-properties consist of the particle contact modulus (E_c), the ratio of normal to shear stiffness of the particles ($\frac{K^N}{K^S}$), and the particle friction coefficient (μ). The cement micro-properties are Young's modulus of the cement (E_{pb}), the ratio of normal to

shear stiffness of the cement ($\frac{K_{pb}^N}{K_{pb}^S}$), the radius multiplier used to set the parallel bond radius (α), and the normal and shear strengths of the cement (S_{pb}^N and S_{pb}^S , respectively). These parameters have to be determined from calibration studies that will be elaborated on the next chapter.

Chapter 4: Systematic calibration procedure for DEM parallel bond models

4.1 Introduction

In the parallel bond DEM models, the micro-properties cannot be determined by direct measurements of the macro responses on the laboratory specimens. It can be found by means of a calibration process in which a particular assembly of particles with a set of micro-parameters is used to simulate a set of material tests, and the micro-parameters then are evaluated to reproduce the macro responses measured in such tests (Potyondy and Cundall, 2004). The calibration procedure is challenging for the 3D bonded particle model. There may be several variations in the parameters, and it is difficult to conclude which set of parameters is most appropriate for the material.

Fakhimi and Villegas (2007) and Yoon (2007) proposed a calibration procedure relating the micro-properties to macro-properties of the material for 2D DEM analyses. Alassi and Holt (2011) also derived micro-macro relations to determine the particle contact normal stiffness (K^N) and shear stiffness (K^S) in terms of macro Young's modulus and Poisson's ratio. To simplify the problem, they assumed simple packing (e.g., hexagonal packing with a constant particle size and square packing) to represent the granular media in 2D. They used a contact bond model in which the contact normal stiffness and shear stiffness are related to macro elastic properties. Their model is only applicable to uncemented materials. Also, the validity of calibrating a 2D DEM model against 3D experimental data needs to be addressed.

Kulatilake et al. (2001) suggested a calibration procedure for a jointed block of rock under uniaxial loading using PFC3D. They only used the contact bond model in PFC3D and evaluated the contact model micro-properties using the macro response of the material under uniaxial loading. The normal contact stiffness was related to Young's modulus of the specimen, and the normal contact strength between the particle contacts was related to the tensile strength of the specimen. The shear contact stiffness and strength were assumed to be half and equal to the

corresponding normal components. In the sensitivity analysis section, we will show these assumptions highly affect the Poisson's ratio and the peak stress in the simulation of triaxial tests.

Tawadrous et al. (2009) used artificial neural networks to predict the micro-properties of the parallel bond model in PFC3D to reproduce macro-properties of rock samples in uniaxial compression tests. To simplify the problem, they made the following assumptions: (1) the particle contact modulus is the same as the parallel bonds modulus; (2) the normal and shear bond strengths are equal; and (3) the friction between particles is a constant parameter, and it is equal to 2.5. Again, we will show that these assumptions could highly affect the macro response of the material. Further, they investigated the effect of micro-properties on only the macro Young's modulus, Poisson's ratio, and uniaxial compressive strength (UCS). The effects of micro-properties on the hardening/softening behavior were not studied in their work.

Belheine et al. (2008) suggested a calibration procedure for a 3D spherical discrete model with rolling resistance. They generated the numerical model of Labenne sand using a DEM code called SDEC, and the micromechanical properties of the numerical model were calibrated to match the macro response of the real sand.

Potyondy and Cundall (2004) studied the influence of micromechanical properties on the macroscopic response of simulated triaxial tests. Their main findings are summarized below:

- The macro Young's modulus of the specimen is mainly governed by the particle contact modulus and the cement Young's modulus. The Poisson's ratio of a parallel-bonded specimen is influenced by the ratio between the total shear stiffness and the total normal stiffness.
- The parallel bond strengths affect the peak mobilized stress of the specimen.
- The particle friction coefficient mainly governs the post-peak behavior.

We have used these findings in our calibration study and have tested their validity by conducting a sensitivity analysis, which will be elaborated on later.

This chapter describes a method adopted to determine the 3D parallel bond model parameters required to capture the response of natural sandstones in triaxial tests under different confining stresses through a model calibration process. The calibration process is non-trivial as the parameters that are needed typically cannot be directly related to any standard experimental measurements, and each parameter is not independently related to a single macro-behavior property.

The calibration process is verified against analytical solutions developed by Risnes et al. (1982) and validated against laboratory data. This chapter is based on a series of triaxial and TWC tests performed on samples of SWS sandstone.

4.2 Calibration process

The set of DEM input parameters required to capture the macro-scale response of the rock was selected using the existing knowledge in the literature and methodological trial and error to match the DEM response with the laboratory measurements. The calibration was validated against a series of triaxial tests performed on SWS sandstone. Figure 4.1 shows the result of drained triaxial tests conducted at confining stresses of 0, 6.8, 13.8, 24.1, and 48 MPa.

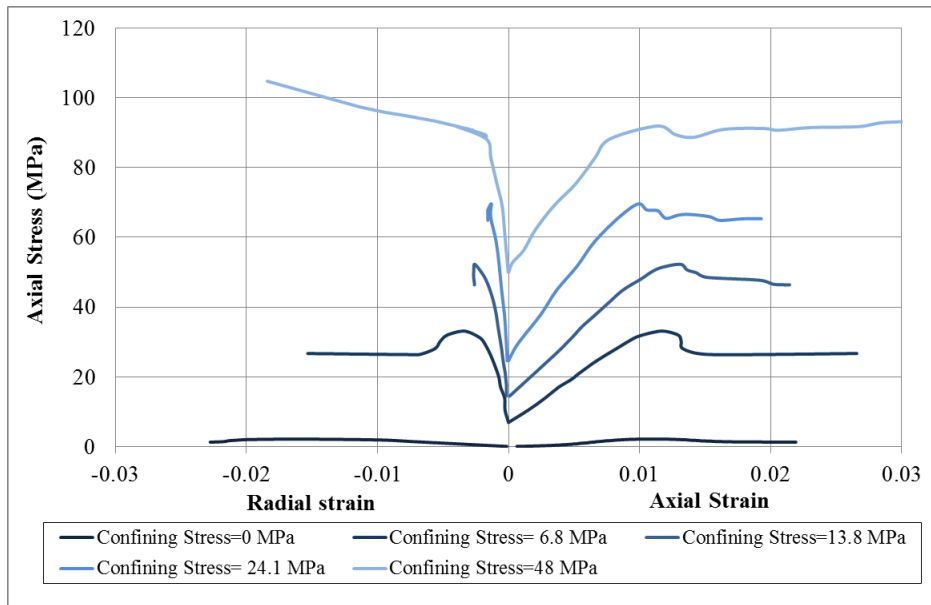


Figure 4.1 Stress-strain curves for SWS sandstone at different confining stresses

4.2.1 Specimen generation

It is not practical to model every single grain in the DEM simulations with the current computational power. Therefore, particles that represent rock volumes rather than individual grains are modeled in DEM. Potyondy and Cundall (2004) concluded that the macro response of a 3D DEM model can be very sensitive to the number of particles. It becomes less sensitive when the number of particles increases. In our simulation, the mean particle size was selected such that more than 20 particles were generated across the width of the triaxial sample (Cheung, 2010).

In previous DEM modeling studies, many researchers did not capture the particle size distribution (PSD) of the real material (e.g., Cho et al., 2007; Holt et al., 2005; Potyondy and Cundall, 2004; Wang et al., 2003). They assumed even distribution of the sizes of DEM particles between the radius of the largest and smallest particles. They used a D_{\max}/D_{\min} ratio between 1.2 and 2, giving almost a uniform graded material, which could significantly differ from the actual PSD. Schöpfer et al. (2009), by numerical simulation of triaxial tests using DEM, concluded that the PSD affects the elasticity and strength of the specimen. In this simulation, a uniform PSD with D_{\max}/D_{\min} of 4.76 was chosen, which approximately captures the PSD of SWS sandstone (Figure 4.2).

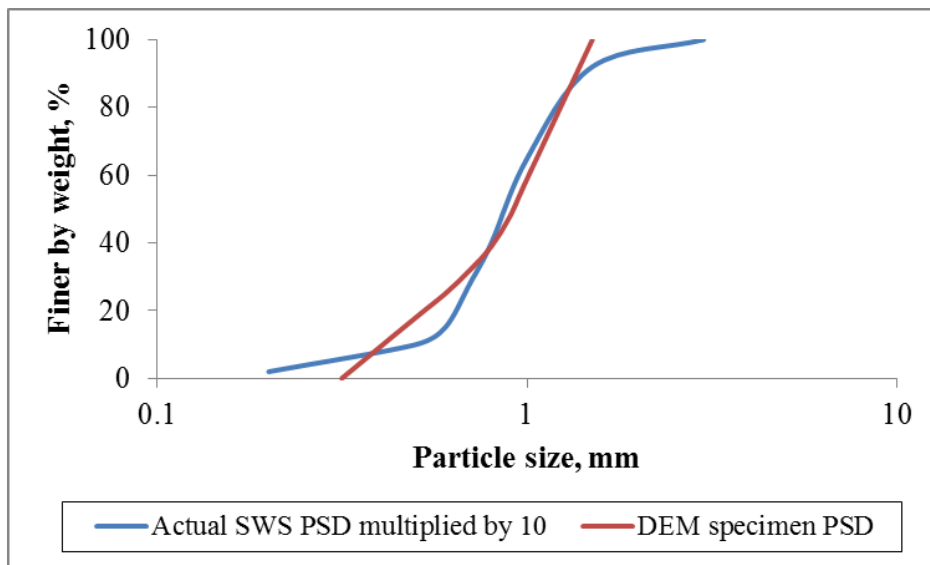


Figure 4.2 Comparison between the actual SWS PSD and the DEM specimen PSD

The DEM particles were generated randomly in a rectangular box of $0.1 \text{ m} \times 0.1 \text{ m} \times 0.2 \text{ m}$ bounded by rigid walls. To ensure initial tight packing, the particles were generated at half their final size. Then the particle diameters were increased to their final values under zero friction (frictionless balls). The walls were moved slowly using a servo control algorithm until the block reached an isotropic stress state of 20 kPa. This low value of isotropic stress is around 1% of UCS, and it was chosen to reduce the locked-in stresses that develop after subsequent parallel-bond installation (Itasca, 2008). In order to have a denser network of parallel bonds in the subsequent step, floating particles, defined as the particles with less than three contacts with other particles, were removed (Potyondy and Cundall, 2004). Next, parallel bonds were randomly installed at 40% of the contacts detected at this stage, and the bond radius multiplier was varied randomly between 0 and 1 based on the observations from the SEM images of SWS sandstone (Cheung, 2010). Then a friction coefficient was assigned to all particles.

Sazzad and Islam (2008) showed that in the contact bond model with rigid spherical particles, the friction angle at the peak strength is related to the inter-particle friction and that the macro friction angle is lower than the friction angle between the particles. They concluded that the friction angle is affected by grain angularity due to the inherent rolling resistance among non-spherical grains. However, in the parallel bond model, we show that the friction angle at peak strength is also related to the parallel bond strengths and the percentage of bonded contacts. The SWS particles are sub-rounded (Alvarado, 2007); thus, it was assumed that the friction between particles is equal to the friction angle at the peak strength of SWS sandstone ($\mu = \tan(30^\circ) = 0.58$) as the initial guess.

Finally, in order to reduce the boundary effects on the specimen generation process, a cylindrical specimen with a diameter of 50 mm and height of 100 mm was cut from the block. The specimen was bounded with cylindrical, top and bottom rigid frictionless walls as shown in Figure 4.3.

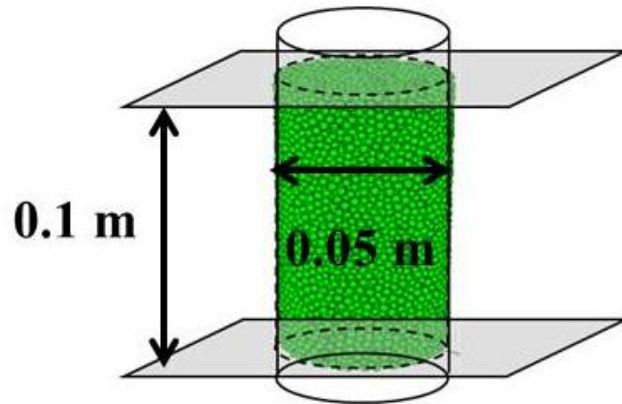


Figure 4.3 Triaxial test specimen

This resulted in a specimen with 23,450 particles, and there were approximately 24 particles across the specimen diameter. The average porosity of the DEM specimen was assessed to be 0.32, which is more than the actual porosity (0.29). This is partly because the parallel bond representing the cement between grains is represented as a set of springs with no volume. Moreover, the particles in PFC3D are spherical, whereas in real sandstones, they usually have irregular shapes. This could also affect the packing and therefore the initial porosity of the specimen.

4.2.2 Calibration of the micromechanical parameters

As discussed previously, calibration of the DEM model parameters was based on trial and error and comparison of laboratory and simulated triaxial tests. In order to minimize the number of iterations, a calibration sequence was developed, which will be discussed in Section 4.7.

The set of DEM micro-parameters found to capture the overall behavior of SWS sandstone is summarized in Table 4.1 and Figure 4.4.

Table 4.1 Calibrated micro-parameters for the SWS sandstone DEM model

Particle properties		Parallel bond properties	
E_c	Fig. 4	E_{pb} (GPa)	7
$\frac{K^N}{K^S}$	1	$\frac{K_{pb}^N}{K_{pb}^S}$	1
μ	0.5	S_{pb}^N (MPa)	60
Particle radius (mm)	0.315 to 1.5	S_{pb}^S (MPa)	96
Particle density ρ_s (kg/m ³)	2650	λ , %	40
		α	Randomly distributed between 0 and 1

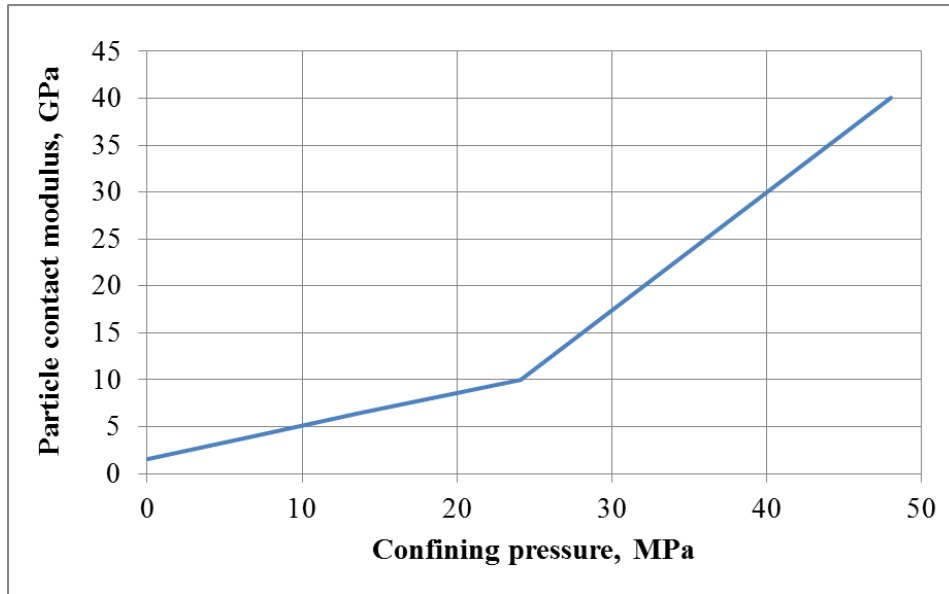


Figure 4.4 SWS sandstone micro-properties

4.3 Triaxial test simulation

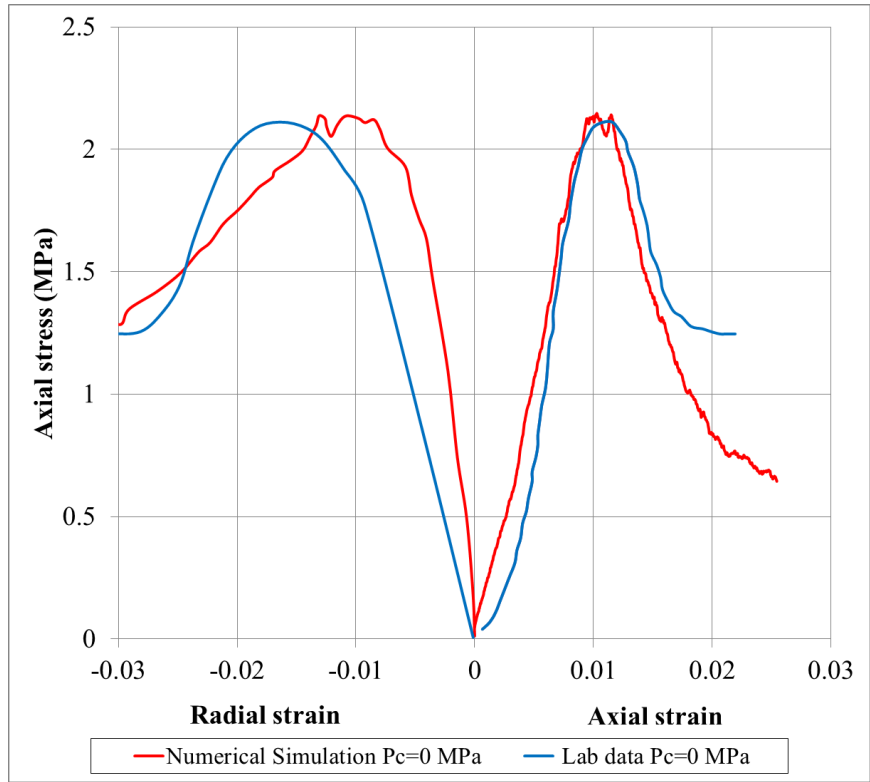
The triaxial test was performed in two stages: isotropic compression and deviatoric loading. After the DEM specimen was generated, the isotropic confining pressure was applied at all boundaries using a servo control algorithm. Then the top platen was moved downward at a velocity of 0.01 mm/sec to keep

the quasi-static condition while the base platen remained stationary. The radius of the cylindrical wall in the DEM model could be increased or decreased using a servo control system to maintain a constant lateral confining pressure.

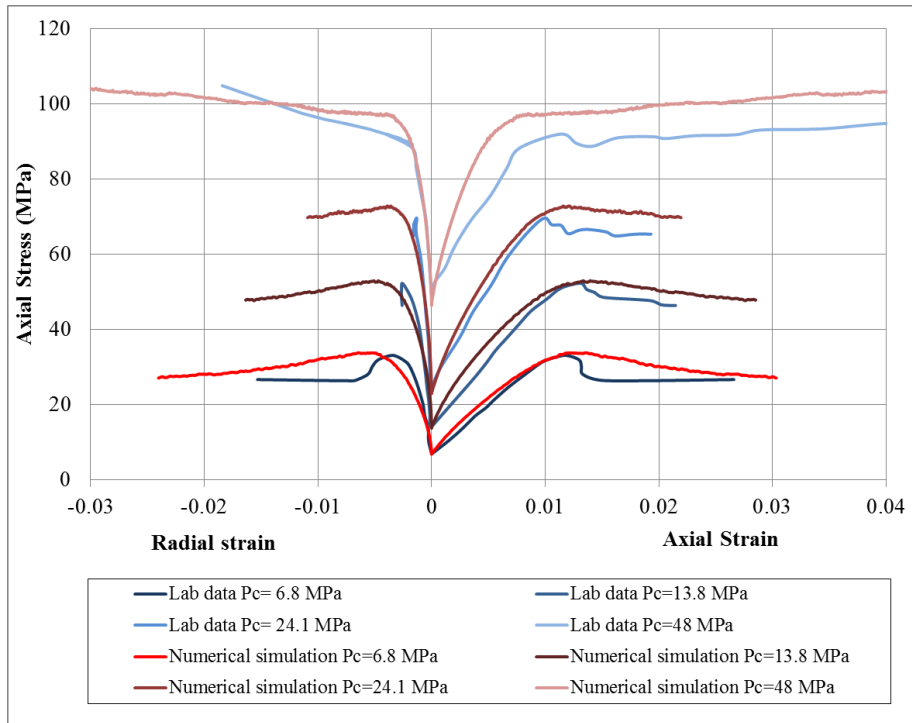
During the loading process, stresses were calculated using the forces on the DEM walls and outer boundaries of the specimen. Strains were calculated using the wall positions and gauge balls. Gauge balls were used for unconfined compressive tests, mimicking Linear Variable Displacement Transducers (LVDTs) mounted on the middle height of the specimen during the testing.

Figure 4.5 compares the macro responses of the 3D DEM model under different confining stresses with the corresponding laboratory results. The 3D DEM model for SWS sandstone reasonably captures the initial elastic response, the peak stress, and the post-peak behavior observed in physical laboratory test results.

The macromechanical properties including Young's modulus, Poisson's ratio, friction angle, cohesion, and dilation angle were measured for the laboratory data and numerical simulations. Elastic properties were determined at 50% of the peak stress (Jafarpour et al., 2012), and plastic properties were calculated at the peak stress assuming the material obeys the MC model. The dilation angle was calculated for the triaxial test with confining stress equal to 6.8 MPa (Vermeer and de Borst, 1984). The macromechanical properties for the laboratory data and calibrated numerical model are listed in Table 4.2 and Table 4.3.



(a)



(b)

Figure 4.5 Comparison between triaxial data and numerical simulations

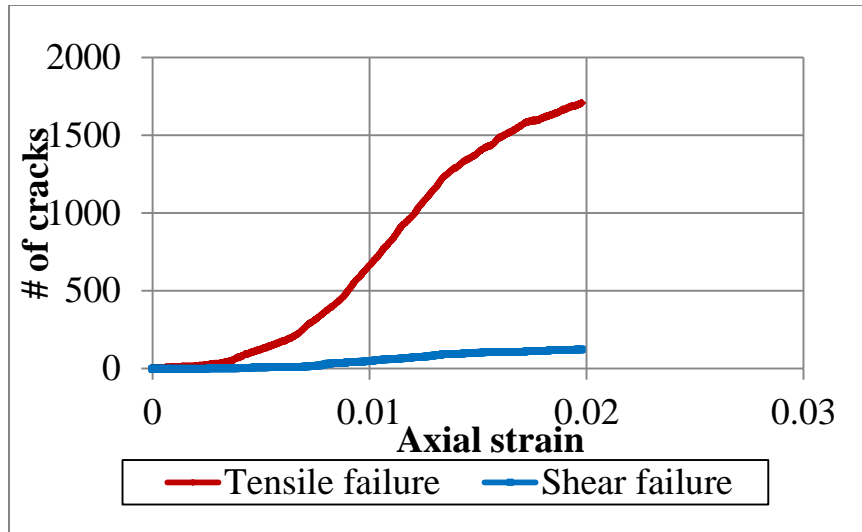
Table 4.2 Elastic properties assessed from the laboratory data and the DEM model

Confining stress (MPa)	Laboratory data		DEM model	
	Young's modulus (GPa)	Poisson's ratio	Young's modulus (GPa)	Poisson's ratio
0.0	0.17	-	0.19	0.41
6.8	2.63	0.15	3.04	0.16
13.8	3.66	0.14	4.37	0.15
24.1	5.70	0.14	6.20	0.15
48.0	5.75	0.14	6.80	0.13

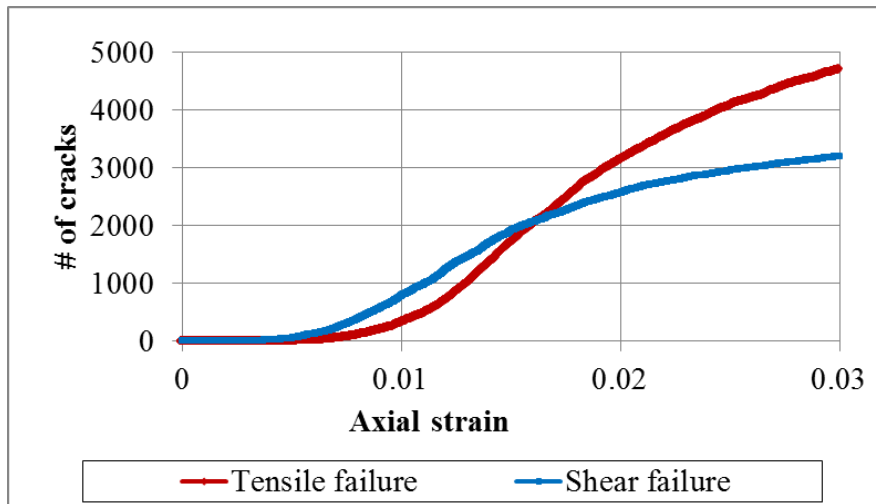
Table 4.3 Plastic properties assessed from the laboratory data and the DEM model

	Laboratory data	DEM model
Friction angle, °	30	28.5
Cohesion, MPa	2.55	2.64
Dilation angle, °	13	16

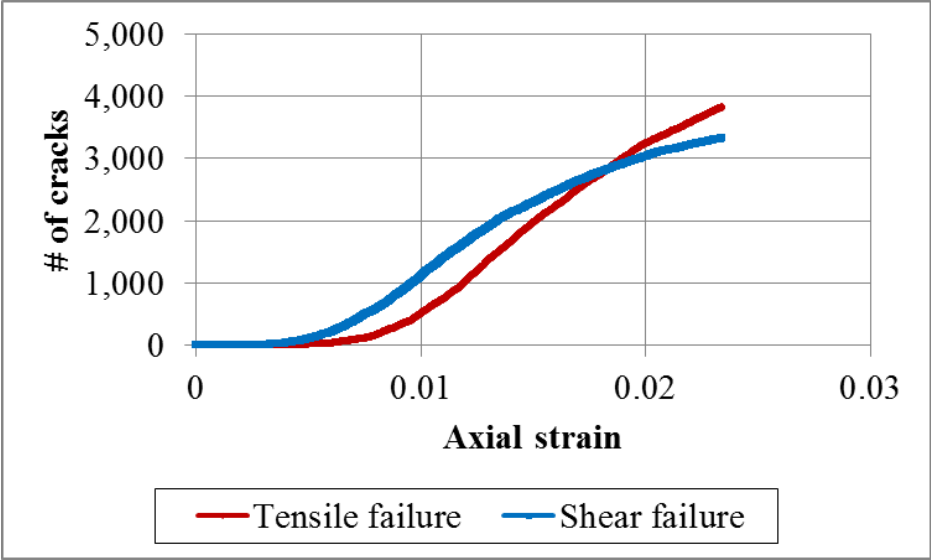
Figure 4.6 shows the number of parallel bonds that fail in either tension or shear during the loading. Prior to the peak strength, there is a significant change in parallel bonds breakage that is possibly analogous to the structural degradation of sandstone. It also shows that the parallel bonds mainly fail in tension rather than shear at low confining stresses.



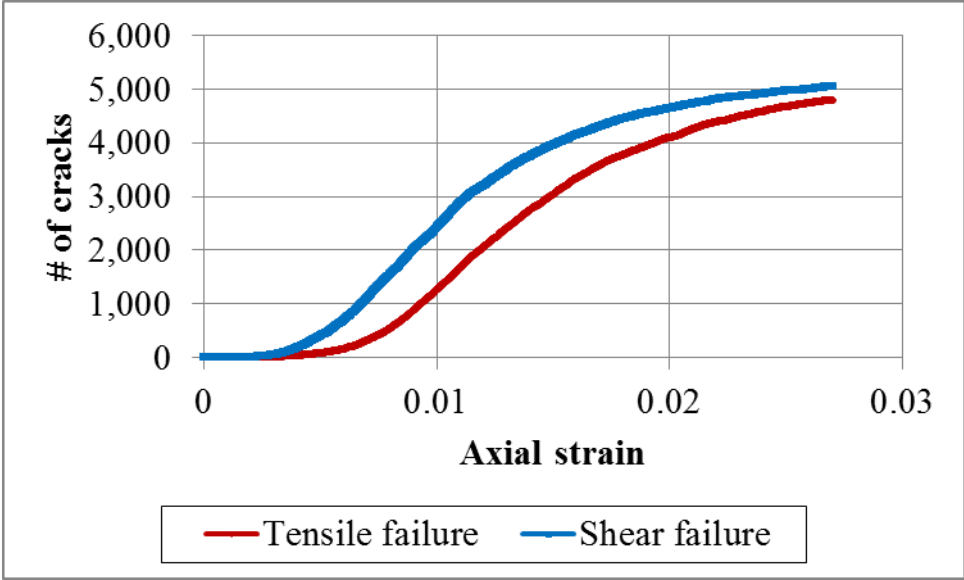
(a) Confining pressure = 0 MPa



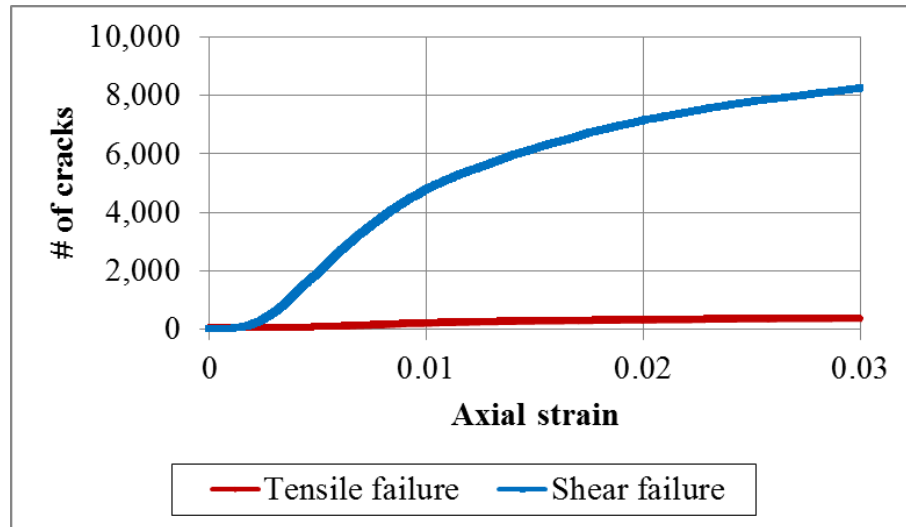
(b) Confining pressure = 6.8 MPa



(c) Confining pressure = 13.8 MPa



(d) Confining pressure = 24.1 MPa



(e) Confining pressure = 48 MPa

Figure 4.6 The number of parallel bonds that fail in either tension or shear at different confining stresses

Failure patterns at the vertical cross sections of the specimen at the peak stress (Figure 4.7) indicate that the parallel bonds fail in a relatively uniform fashion within the specimen. It can be explained by the use of a rigid cylindrical wall as the lateral boundary in the simulations, which constrains the specimen to deform uniformly and does not allow the natural development of localization bands within the specimen or barrelling of the specimen as it strains. Therefore, it may influence the post-peak behavior of the sandstone. Triaxial tests can be realistically simulated using a flexible latex membrane that allows the material to deform freely while maintaining a specified stress condition (Cheung and O’Sullivan, 2008). However, this method is computationally demanding.

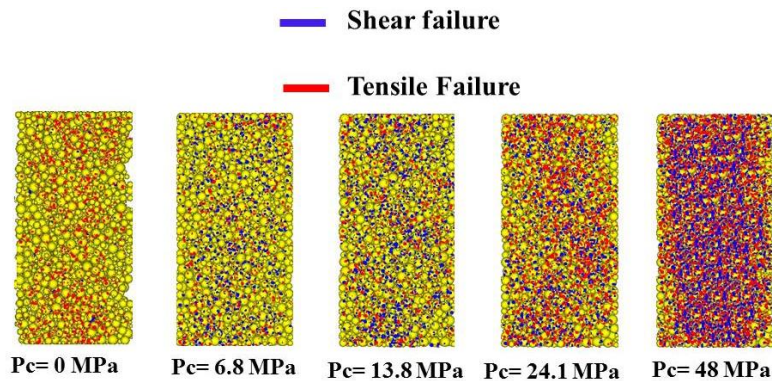


Figure 4.7 Vertical cross section of the specimen failure patterns

In Figure 4.8, particle displacement was plotted to investigate the evolution of localized deformation, which is usually developed in uniaxial compression testing. It shows the displacement vector field and failure pattern for the vertical cross section of the specimen. Both the bond failure mechanism (Figure 4.8a) and the displacement vector (Figure 4.8b) indicate axial splitting as the failure mechanism in the uniaxial compression test.

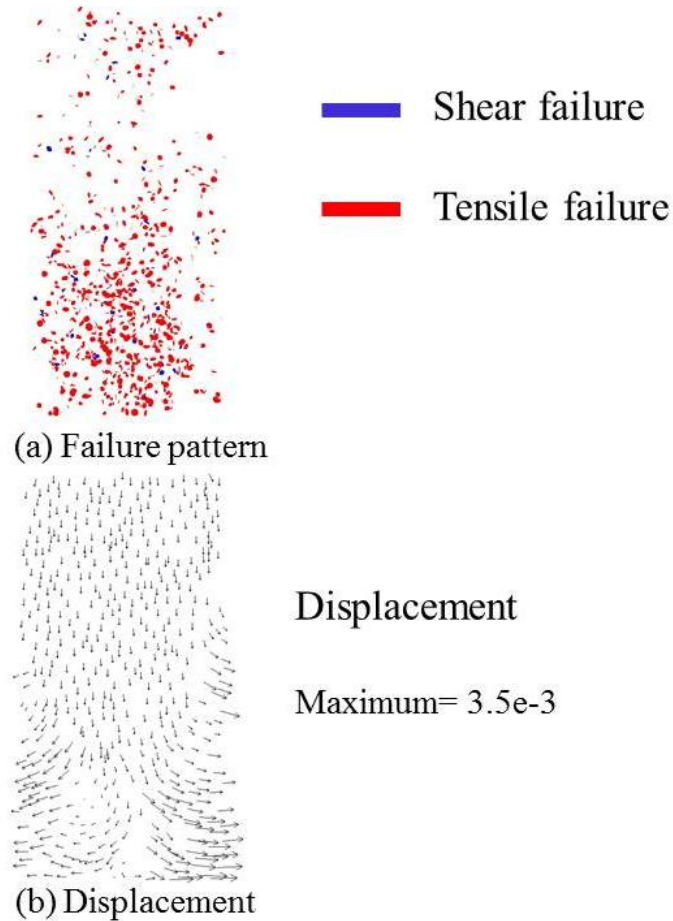


Figure 4.8 Vertical cross section of the specimen at residual strength

4.4 Verification of the calibration process

DEM simulations were conducted to verify the calibration process by comparing the DEM response with the calculated results from analytical solutions. Risnes et al. (1982) derived analytical expressions for the stresses around a wellbore or cavity by using continuum-based elasticity and plasticity theories (Appendix A).

They assumed axisymmetry and plane strain conditions and that the material obeys the MC failure criterion.

In the analytical model, a disk of SWS sandstone with an inner radius of 8 mm, outer radius of 80 mm, and unit height was chosen. The sample was also assumed to be dry. The other input parameters for the analytical solution, including cohesion, friction angle, and Poisson's ratio, were assumed to be equal to 0.65 MPa, 33° , and 0.25, respectively. The cohesion and friction angle were evaluated at peak strength from the triaxial tests at low effective confining stresses (Rahmati et al., 2012). Figure 4.9 shows the bilinear yield function of the SWS sandstone. It shows that when the minimum principal effective stress is less than 15 MPa, the yield function could be approximated by a linear yield function at the low effective confining stress. The radial stress (minimum principal stress) in the plastic region in Figure 4.10 is less than 15 MPa. Therefore, it confirms that the plastic input parameters (friction and cohesion) for the analytical model should be the plastic properties at low effective confining stress. Poisson's ratio was also assumed to be the average Poisson's ratio at different effective confining stresses. The radial stress on the inner and outer boundaries of the model were zero and 25 MPa, respectively.

Figure 4.10 shows the analytical vertical and tangential stresses. The extent of the plastic zone is defined by R_c where the peak tangential stress is observed.

The DEM model was generated by three rigid walls (two horizontal and one cylindrical) with a radius of 80 mm and height of 15 mm. The micro-parameters were the same as the parameters in the calibration for SWS sandstone. A radial stress of 25 MPa was applied to the cylindrical wall using a servo control algorithm while the top and the base platen remained stationary. Then the inner hole was drilled by removing the particles, and the model was cycled until the average unbalanced forces were low compared to the average contact forces (0.01 ratio was adopted here).

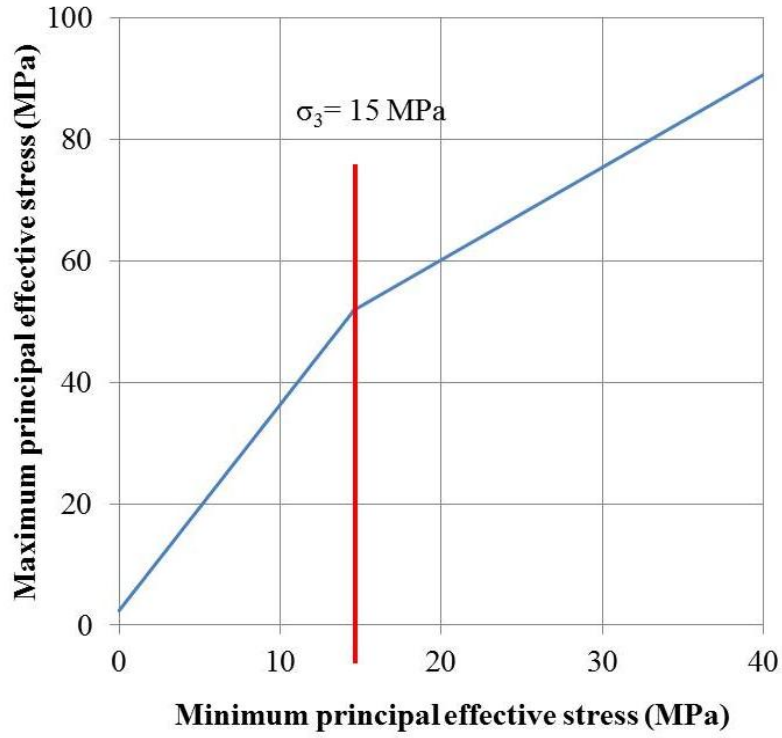


Figure 4.9 The bilinear yield function for the SWS sandstone

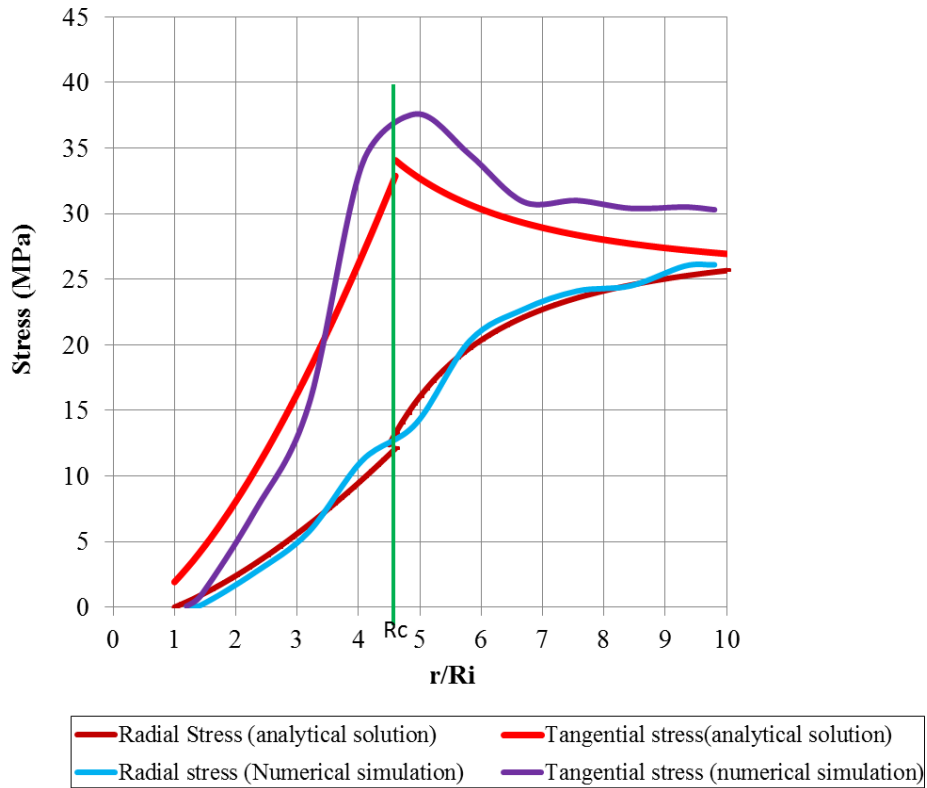


Figure 4.10 Comparison of the stresses around the wellbore between the DEM model and the analytical solution developed by Risnes et al. (1982)

Figure 4.10 compares the stresses around the wellbore of the DEM model with the analytical solution. The stress in the DEM model was calculated by performing a statistical averaging technique over a representative volume based on the algorithm described in Potyondy and Cundall (2004). The radial stress gradually increased from zero at the well face to 25 MPa at the outer boundary, and the tangential stress increased and reached a maximum value in the plastic zone and then decreased in the elastic zone. The stress values and the size of the plastic zone are in agreement with the analytical solutions. Around the inner hole, the material is degraded because of high tangential stress and a lack of radial support, resulting in broken bonds. Figure 4.11 shows the average number of contacts per particle, namely the coordination number, gradually increased in the plastic zone and reached a constant value in the intact zone. The lower value of the coordination number in the plastic zone is due to the dilation in this zone.

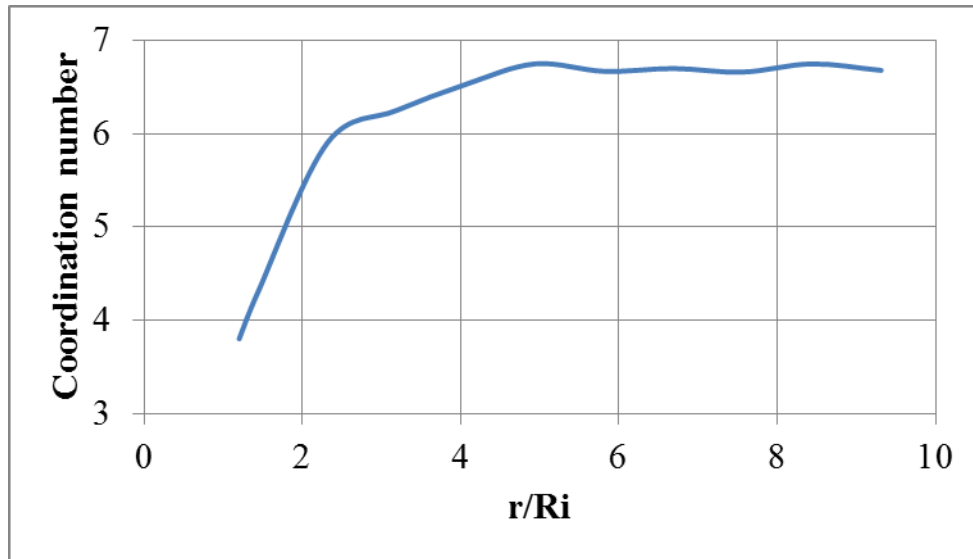


Figure 4.11 Coordination number around the hole

4.5 Validation of the calibration by simulating the TWC response

The calibration was validated against TWC measurements for SWS sandstone. The TWC test was performed on a specimen 11.02 cm in length and 5.11 cm in diameter, with a 1.81 cm hole diameter. The sample was dry, and the stresses around the outer boundaries of the specimen gradually increased until the sample collapsed. Figure 4.12 shows the laboratory results. Volumetric strain was defined

as the sum of axial strain and two radial strain measurements. The axial strain was measured at the top platen, and the radial strains were measured using Linear Variable Displacement Transducers mounted on the outer surface at the middle height of the specimen. The failure pressure was reported to be around 17.2 MPa where the volumetric strain sharply increased.

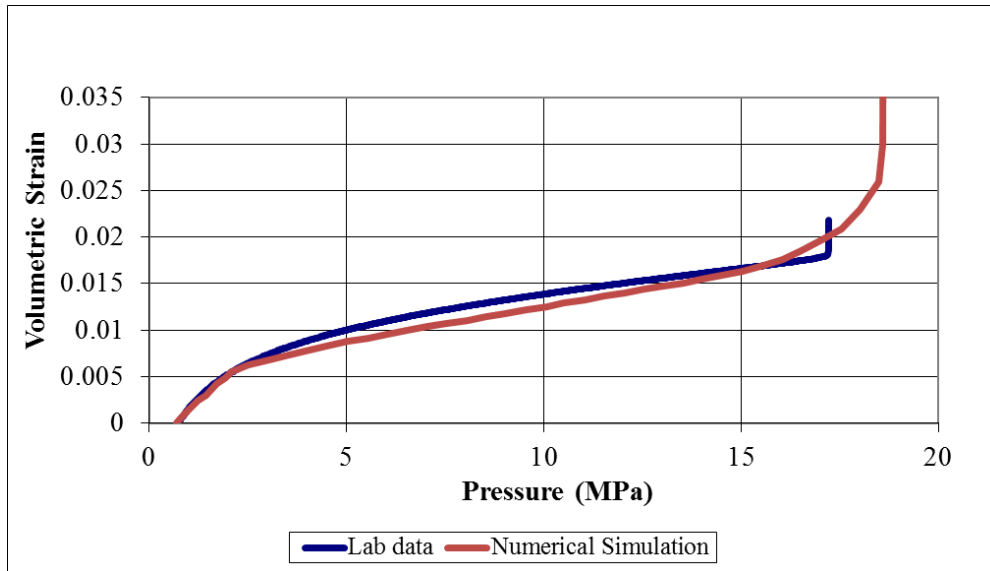


Figure 4.12 Comparison between TWC laboratory data and the numerical simulation

The TWC test was simulated using the same set of micromechanical parameters from the calibration presented in this paper. The specimen was generated, and a central hole was drilled into the sample before the loading process began in accordance with the laboratory procedures. Then the top and confining pressures were isotropically increased by moving the platens and cylindrical wall using a servo control method until collapse was detected. The collapse was determined when the pressures could not be increased further.

Figure 4.12 compares the macro response of the TWC DEM model with the laboratory results. The specimen collapse pressure was 18.7 MPa, which was in reasonable agreement with the laboratory data (17.2 MPa). The failure pattern around the hole was uniform and mainly caused by tensile failure of the bonds (Figure 4.13). Papamichos et al. (1996) predicted the same failure pattern for a weakly consolidated sandstone under isotropic loading conditions.

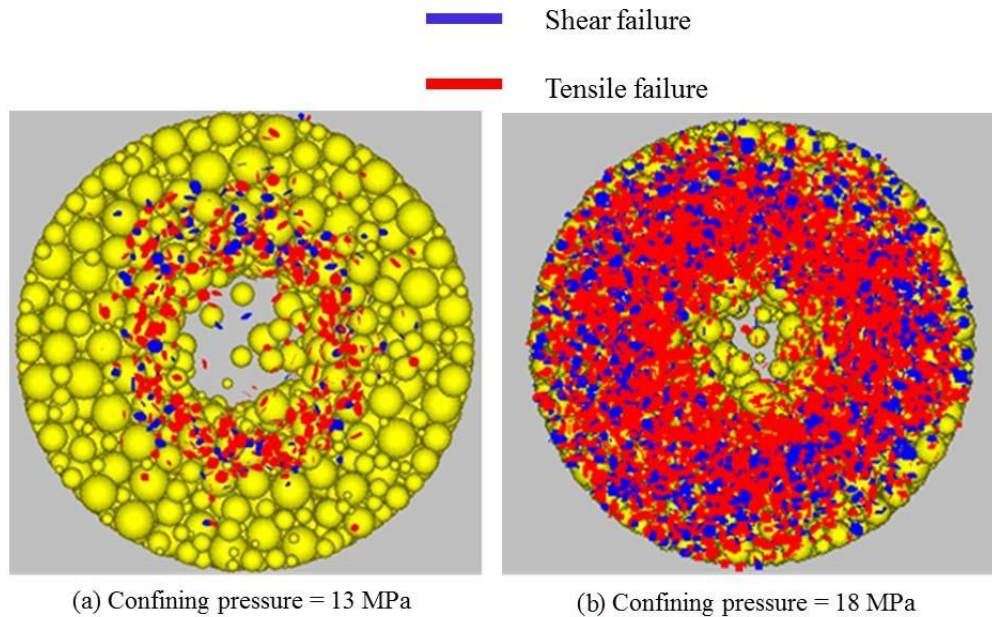


Figure 4.13 Failure pattern around the hole in TWC test for the SWS sandstone

4.6 Uniqueness of the calibration

The present approach for calibrating the micro-properties is by trial and error. With the calibration being governed by trial and error, questions of the uniqueness of the calibrated parameters and the possibility of producing another set of parameters that may result in equally good matches with the triaxial measurement arise. It is critical to know if a procedure can be developed for a systematic trial-and-error process that produces the best results for calibration.

To address the uniqueness issue, a sensitivity study of the parameters to determine the effect of each micro-property on the results was carried out. The parametric study was conducted with respect to the grain and cement stiffness, the percentage of bonded contacts, shear and tensile strength of the bonding, and the friction coefficient between the particles. The parametric study was conducted for one of the triaxial tests at a confining pressure of 6.8 MPa. The micro-parameters of the base case are the same as the calibration values reflected in Table 4.1. The parametric study is described in detail below.

4.6.1 Effect of particle contact modulus and parallel bond modulus (E_c and E_{pb})

Four simulations were carried out where E_{pb} was varied between 3 and 11 GPa.

The specimen generation method and other micro-parameters for the simulations were the same as those used in the base case simulation. In addition, the effect of the particle contact modulus (E_c) was studied by choosing $E_c = 2$ and 8 GPa.

The macro responses of the simulations are shown in Figure 4.14 and Figure 4.15, which confirmed an increase in the macro Young's modulus as E_{pb} or E_c increased. Results also indicated variation of E_c and E_{pb} only slightly affected the peak and residual strengths.

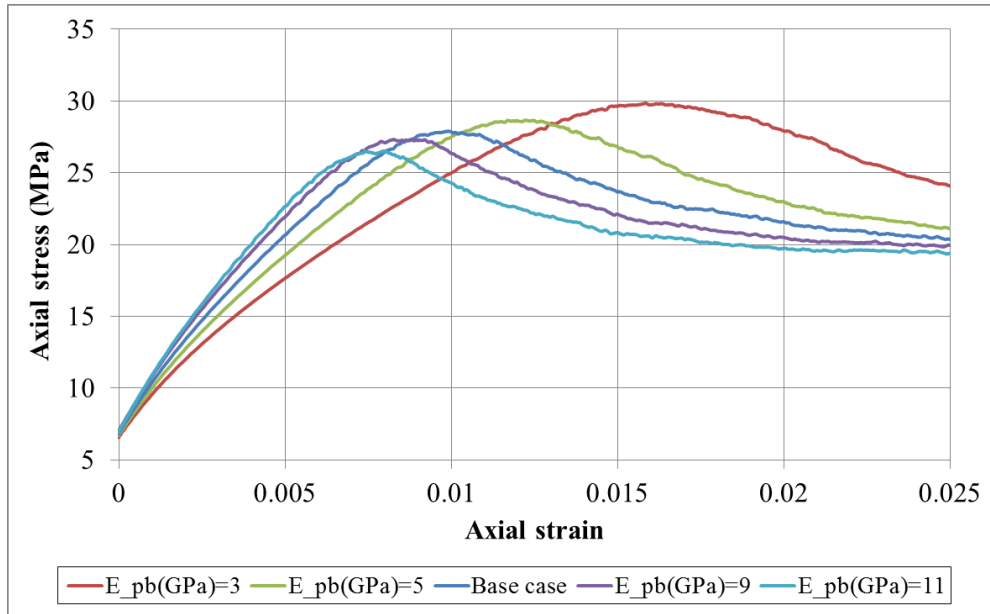


Figure 4.14 Sensitivity of the macro response to E_{pb}

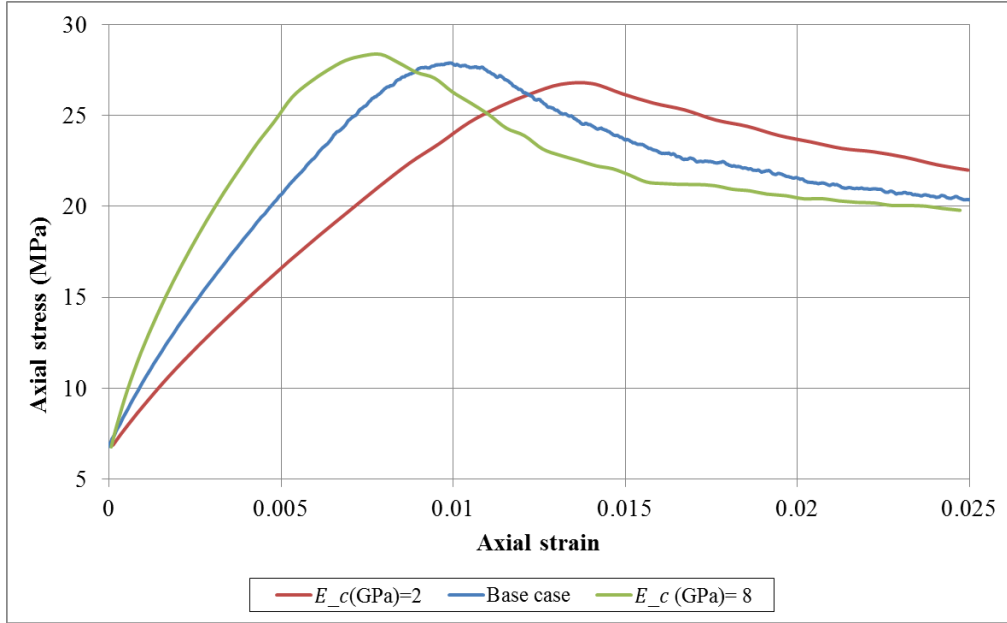


Figure 4.15 Sensitivity of the macro response to E_c

Figure 4.16 shows that the dilation angle increases with an increase in the parallel bond modulus (hence, increasing $\frac{E_{pb}}{E_c}$) and a decrease in the particle contact modulus (hence, increasing $\frac{E_{pb}}{E_c}$).

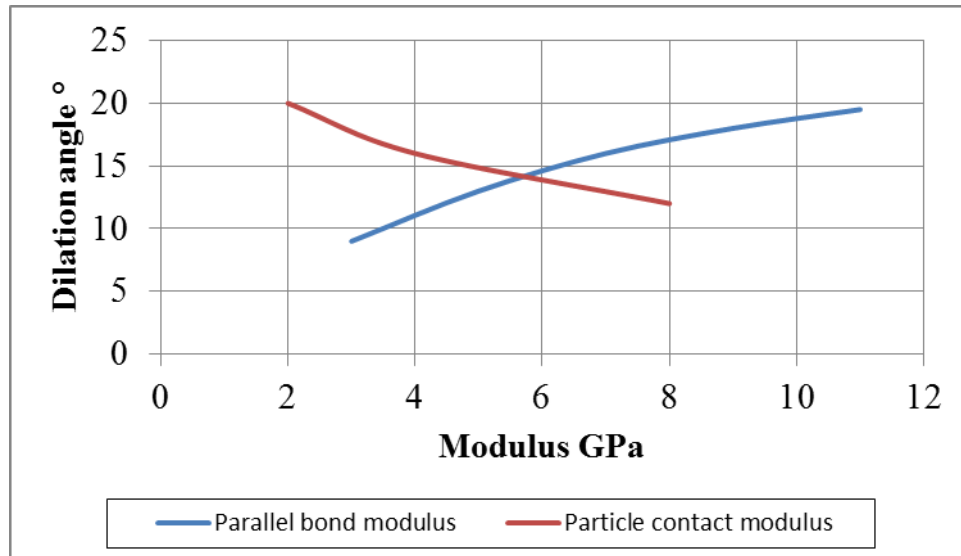


Figure 4.16 The impact of the particle contact and parallel bond moduli on dilation angle

4.6.2 Effect of percentage of bonded contacts (λ)

The effect of the percentage of bonded contacts (λ) was studied by choosing $\lambda = 10\%$, 30% , and 70% and investigating its impact on the material response. Figure 4.17 shows that an increase in λ (1) increased the macro Young's modulus; (2) increased the peak and residual strengths; and (3) resulted in a more distinct peak stress followed by sharper strain softening. For the simulation where $\lambda = 10\%$, no obvious peak strength was observed, and the behavior was similar to the response of loose sands in which the response is mainly governed by the frictional contacts. The macro Young's modulus of the specimen increases with increasing λ (i.e., adding more parallel bonds to the specimen). Also as λ increases, lower loads are attracted to each parallel bond at any axial load, boosting the peak strength.

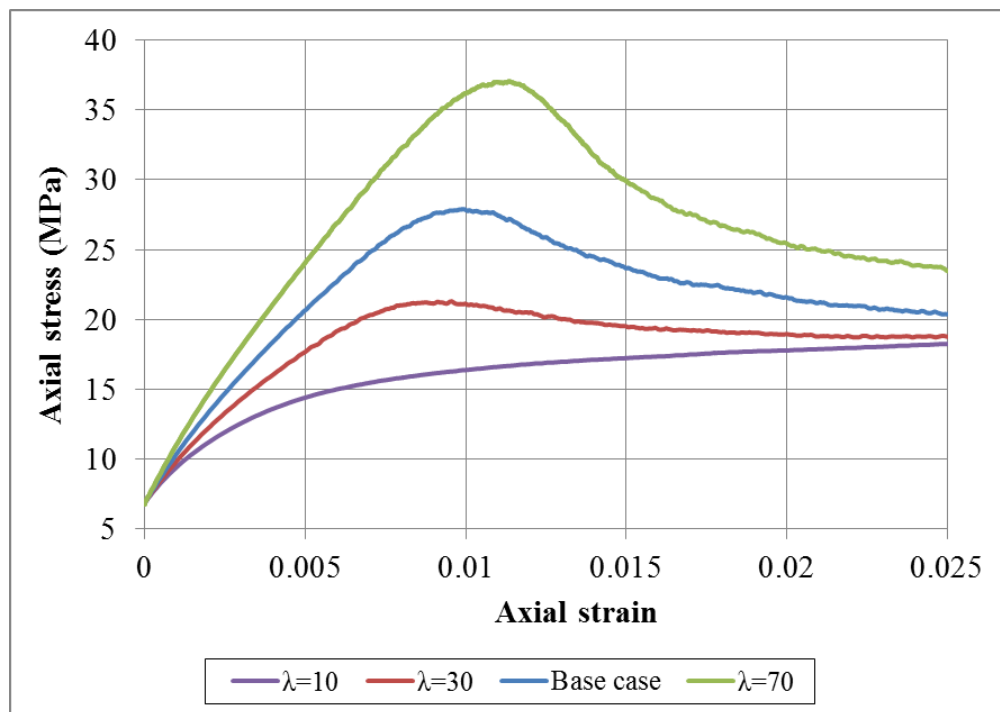


Figure 4.17 Sensitivity of response to the percentage of bonded contacts

Figure 4.18 also shows the impact of λ on the Poisson's ratio for the triaxial test at a confining pressure of 6.8 MPa. The Poisson's ratio decreases with increasing the percentage of bonded contacts. These general trends were also predicted by Schöpfer et al. (2009). In addition, Figure 4.19 shows that the dilation increases with increasing the percentage of bonded contacts.

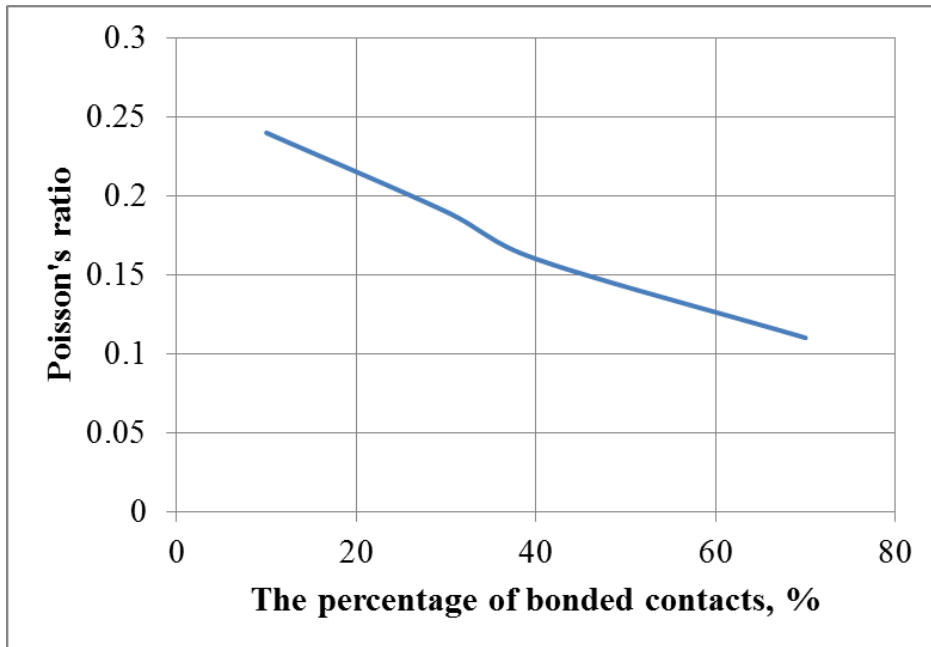


Figure 4.18 The impact of the percentage of bonded contacts on Poisson's ratio

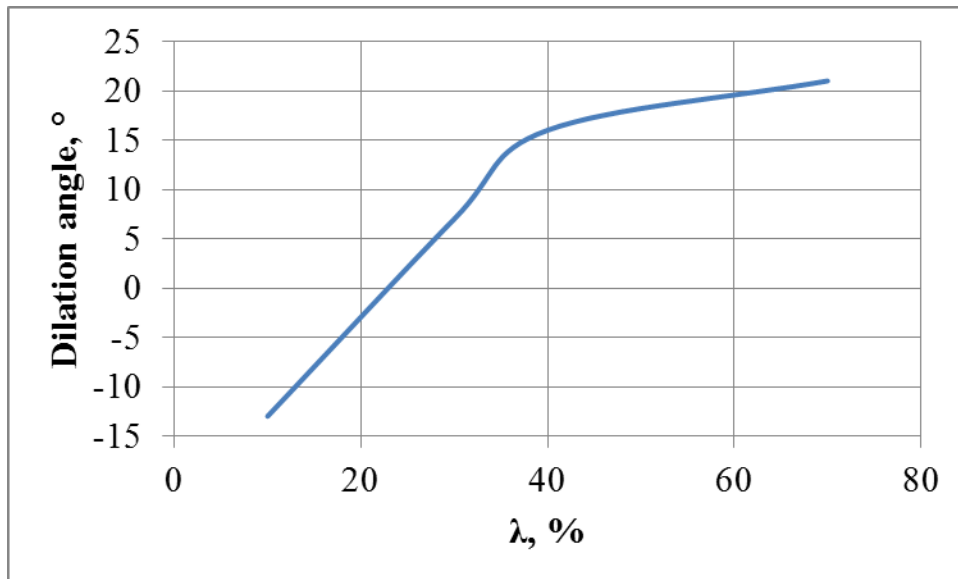


Figure 4.19 The impact of the percentage of bonded contacts on dilation angle

4.6.3 Effect of bond strengths

The effect of the parallel bond strength on the specimen response was also studied by varying S_{pb}^N and S_{pb}^S (Table 4.4).

Table 4.4 Simulation investigating the effect of bond strengths

Test	S_{pb}^N (MPa)	Test	S_{pb}^S (MPa)
8	30	10	60
Base case	60	Base case	96
9	96	11	120

The results are presented in Figure 4.20 and Figure 4.21. Figure 4.20a and Figure 4.21a show that the bond strengths have negligible effect on the elastic response. It is clear from Figure 4.20d and Figure 4.21d that only a small number of parallel bonds failed in the elastic range. The difference in the macro responses was observed once the parallel bonds began to break. The most important parameters affected by the bond strengths were the peak and residual strengths (Figure 4.20a and Figure 4.21a).

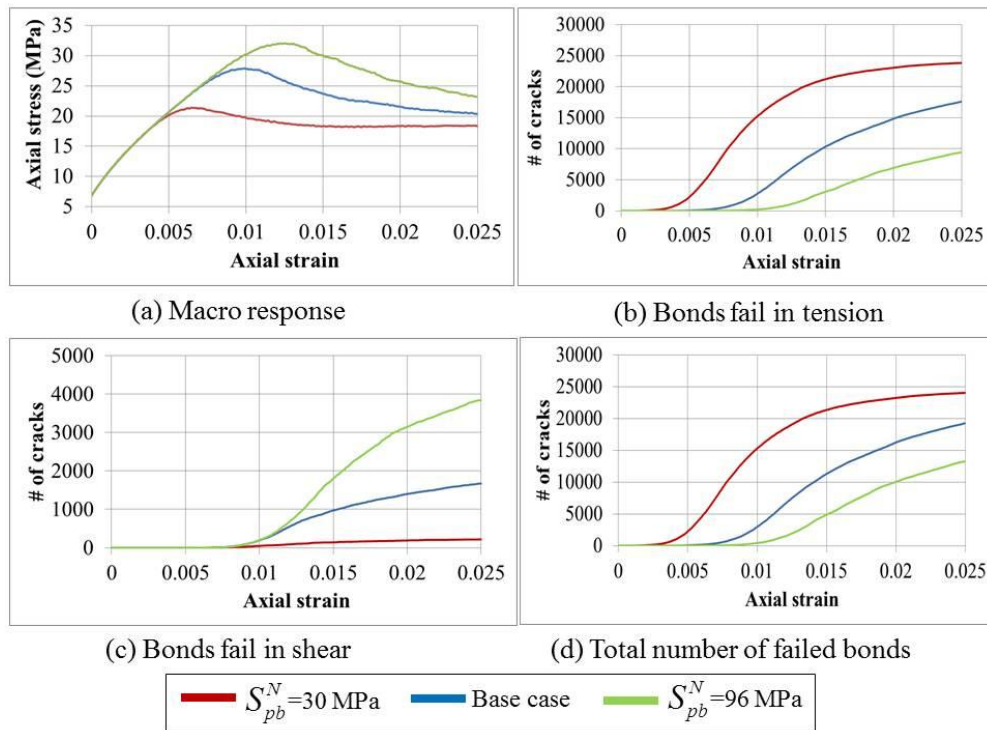


Figure 4.20 Sensitivity of response to normal bond strength

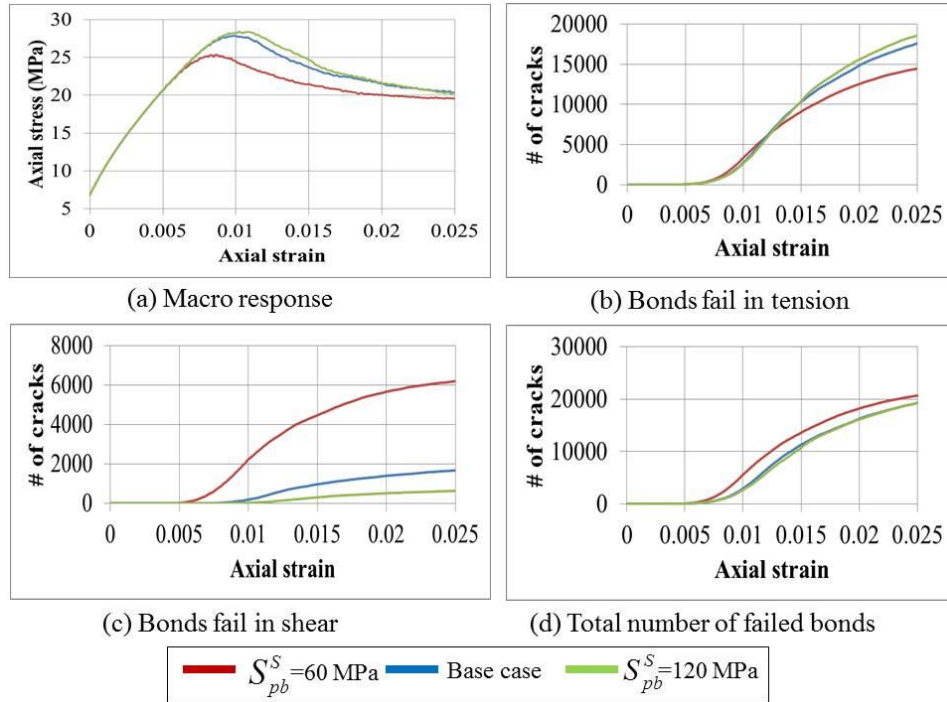


Figure 4.21 Sensitivity of response to shear bond strength

Figure 4.22 shows the macro response in terms of volumetric strain versus the axial strain. It indicates higher sample contraction for the cases with stronger bonds before the response turns dilative. Further, the rate of dilation was faster for the stronger bonds.

In general, the macro responses for this triaxial test were more sensitive to the normal bond strength than shear bond strength as seen in the number of bonds which failed in tension and shear (Figure 4.20b-c and Figure 4.21b-c). It was observed that more bonds failed in tension than in shear. The amount of confining pressure played an important role in the bond rupture. At low confining stress, the bonds mainly failed in tension, and at high confining stress, the bonds mainly failed in shear.

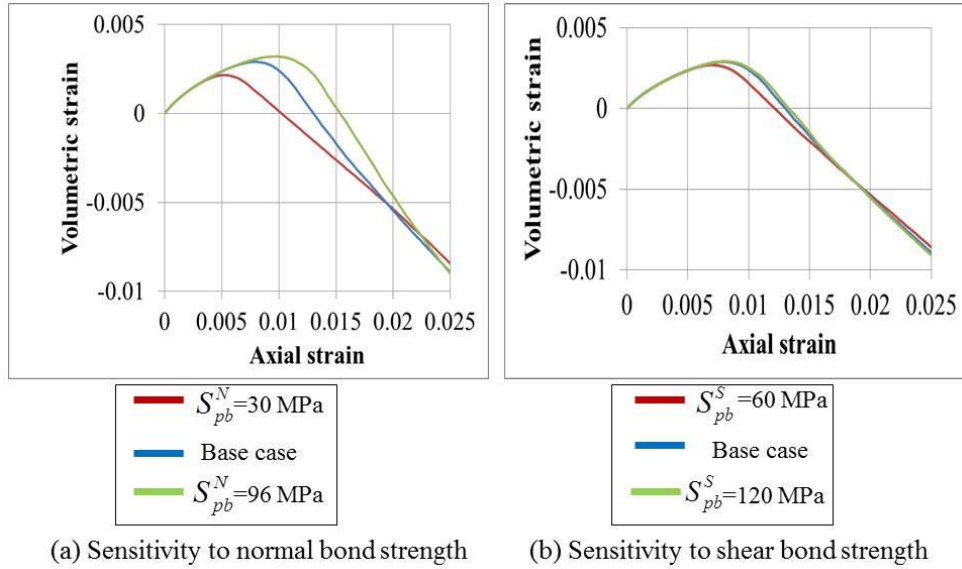
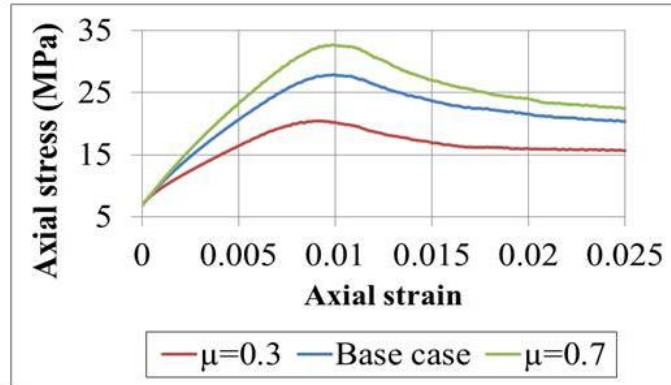


Figure 4.22 Sensitivity of volumetric strain to bond strengths

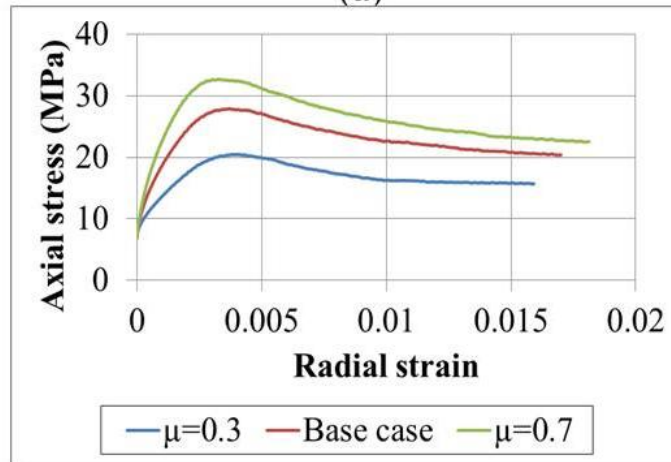
4.6.4 Effect of friction between particles (μ)

According to Cui (2006), with increasing inter-particle friction of an unbounded specimen, the peak stress of the specimen increases. The impact of inter-particle friction is expected to be different for a parallel-bonded specimen due to the effect of the parallel bonds on the response. It has been reported that the particle friction coefficient affects post-peak behavior (Itasca, 2008).

The impact of inter-particle friction was investigated by a parametric study. Figure 4.23a shows that the increase in inter-particle friction leads to higher initial stiffness, higher peak strength, and higher residual stress. The dilation angle at the peak strength also increased from 13° when $\mu=0.3$ to 18° when $\mu=0.7$.



(a)



(b)

Figure 4.23 Sensitivity of response to inter-particle friction

As inter-particle friction increases, the particles have less freedom to slide and roll over. Therefore, less lateral strain is possible leading to a lower Poisson's ratio (Figure 4.23b).

4.6.5 Effect of radius multiplier (α)

The effect of the parallel bond radius was studied by varying $\alpha = 0.2$ and 0.8 , and investigating its impact on the material response. Figure 4.24 shows that an increase in α (1) increased the macro Young's modulus; (2) increased the peak strength; and (3) resulted in a more distinct peak stress followed by sharper strain softening. For the simulation where $\alpha = 0.2$, no obvious peak strength was observed, and the behavior was similar to the response of loose sands in which the response is mainly governed by the frictional contacts. As α decreases, the parallel bond radius is reduced and the parallel bond experiences a reduction in stiffness. The Poisson's ratio also increased from 0.13 when $\alpha=0.8$ to 0.18 when $\alpha=0.2$.

Thus, the effect of decreasing the radius multiplier is similar to the effect of decreasing the percentage of bonded contacts between particles. However, the radius multiplier does not have a significant effect on the dilation angle.

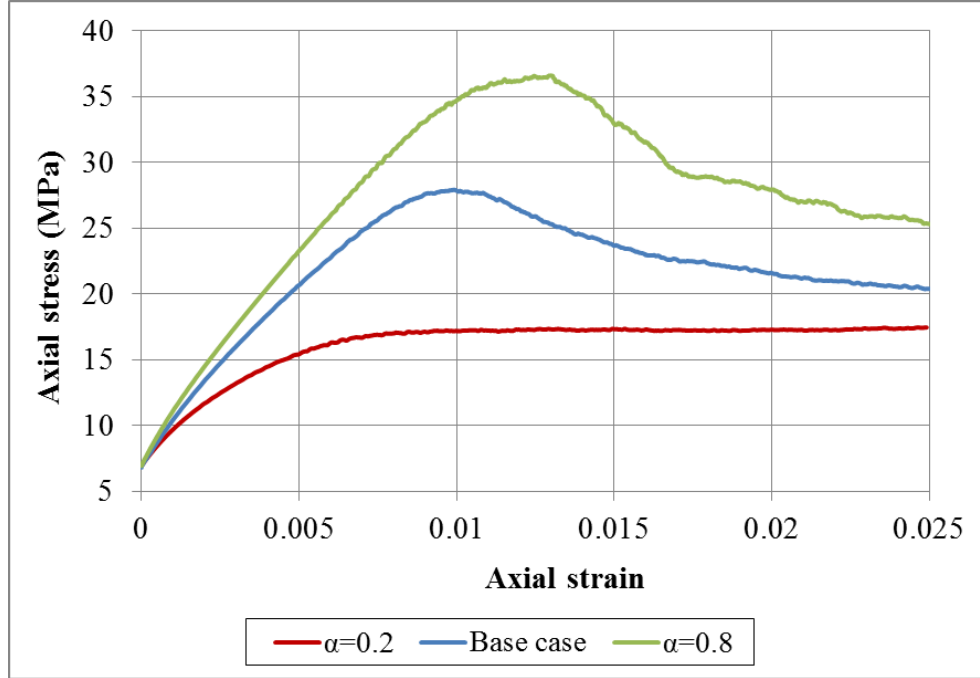


Figure 4.24 Sensitivity of response to radius multiplier (α)

Potyondy and Cundall (2004) showed that the macroscopic Poisson's ratio is affected by grain shape, grain packing, $\frac{K^N}{K^S}$, and $\frac{K_{pb}^N}{K_{pb}^S}$ in a bonded particle model. It seems that Poisson's ratio is also affected by the friction coefficient between particles, the percentage of bonded contacts, and radius multiplier.

4.6.6 Effect of $\frac{K^N}{K^S}$ and $\frac{K_{pb}^N}{K_{pb}^S}$

According to Yoon (2007), with increasing $\frac{K^N}{K^S}$ of an unbounded specimen, its Poisson's ratio increases.

The impact of the ratio of normal to shear stiffness of the particles and cement was investigated by choosing $\frac{K^N}{K^S} = \frac{K_{pb}^N}{K_{pb}^S} = 0.5$ and 1.5. Figure 4.25 shows that the increase in the ratio of normal to shear stiffness of the particles and cement leads

to a higher Poisson's ratio. The ratio of normal to shear stiffness of the particles and cement does not have significant effect on the macro Young's modulus, dilation angle, and the peak and residual strengths.

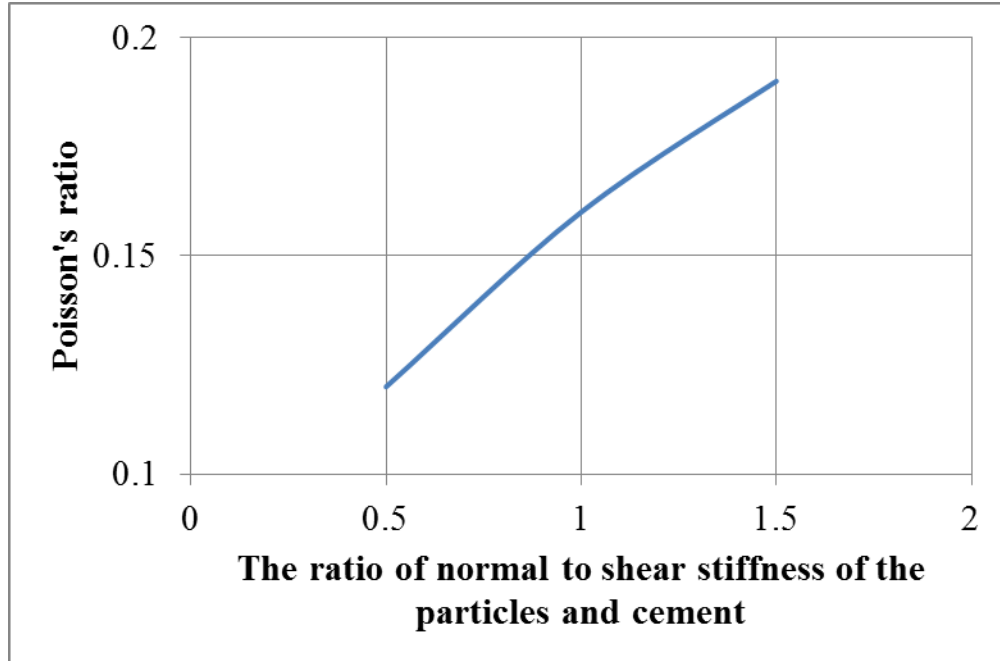


Figure 4.25 The impact of ratio of the normal to shear stiffness of the particles and cement on Poisson's ratio

4.7 Suggested procedure for calibration of micro-properties

Based on the knowledge gained from the parametric study, the following calibration sequence can be followed in order to minimize the number of iterations and to ensure the uniqueness of the calibration.

The calibration starts with the evaluation of the micro-parameters that affect the pre-peak response. Based on the parametric studies, the initial stiffness of the material is affected by the particle and bond Young's modulus, the inter-particle friction, the degree of bonding, and the radius multiplier. The steps below may be taken to calibrate the micro-properties.

1. The percentage of bonded contacts (λ) and the radius multiplier (α) to set the parallel bond radius could be determined using SEM images of thin sections through sandstone cores (Cheung, 2010).

2. The friction coefficient between the particles in the parallel bond model is initially assumed to be equal to the macro friction coefficient at the peak strength observed in the laboratory results.
3. The particle contact modulus is not a constant, and it increases with increasing confining stress, indicating the effect of particle overlap and reorientation at different confining stresses. The particle contact modulus at high confining stresses could be initially assumed to be equal to the Young's modulus of the minerals that the material is composed of.
4. Use the results of triaxial testing at high confining stresses and follow the procedure below:
 - a. Cement Young's modulus is calibrated to match the macro rock stiffness from the laboratory measurement and DEM simulations.
 - b. $\frac{K^N}{K^S}$ and $\frac{K_{pb}^N}{K_{pb}^S}$ affect Poisson's ratio. In order to minimize the number of iterations in the simulation, it is assumed that they are equal and are calibrated to match the Poisson's ratio calculated for the triaxial test.
5. The parallel bond strengths are adjusted to capture the peak mobilized stress ratio measured in the laboratory tests. To minimize the number of iterations for the parallel bond strengths, it should be noted that parallel bonds mainly fail in shear at high confining stresses and in tension at low confining stresses. Therefore, the shear bond and normal bond strengths are calibrated to match the peak mobilized stress ratio at high and low confining stresses, respectively.
6. Adjust the friction coefficient between particles and the particle contact modulus to match the residual stress and the dilation angle of the laboratory test with simulation results, respectively. The adjustment in the friction between particles and the particle contact modulus affects the macro elastic response.

7. Repeat steps four through six as needed to obtain a match between the laboratory data and the simulation results.

It is to be noted that all micro-parameters' calibrations are done using triaxial testing data at one single confining pressure. The triaxial testing data at other confining pressures are only to be used to calibrate the contact modulus parameter (E). However, the value of E was shown to only influence the macro Young's modulus and dilation angle. In addition, the UCS testing data are used to calibrate the bond normal strength. Therefore, most of triaxial data remain unused in the calibration process. A close match of numerical versus experimental values at different confining pressures is an indication of the success of the calibration procedure in assessing the correct values of the micro-parameters (Figure 4.5).

It is also worth noting that the above procedure is also applicable to micro-parameters evaluation of unconsolidated sands. In sands, there is no cementing material. Therefore, cement micro-parameters should simply be set at zero.

4.8 Conclusions

In this chapter, a calibration methodology for 3D DEM models using a bonded particle model was presented. The calibration procedure was based on a systematic trial-and-error method and comparison of laboratory and simulated triaxial tests. To minimize the number of iterations, the effect of micromechanical parameters was investigated on the macro responses of the simulated triaxial tests. The parametric studies showed that although the calibration was based on trial and error, different micro-parameters lead to different macromechanical responses. Identification of such trends allows an efficient calibration process with minimal trial and error.

DEM simulations were carried out to simulate SWS sandstone triaxial testing. In spite of its simplicity, the model reproduced the macro responses of SWS sandstone obtained from laboratory testing, such as the initial elastic response, the peak stress, and the post-peak behavior.

The calibration was validated against TWC measurements for SWS sandstone and also verified with the analytical solutions. The numerical results were quantitatively in agreement with the analytical and experimental results.

Chapter 5: Simulation of drilling induced compaction bands using Discrete Element Method

5.1 Introduction

Several attempts have been made to investigate the failure pattern around the borehole based on theoretical works, notably using elasto-plasticity (Detournay et al., 2009; Kwong and Kaiser, 1989; Papamichos et al., 2001; Zheng et al., 1989), pressure-dependent elasticity (Santarelli and Brown, 1987, 1989), bifurcation theory (Papanastaiou and Vardoulakis, 1992), fracture mechanics (Bazant et al., 1993; Germanovich and Dyskin, 2000) and microstatistics (Charlez et al., 1989). A comprehensive review of many theoretical and numerical approaches to investigate the mechanism of the borehole breakouts has been provided by Germanovich and Dyskin (2000).

Several researchers have identified the discrete element method as a useful tool in the investigation of breakout morphology and sand production (Jensen et al., 2000; Li et al., 2006; O'Connor et al., 1997; Rawlings et al., 1993). Instead of treating the rock mass as a continuum, DEM simulates the particles/blocks and their interaction explicitly (Jing and Stephansson, 2007).

Li et al. (2006) used PFC2D (Itasca, 2004) to simulate HC tests with fluid flow and study breakout geometry. In the standard PFC2D code, the bonds have normal and shear stiffness and strength and they fail when the tensile or shear stress in the bond exceeds its strength (Itasca, 2004). Li et al. (2006) used bond strength so high that no bonds in the model would fail due to the stress in the bond. They assumed that all bonds associated with a given disk break when the stresses inside the disk satisfy a failure criterion. In addition, they simulated grain crushing by reducing particle radius when the particle stresses reached a threshold. They found three typical breakout geometries in the simulations similar to those observed in laboratory tests. The fracture-like breakout was observed when the material was prone to localized compressive failure. However, the compacted zone of reduced porosity was not observed at the breakout tip. For those cases where the material was weak and the tensile strength was low,

uniform failure around the borehole was observed along with a rather uniform hole enlargement. In the cases with relatively competent rock properties, which were unlikely to fail in localized compaction, a V-shaped breakout failure pattern was observed.

Little is known on the mechanism of the initiation and propagation of the compaction bands at the grain scale during drilling. This chapter describes the development of drilling induced compaction bands using a 3D discrete element model to investigate the mechanism of the fracture-like breakout at the particle scale. It also focuses on the effect of stress anisotropy on the breakout type. In this work, a numerical scheme was implemented in PFC3D to simulate grain crushing during the formation of compaction bands that are believed to induce fracture-like breakouts. The numerical tool was verified against analytical solutions and was then utilized to study the effect of stresses on the breakout length and shape in cubic laboratory rock samples.

5.2 The grain crushing modeling scheme

In addition to the tensile and shear failure at inter-granular contacts that are captured in the standard PFC3D, the model used in this research includes a scheme to simulate grain breakage and crushing.

Several researchers have proposed a number of schemes to model grain breakage in DEM simulations (Cheng et al., 2003; Couroyer et al., 2000; Marketos and Bolton, 2009; Tsoungui et al., 1999). The schemes use some simplifying assumptions to capture the behavior without dramatically increasing simulation time.

The breakage criterion is usually defined in terms of contact forces acting on the grain (Couroyer et al., 2000; Marketos and Bolton, 2009). In this research, a particle will break if the characteristic stress (σ_{ch}) inside the particle exceeds its crushing strength (σ_{crush}) (Marketos and Bolton, 2009):

$$\sigma_{ch} = \frac{F_{(\max)particle}}{D^2} \geq \sigma_{crush} , \text{ grain breaks} \quad (5.1)$$

The characteristic stress (σ_{ch}) is defined as the ratio of the maximum normal contact force ($F_{(max)particle}$) on the particle to the square of its diameter (D). Thus, the effect of the spatial distribution of the contact forces around the grain is neglected. However, Marketos and Bolton (2009) concluded this effect is negligible where the coordination number of approximately two-thirds of the particles is either 6 or lower. In the current study, the coordination number of the particles is around 6 or lower. The crushing strength (σ_{crush}) has been experimentally evaluated by conducting single grain crushing tests. The test is conducted by inserting a grain between two platens and then moving the lower platen to crush the grain. The crushing strength is defined as the ratio of the maximum force at failure to the square of the distance between the platens at the start of the test (McDowell and Amon, 2000; Nakata et al., 2001). Nakata et al. (2001) concluded that the grain crushing strength depends on the grain mineralogy and the grain size. In addition, the crushing strength of the grains was determined by multiple particle crushing strength test method, where each particle was compressed between a platen and an assembly of stainless steel beads (Couroyer et al., 2000). The crushing strength is detected by a sudden drop in the load which applies to the platen.

In the DEM simulation of the compaction band, different methods were used to simulate the post breakage behavior. A comprehensive review of the methods is given by Marketos and Bolton (2009). One of the methods for modeling grain crushing is to reduce the contact stiffness of the crushed particle (Marketos and Bolton, 2009). The stiffness reduction simulates the deformation of inter-fragment voids, making the local response less stiff. The amount of stiffness reduction depends on the grain mineralogy and the stresses on the crushed particle by the neighbouring grains. After breakage, the broken particle could still carry force resulting in reduction in the compaction band porosity. Kurt et al. (2005) found that the elastic modulus within the compaction band increases as the result of porosity reduction and the increased area of contact among the grains.

5.3 The numerical modeling case

The numerical model has been used to simulate the balanced drilling process in Castlegate sandstone at the laboratory scale. In balanced drilling, the drilling fluid pressure is equal to the formation pore pressure and there is no fluid flow in the formation.

In the numerical analysis, the effective far-field stresses were applied to the sample with zero pore pressure instead of applying the total far-field stresses along with the pore pressures. The numerical procedure was designed to closely simulate the drilling conditions in which the wellbore material is removed while the rock is under the *in situ* stresses. The applied stresses were sufficiently high to generate breakouts around the hole.

In real-world drilling, the drilling mud is usually circulated through the borehole during drilling in order to cool the drilling bit and transport the rock debris to the surface. The drilling mud is usually cooler than the formation rock inducing thermal stresses in the rock. However, the thermal effect was not included in the numerical analyses.

Test numerical specimens were generated in a rectangular box of $0.18 \text{ m} \times 0.18 \text{ m} \times 0.02 \text{ m}$ ($W \times H \times D$) bounded by rigid frictionless walls. The model creation procedure was similar to the same described in Section 4.2.1. Parallel bonds were randomly installed at 30% of the contacts detected at this stage, and the bond radius multiplier was varied randomly between 0 and 1 based on the observations from the SEM images for the Castlegate sandstone, which is discussed in Appendix B. Then a friction coefficient was assigned to all particles.

The specimen consisted of 89,538 spherical particles of sizes randomly between 0.4 and 1.3 mm, which approximately captures the particle size distribution of the Castlegate sandstone (Figure 5.1).

Other DEM micro-parameters were calibrated using the algorithm described in Section 4.7 for the Castlegate sandstone (Table 5.1). Appendix B describes in detail the calibration process for the Castlegate sandstone.

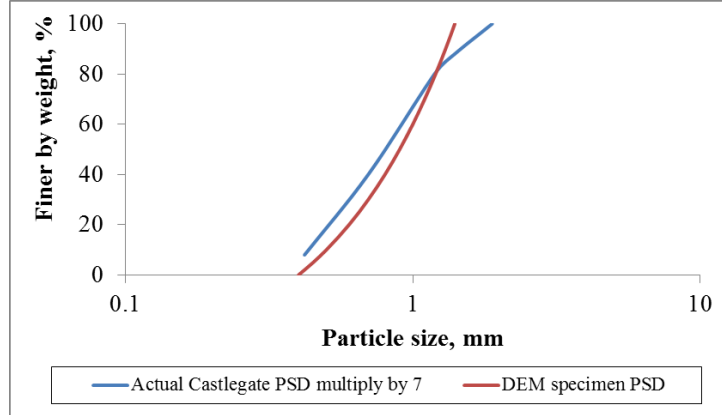


Figure 5.1 Comparison between the actual Castlegate PSD and the DEM specimen PSD

Table 5.1 Calibrated micro-parameters for the Castlegate sandstone DEM model

Particle properties		Parallel bond properties	
Particle contact modulus, E_c (GPa)	7	Cement Young's modulus, E_{pb} (GPa)	20
The ratio of normal to shear stiffness of the particles, $\frac{K^N}{K^S}$	0.2	The ratio of normal to shear stiffness of the cement, $\frac{K_{pb}^N}{K_{pb}^S}$	0.2
The particle friction coefficient, μ	1.5	Normal strength of the cement, S_{pb}^N (MPa)	400
Particle radius (mm)	0.4 to 1.3	Shear strength of the cement, S_{pb}^S (MPa)	900
Particle density, ρ_s (kg/m ³)	2650	The percentage of bonded contacts, λ (%)	30
		The radius multiplier, α	Randomly distributed between 0 and 1

The average porosity of the DEM specimen was assessed to be 0.34, which is higher than the actual porosity (0.25). This is partly because the parallel bond representing the cement between grains is represented as a set of springs with no volume. Cheung (2010) reported that the cement content for the Castlegate sandstone is equal to 6.4% by mass. By assuming the same density for the cement and grains, it can be concluded that approximately 0.06 of the porosity difference between the actual rock and the DEM specimen is due to the parallel bonds with no volume. Moreover, the particles in PFC3D are spherical, whereas in the Castlegate sandstone, grains are sub-angular and usually have irregular shapes (Cheung, 2010). This could also affect the packing and therefore the initial porosity of the specimen.

In our simulations, the stiffness of a crushed particle is reduced by a factor of two once the grain-crushing criterion is satisfied (Marketos and Bolton, 2009). Alvarado (2007) reported that the Castlegate sandstone particles are predominately quartzitic. The average particle crushing strength was assumed to be 60 MPa based on the single grain crushing experiments that Nakata et al. (2001) conducted on different sizes of quartzitic grains. In addition, it was assumed that the contact stiffness after grain crushing increases linearly as a function of porosity to eventually reach the original contact stiffness.

The simulation procedure began by applying three perpendicular and unequal stresses ($\sigma_H \geq \sigma_v \geq \sigma_h$) using a servo control algorithm. While maintaining the far-field stresses on the specimen, a vertical borehole (1.25 cm radius) was drilled by gradually decreasing the grains stiffness inside the borehole to zero and finally removing the grains from inside the hole. Then the model was cycled until the average unbalanced forces were low compared to the average contact forces (0.01 ratio was adopted here).

5.3.1 Verification of the DEM model

The DEM simulations were verified by comparing their response with the calculated results from analytical solutions. Zoback (2007) derived analytical

expressions for the effective stresses at the wellbore wall in an anisotropic elastic medium (Appendix A).

In the analytical solution and DEM model, the maximum horizontal, vertical, and minimum horizontal stresses were 40, 30, and 20 MPa, respectively. The applied stresses were selected such that the material response at the borehole wall was elastic. The sample was also assumed to be dry. Figure 5.2 compares the stresses in a cylindrical coordinate system at the wellbore wall of the DEM model with the analytical solution in terms of the angle with respect to the direction of the maximum horizontal stress. It shows that the radial stress is zero at the wellbore wall, and the tangential and vertical stresses vary as a function of position around the wellbore. It also shows that tangential stresses are higher in the direction of the minimum horizontal stresses. Note that the average value of vertical stress is the same as the far-field vertical stress (30 MPa), and the variation of the tangential stress is around four times the difference between the maximum and minimum horizontal stresses ($4 \times (40 - 20) = 80$ MPa).

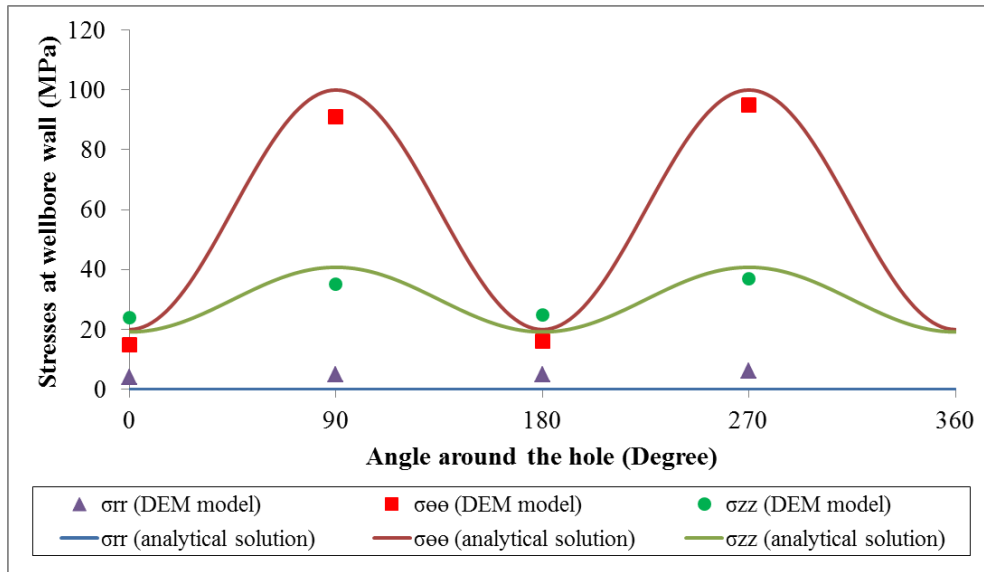


Figure 5.2 Comparison of the stresses at the wellbore wall between the DEM model and the analytical solution developed by Zoback (2007)

In addition, the DEM simulations were verified by comparing the DEM response with the calculated results from analytical solutions developed by Risnes et al. (1982). They derived analytical expressions for the stresses around a wellbore or

cavity using continuum-based elasticity and plasticity theories (Appendix A). They assumed axisymmetry and plane strain conditions and that the material obeys the MC failure criterion.

In the analytical model, a disk of Castlegate sandstone with an inner radius (R_i) of 8 mm, outer radius of 80 mm, and unit height was chosen. The sample was also assumed to be dry. The other input parameters for the analytical solution, including cohesion, friction angle, and Poisson's ratio, were assumed to be equal to 4.3 MPa, 46.5° , and 0.2, respectively. The cohesion and friction angle were evaluated at the peak strength from the simulated triaxial tests on the Castlegate sandstone assuming the material obeys the MC model. Elastic properties were also determined from the simulated triaxial tests. Young's modulus was determined at 50% of the peak stress (Jafarpour et al., 2012). The average Poisson's ratio at different effective confining stresses was also used in the calculations.

Figure 5.3 shows the analytical vertical and tangential stress profiles. The extent of the plastic zone is denoted by R_c , where the peak tangential stress is observed.

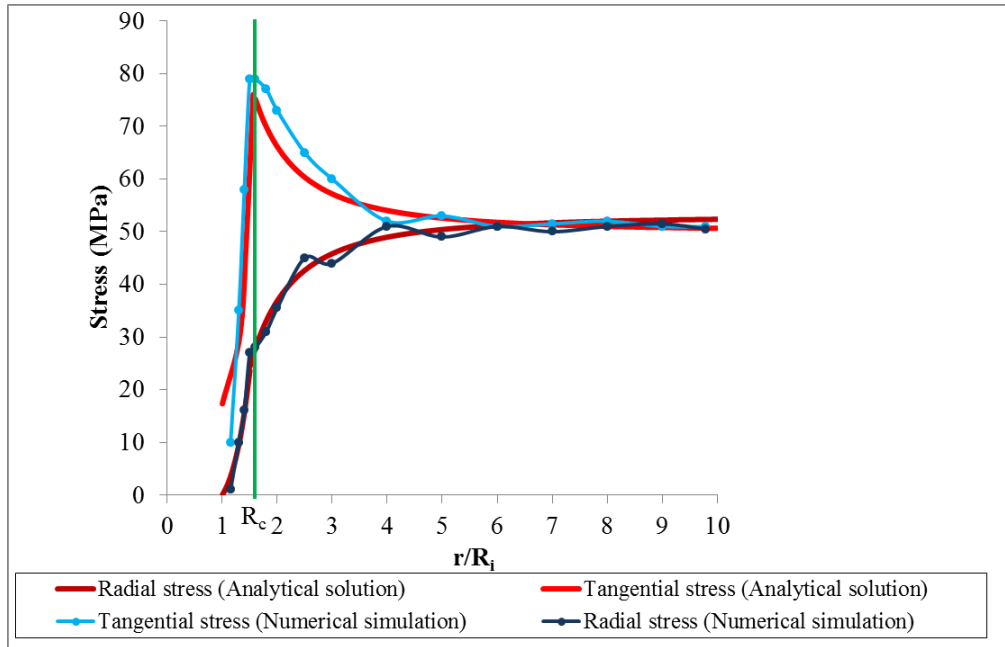


Figure 5.3 Comparison of the stresses around the wellbore between the DEM model and the analytical solutions developed by Risnes et al. (1982)

The DEM model was generated by three rigid walls (two horizontal and one cylindrical) with a radius of 80 mm and height of 15 mm. The micro-parameters were the same as the parameters in the calibration for Castlegate sandstone. A radial stress of 50 MPa was applied to the cylindrical wall using a servo control algorithm while the top and the base platen remained stationary. Then the inner hole was drilled by removing the particles, and the model was cycled until the average unbalanced forces were low compared to the average contact forces (0.01 ratio was adopted here).

Figure 5.3 compares the stresses around the wellbore of the DEM model with the analytical solution. The stress in the DEM model was calculated by performing a statistical averaging technique over a representative volume based on the algorithm described in Potyondy and Cundall (2004). The radial stress gradually increased from zero at the well face to 50 MPa at the outer boundary, and the tangential stress increased and reached a maximum value in the plastic zone and then decreased in the elastic zone. The stress values and the size of the plastic zone are in agreement with the analytical solutions.

5.4 Numerical results

The results of the simulations are presented in Figure 5.4 and Figure 5.5. Figure 5.4 shows a horizontal cross section of the sample after the completion of drilling. Micro-scale damage at the contacts is presented by red lines for bonds failed in tension and blue lines for the bonds failed in shear. The yellow grains show intact grains, while the black ones represent the crushed grains. Figure 5.4 shows the induced breakout is aligned with the minimum horizontal stress direction where the stress concentration is the highest. This breakout resembles the fracture-like breakout observed in Castlegate sandstone (Cundall et al., 1999) and highly porous sandstones (Haimson, 2007) in laboratory drilling experiments. Figure 5.4 indicates that a signature of the fracture-like breakout is the grain crushing inside the band.

Figure 5.5 shows the density of the bond breakage along the fracture-like breakout. Broken bonds density is defined as the total number of broken bonds

(which fail in either tension or shear) within the unit length of the compaction band in the entire height of the specimen. The figure indicates higher bond breakage densities near the hole face but significant bond breakage even farther inside the breakout band. The breakout is seen to initiate at the borehole wall by grain debonding and progressed with additional grain debonding, grain crushing, and grain repacking resulting in the formation of a band in the σ_h direction. Not every grain inside the band is crushed. The higher broken bonds near the wellbore face could facilitate particle removal by seepage or mudflow forces.

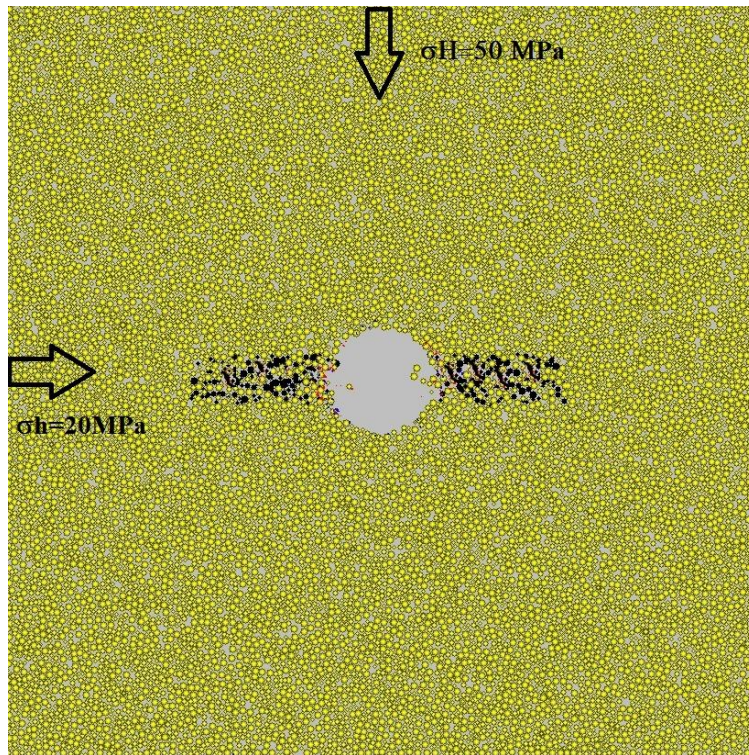


Figure 5.4 Borehole cross section of Castlegate sandstone showing a fracture-like breakout ($\sigma_v=30 \text{ MPa}$)

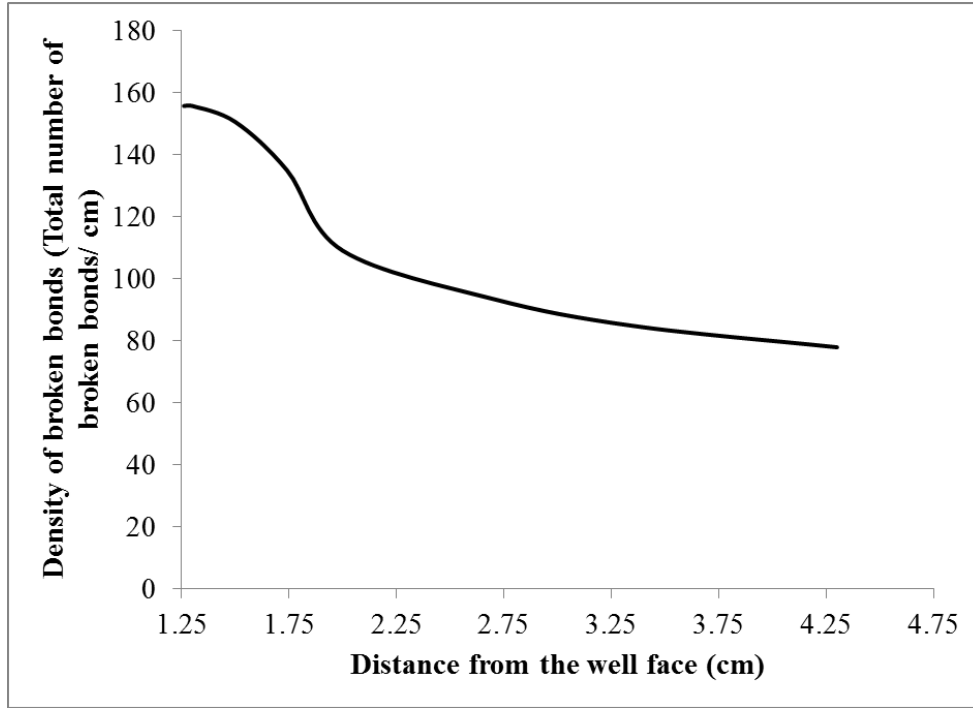


Figure 5.5 Density of broken bonds within the compaction band ($\sigma_h=20$ MPa, $\sigma_v=30$ MPa, $\sigma_H=50$ MPa)

By the time the breakout is fully developed, the total number of broken bonds is only 310, while 1,484 particles are crushed inside the compaction band. The average porosity along the compaction band after drilling is 0.325, which is less than the initial porosity (0.34). Thus, it shows that the failure mechanism is not of a dilatant nature as in V-shaped breakouts (Haimson, 2007). In fact, grain crushing and grain debonding and repacking (alone or in combination) are the signatures of localized pore collapse, which is also known as compaction band. The length of the reduced porosity zone from the borehole center (L) was 4.3 cm.

Further evidence on the failure mechanism in the breakout can be obtained by examining the stress state in the breakout in relation to the MC envelope. The MC failure criterion for Castlegate sandstone is illustrated in Figure 5.6. The stress state inside the breakout (3 cm far from the borehole center) is also plotted in Figure 5.6 (Point “A”). It shows the stress state inside the band is well below the MC shear envelope, which confirms the failure mechanism is not shear. The

compactive mode of failure is usually represented by a cap in the MC failure criterion (Detournay, 2009; Li et al., 2006).

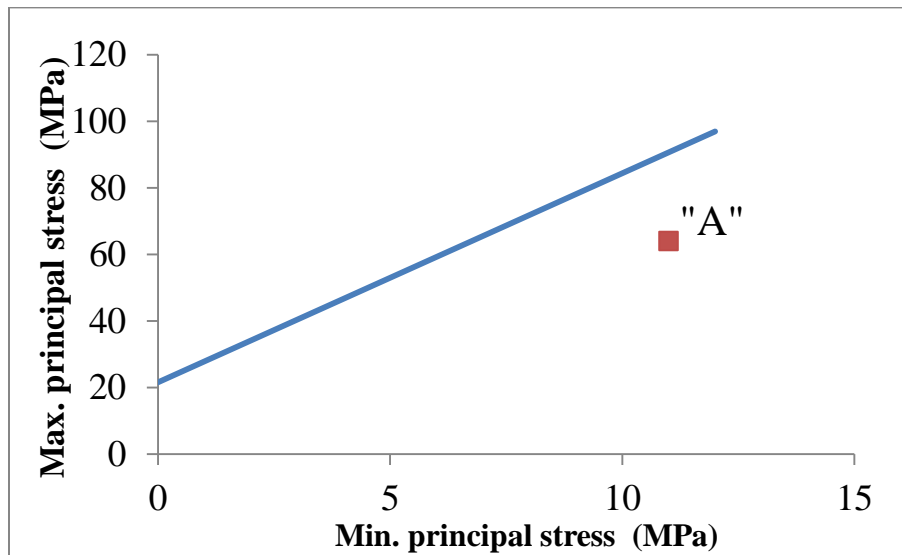


Figure 5.6 The MC failure criterion for Castlegate sandstone and the state of stress inside the breakout

Haimson and Lee (2004) experimentally showed that fracture-like breakout dimensions in Mansfield sandstone depend on the far-field stresses. In this research, the effect of far-field stresses on breakout dimensions was examined using the DEM on Castlegate sandstone. The simulations were conducted at different levels of the minimum and maximum horizontal stress (σ_h and σ_H) and vertical stress (σ_v). The results show fracture-like breakouts in the σ_h direction for all these cases (Figure 5.7).

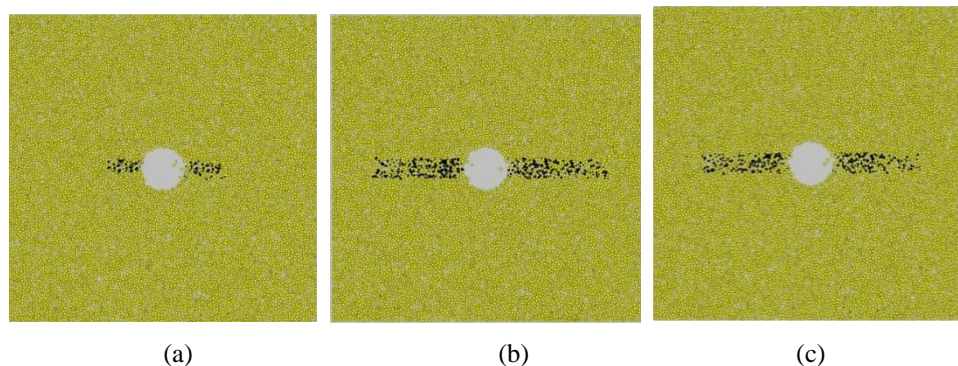


Figure 5.7 Borehole cross section of Castlegate sandstone at different far-field stresses (a) $\sigma_h=20$ MPa, $\sigma_v=30$ MPa, $\sigma_H=45$ MPa (b) $\sigma_h=20$ MPa, $\sigma_v=30$ MPa, $\sigma_H=60$ MPa (c) $\sigma_h=30$ MPa, $\sigma_v=35$ MPa, $\sigma_H=50$ MPa

Figure 5.8 shows the breakout length (normalized using the hole radius) as a function of the ratio between the maximum and minimum horizontal stresses (σ_H/σ_h). It shows that the slit length increases with increasing σ_H at constant σ_h (increasing σ_H/σ_h), which is in agreement with Haimson and Lee (2004). However, the length decreases at constant (σ_H) with decreasing σ_h (increasing σ_H/σ_h), which results in lower mean stress (e.g., comparing points A and B in Figure 5.8). This suggests that both mean stress and stress anisotropy can affect the length of the fracture-like breakout. This phenomenon could be explained by the failure mechanism of the fracture-like breakout.

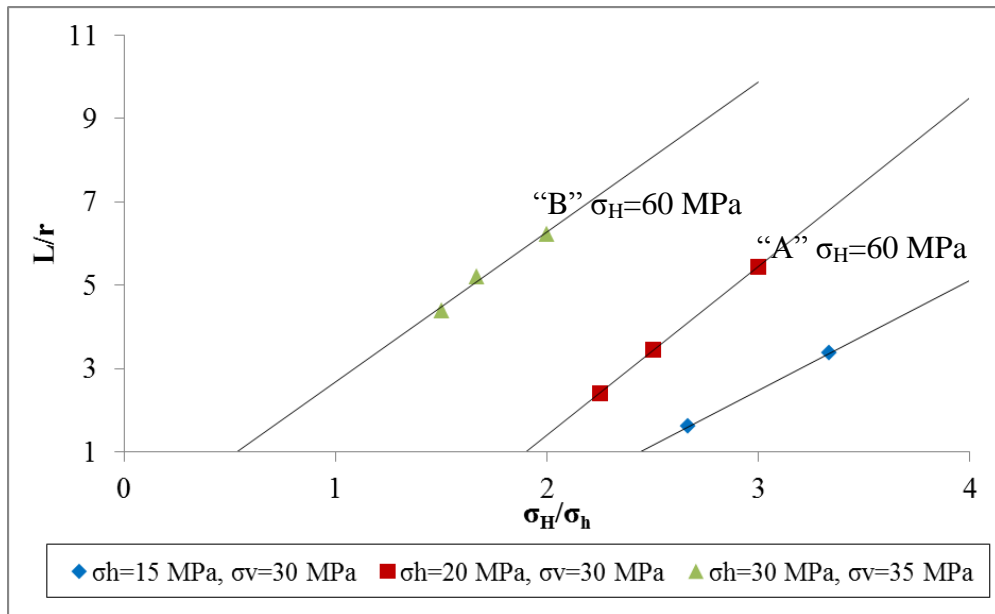
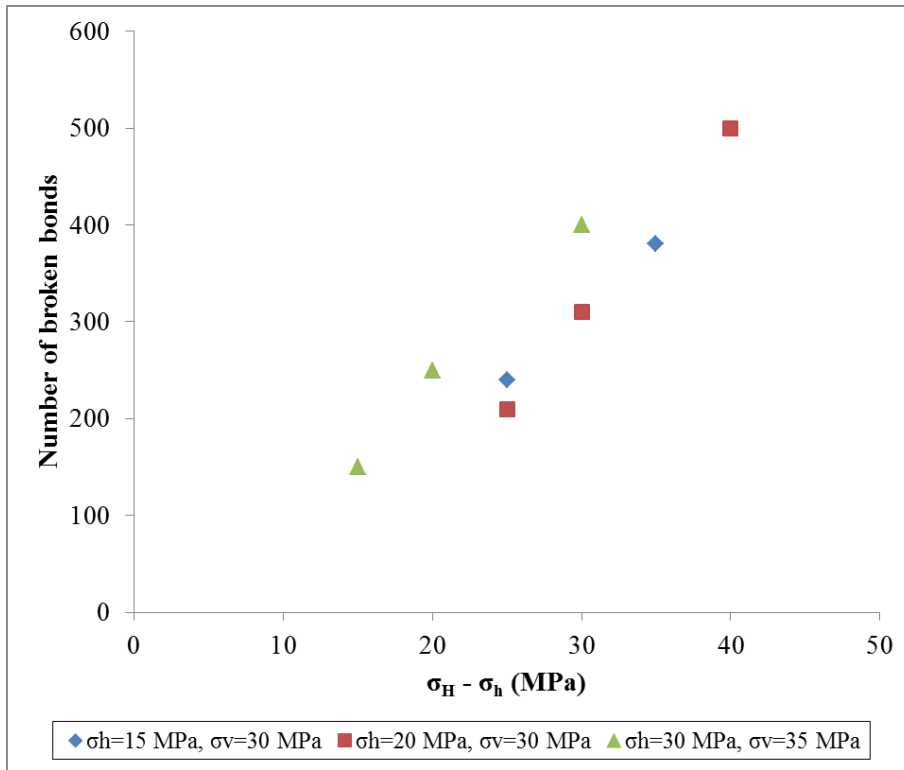
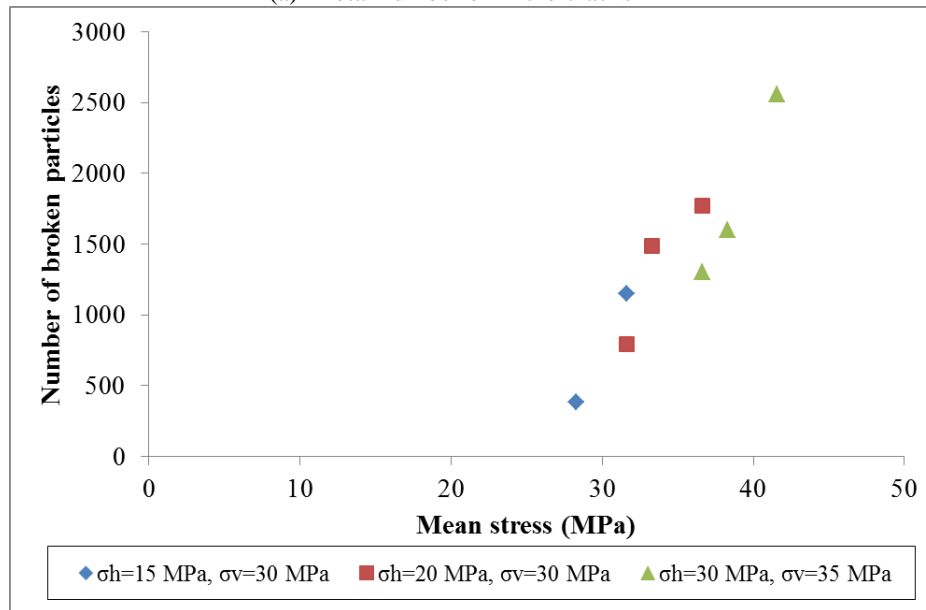


Figure 5.8 Variation of normalized breakout length (L/r) in Castelgate sandstone as a function of σ_H/σ_h

As mentioned above, a source of the formation and development of compaction bands is grain crushing and grain repacking. Figure 5.9a illustrates that more bonds break with increasing the stress anisotropy ($\sigma_H-\sigma_h$), and Figure 5.9b shows that more grains crush with increasing the mean stress. Figure 5.10 also shows that total number of broken bonds and broken particles do not change significantly with the change in the mean stress and stress anisotropy, respectively. Thus, it appears higher σ_H/σ_h ratio furthers grain debonding and grain repacking, whereas higher mean stress intensifies grain crushing.

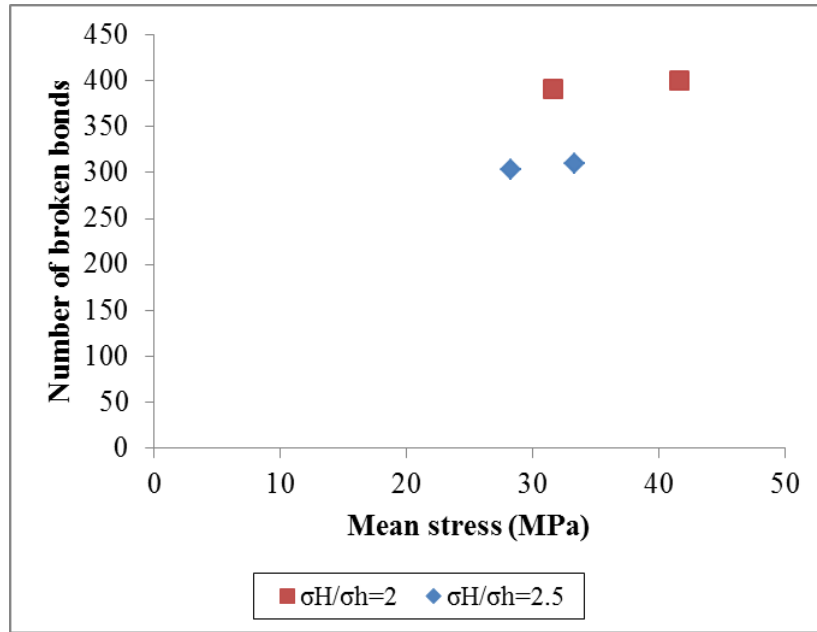


(a) Total number of micro cracks

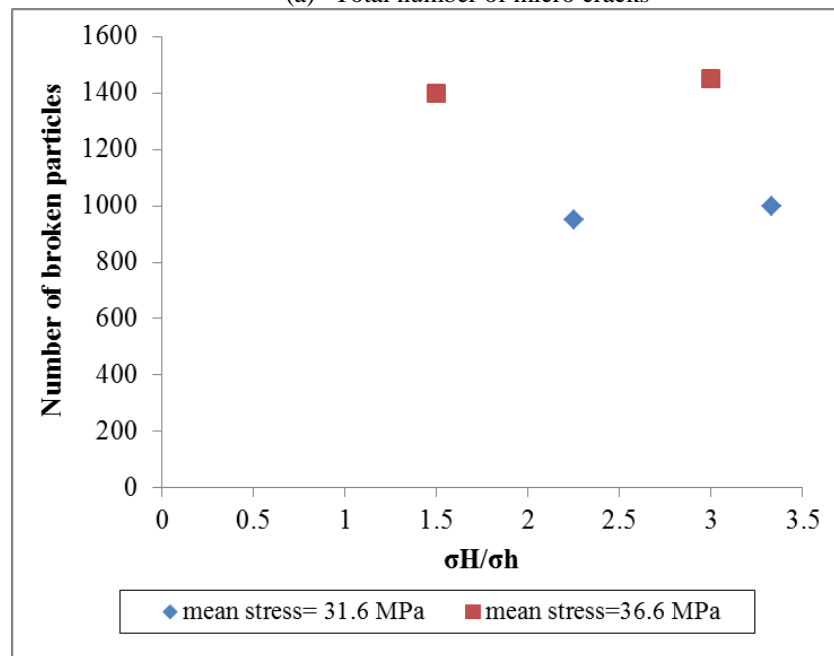


(b) Total number of broken particles

Figure 5.9 Variation of micro cracks and crushed grains as function of mean stress and stress anisotropy



(a) Total number of micro cracks



(b) Total number of broken particles

Figure 5.10 Variation of micro cracks and crushed grains as function of stress anisotropy and mean stress

The average width of the fracture-like breakout was measured at different far-field stresses (Figure 5.7). It is found that the average width remained almost constant ($7 \text{ mm} \pm 2 \text{ mm}$) regardless of the magnitudes of the far-field stresses. Haimson and Kovacich (2003) experimentally showed similar behavior in fracture-like breakout in Berea sandstone.

The stress analysis suggests that fracture-like breakout length could potentially be utilized as a stress magnitude indicator. One of the *in situ* stresses could be estimated from fracture-like breakout length only if the other two principal stresses are determined by other means (e.g, vertical stress from density logs and the minimum horizontal stress from minifrac tests).

5.5 Borehole breakout at isotropic stress conditions

Cerasi et al. (2005) experimentally showed that V-shaped and fracture-like breakouts could develop in HC tests on sandstone under isotropic stress conditions. It is hard to visualize these types of breakouts, which are angularly asymmetric, under uniform stresses. They concluded that development of these types of breakouts under hydrostatic loading conditions is due to either rock anisotropy or heterogeneity or both. Based on numerical simulations, Lavrov et al. (2005) showed that V-shaped breakout nucleation arises from the strength heterogeneity near the wellbore. They also concluded that the fracture-like breakout could propagate from the tip of a pre-existing slit.

In this research, the failure pattern under isotropic stress condition was investigated using the DEM model. In the simulations, the specimens were loaded hydrostatically ($\sigma_h = \sigma_H = \sigma_v = 33.3$ MPa). The applied stresses were high enough to induce breakouts around the wellbore. Simulations were performed with and without pre-existing flaws incorporated in the specimens by removing a few particles around the borehole.

The borehole breakout simulations under the isotropic stress condition were initially performed using the Castlegate sandstone properties reflected in Table 5.1. The result still shows fracture-like breakout in the direction at which the flaws had been created (Figure 5.11). This result is consistent with the observations in the TWC test for Castlegate sandstone (Cundall et al., 1999). By the time the breakout was fully developed, 1,027 particles had been crushed inside the compaction band creating a 3.6 cm slit length from the borehole center. This shows that fracture-like breakout can develop even under hydrostatic loading conditions due to the material heterogeneity. However, anisotropic far-field stress

conditions could facilitate the formation of compacted zone and could increase the length of the zone.

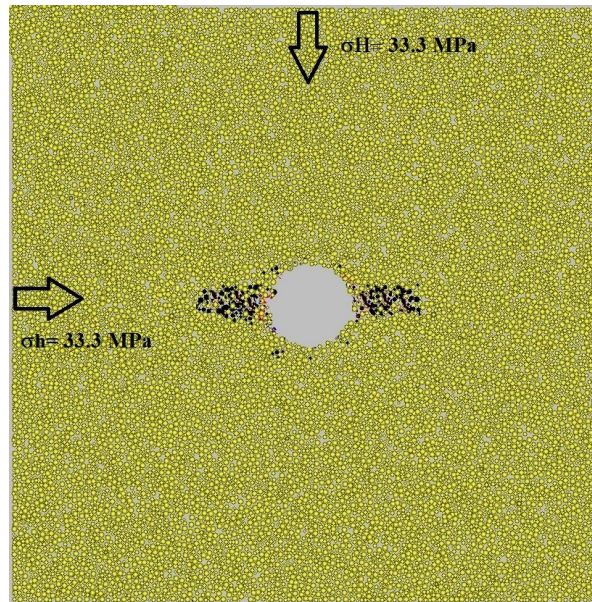


Figure 5.11 Borehole cross section of Castlegate sandstone with pre-existing cracks under isotropic stress conditions

Figure 5.12 shows the breakout geometry around the borehole under the same conditions as above, but without the flaw around the borehole. It shows the development of compacted zones in two perpendicular directions.

The development of the V-shaped breakout under the hydrostatic loading condition was also examined using a set of sandstone micro-properties that had resulted in a V-shaped breakout under anisotropic stress conditions (Figure 5.13). The micro-properties are the same as the ones for the Castlegate sandstone except for the normal and shear bond strengths, which were selected to be 200 and 450 MPa, respectively.

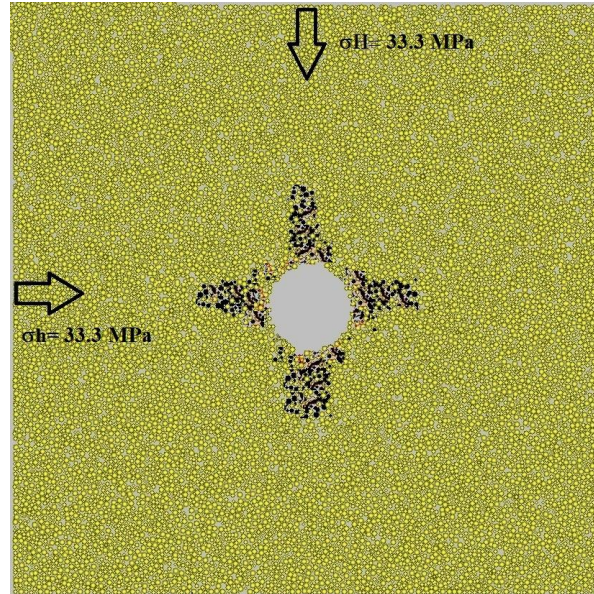


Figure 5.12 Borehole cross section of Castlegate sandstone without the flaw under isotropic stress conditions

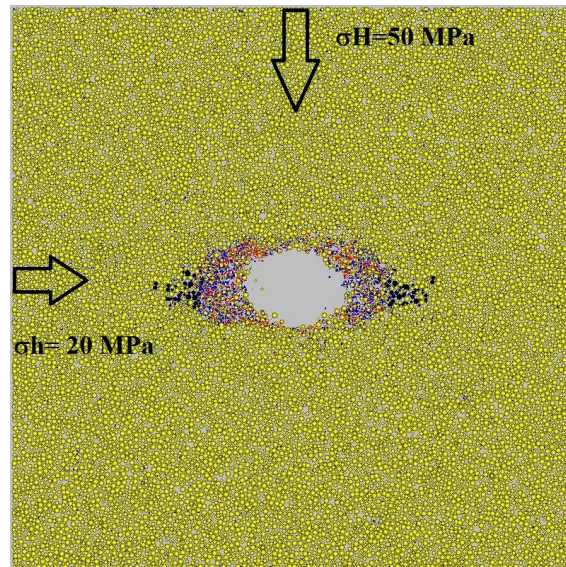


Figure 5.13 Borehole cross section under anisotropic stress conditions showing a V-shaped breakout ($\sigma_v=30$ MPa)

Repeating the above analysis under isotropic stress conditions still shows a V-shaped breakout when pre-existing flaws were created around the hole (Figure 5.14). The breakout developed in the directions at which the flaws had been created. The total number of broken bonds amounted to 6,320, and 110 particles were crushed at the tip of the breakout. The failure mechanism was also

dilatant, and the average porosity in the failed zone was around 0.42. Therefore, the result shows that V-Shaped breakouts can also form under hydrostatic loading conditions due to the heterogeneity in the specimen.

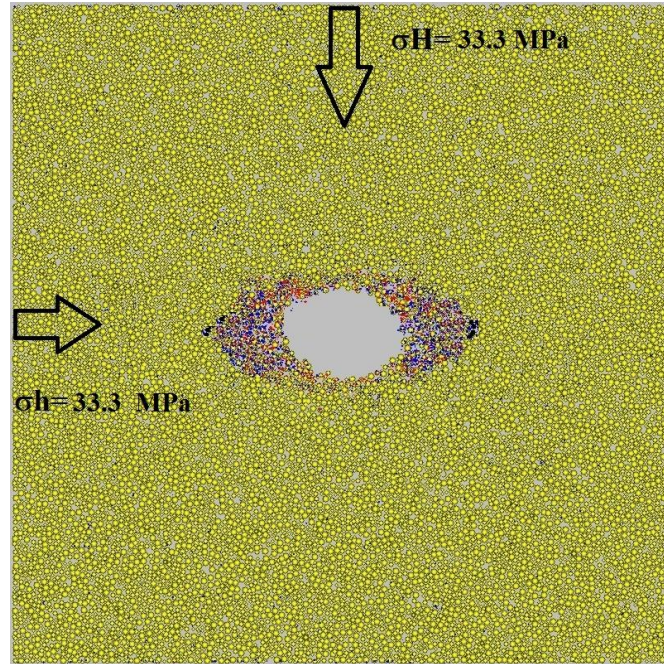


Figure 5.14 Borehole cross section under isotropic stress conditions showing a V-shaped breakout

Figure 5.15 shows the failure pattern for the same case as above, but without inducing the flaws at the borehole face. It shows two V-shaped breakouts were formed in two perpendicular directions. This shows that, even without the flaws, the breakout geometry is not angularly symmetric despite isotropic stress conditions.

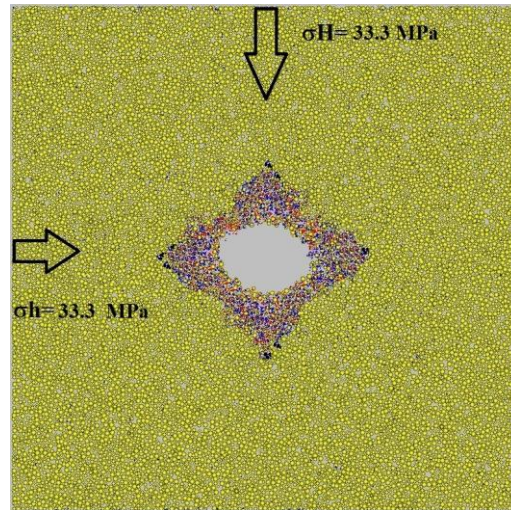


Figure 5.15 Borehole cross section without pre-existing flaws under isotropic stress conditions

5.6 Conclusions

A 3D numerical model has been developed to investigate drilling induced fracture-like breakout around wellbores. The model is based on discrete element method and improved by implementing a grain-crushing algorithm to investigate the fracture-like breakout mechanism at the microscopic particle scale. The numerical tool was verified against analytical solutions.

The DEM model was used to simulate drilling in the Castlegate sandstone in which the applied stresses were sufficiently high to generate breakout around the hole. The results show that fracture-like breakouts develop as a result of grain debonding, grain repacking and grain crushing in the direction of σ_h . Contrary to V-shaped breakouts, the failure mechanism in a fracture-like breakout is non-dilatant, and the failure zone has a lower porosity than the initial porosity. The compaction band is formed along the σ_h springline.

Stress analysis was conducted to explore the relation between far-field stresses and the size of the fracture-like breakout. It was found that the fracture length depends on both the mean stresses and the extent of stress anisotropy. Thus, fracture-like breakout length combined with other techniques (such as minifrac testing) could potentially be utilized to determine the principal *in situ* stress

magnitudes. It was also found that the width of the fracture-like breakout does not significantly change with changing far-field stresses.

The development of the V-shaped and fracture-like breakouts at isotropic stress conditions was also investigated using the DEM model. It was found that these breakouts could develop even under isotropic stress conditions due to either inherent rock anisotropy or heterogeneity.

Chapter 6: The relationship between the rock macro- and micro-properties and wellbore breakout type

6.1 Introduction

In Section 2.2.1, it was stated that physical and mechanical rock properties greatly influence the breakout mechanism and geometry. Previous research shows that macromechanical material properties (e.g., strength, ductility, and dilatancy) may not be sufficient to allow predicting the failure mechanism and the breakout type and such may be more accurately related to the rock micro-properties.

This chapter presents the outcomes of a numerical investigation on the effect of the material micro-parameters (i.e., particle micro-properties and cement micro-properties) on the failure mechanism and the geometry of the breakout. The numerical tool that was developed and verified in Chapter 5 is utilized to study the effect of material micro-parameters and the corresponding material macro-parameters on the breakout geometry in cubic rock samples subjected to pre-existing far-field stresses.

6.2 Numerical model

A series of numerical model testing simulations was conducted to investigate the effect of the micro and the corresponding macro material properties on the failure mechanism and breakout geometry. Test specimen were generated in a rectangular box of $0.18 \text{ m} \times 0.18 \text{ m} \times 0.02 \text{ m}$ ($W \times H \times D$) bounded by six rigid frictionless walls similar to those described in Section 5.3. The borehole breakout simulations were initially conducted for the base case in which the micro-properties of Castlegate sandstone were used (Table 5.1). The specimen consisted of 89,538 spherical particles of random sizes between 0.4 and 1.3 mm, which approximately captures the PSD of the Castlegate sandstone (Figure 5.1).

The macromechanical properties for the base case including Young's modulus, Poisson's ratio, UCS, friction angle, cohesion, and dilation angle were calibrated using triaxial testing data at different confining stresses. Elastic properties were determined at 50% of the peak stress (Jafarpour et al., 2012), and plastic

properties were calculated at the peak stress assuming the material obeys the MC model. In addition, the post-peak behavior was characterized by the post-peak modulus (see definition in Appendix C) and the residual stress (Joseph and Barron, 2003). The post-peak modulus was estimated using the slope of the stress strain curve after the peak, and the absolute value was adopted for the ease of comparison (Cheng, 2011). As the post-peak modulus and the residual stress vary with the confining stress, again for simplicity they were only determined for the triaxial test at a confining stress of 2.41 MPa. The macromechanical properties for the base case are listed in Table 6.1. The evaluation of the macromechanical properties for the base case is described in Appendix C.

Table 6.1 Mechanical properties for the base case

	The base case
Young's modulus (GPa)	5.1
Poisson's ratio	0.17
Friction angle °	46.5
Cohesion (MPa)	4.3
Dilation angle °	5
Post-peak modulus (GPa)	8.5
Residual stress (MPa)	11
Uniaxial compressive strength (MPa)	21.5

The borehole breakout simulations began by applying the maximum horizontal stress ($\sigma_H = 50$ MPa), the vertical stress ($\sigma_v = 30$ MPa), and the minimum horizontal stress ($\sigma_h = 20$ MPa) on the specimen. While maintaining the far-field stresses on the specimen, a vertical borehole (1.25 cm radius) was drilled by gradually decreasing the particles stiffness inside the borehole to zero and finally removing the particles inside the hole to create the hole. Then the model was cycled until the average unbalanced forces were low compared to the average contact forces (0.01 ratio was adopted here).

6.3 Numerical results

The borehole breakout simulations were initially performed using the Castlegate sandstone properties reflected in Table 5.1.

Figure 6.1 shows a horizontal cross section of the sample after completion of the drilling phase. Micro-scale damage at the contacts is presented by red lines for bonds failed in tension and blue lines for the bonds failed in shear. The yellow particles show intact particles, while the black ones indicate the crushed particles. Figure 6.1 shows the induced breakout is aligned with the minimum horizontal stress direction where the stress concentration is the highest. Breakout is initiated at the borehole wall by particle debonding and progressed with additional particle debonding and particle crushing, resulting in the formation of a compaction band in the direction of σ_h or the springline of the opening. This breakout resembles the fracture-like breakout observed in Castlegate sandstone (Cundall et al., 1999) and highly porous sandstones (Haimson, 2007) in laboratory drilling experiments.

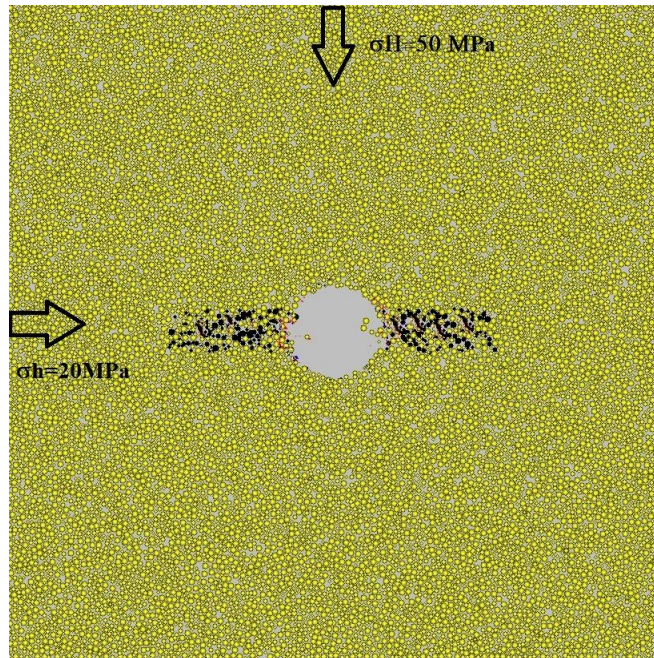


Figure 6.1 Borehole cross section of Castlegate sandstone (base case) showing fracture-like breakout ($\sigma_v=30$ MPa)

By the time the breakout developed, the total number of broken bonds was only 310, while 1,484 particles were crushed inside the compaction band. The initial average porosity of the specimen before drilling was assessed to be 0.34. The

average porosity along the compaction band after drilling was 0.325, which is less than the initial porosity (0.34). Thus it shows that the failure mechanism is not of dilatant nature as in V-shaped breakouts (Haimson, 2007). Also, the length of the reduced porosity zone from the borehole center was 4.3 cm.

A sensitivity study of the micro-parameters was carried out to determine the effect of each micro-parameter on the failure mechanism and breakout geometry. In addition, DEM simulation of triaxial tests was performed using various sets of micro-properties to assess the corresponding sets of macro-properties. When the effect of a certain micro-parameter was investigated, only that parameter was changed while the other parameters values were kept the same as the base case.

6.3.1 Effect of particle contact modulus (E_c)

The particle contact modulus (E_c) was varied to investigate its impact on the failure mechanism and failure pattern ($E_c = 1.5, 7$ and 15 GPa).

Figure 6.2 shows a horizontal cross section of the sample after the equilibrium state was reached. Figure 6.2a shows a V-shaped breakout around the hole face in the direction of σ_h for the particle contact modulus of 1.5 GPa. Inside the V-shaped breakout, parallel bonds are seen to break in either tension or shear (red and blue lines, respectively). The total number of broken bonds was 3,050, while only 76 particles were crushed at the tip of the breakout (black particles). The reason for the increased tendency for bond breakage at a low contact modulus lies in the fact that with a decrease in the particle contact modulus to 1.5 GPa, more loads are attracted to the parallel bonds, increasing the tendency for more parallel bonds breakage around the hole face. The average porosity in the failed zone was calculated to be approximately 0.43, which is higher than the initial porosity (0.34). This indicates a dilatant failure mechanism as expected in a V-shaped breakout.

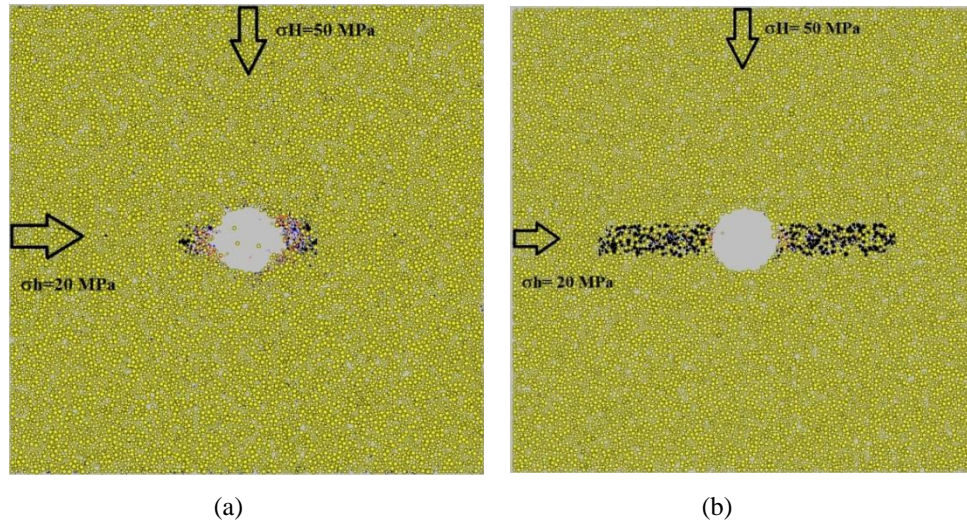


Figure 6.2 Borehole cross section (a) $E_c = 1.5$ GPa and (b) $E_c = 15$ GPa

On the other hand, with an increase in the particle contact modulus to 15 GPa, the breakout was in the form of a compaction band in the direction of σ_h (Figure 6.2b). The length of the compaction band from the center of the hole was 5.8 cm, which is more than the length of the compaction band in the base case (4.3 cm). There were 2,100 particles broken versus only 120 parallel broken bonds, which indicate the compactive nature of the breakout.

The results show that the particle contact modulus can affect the type of breakout around the hole. Stiffer particles appear to increase the tendency for fracture-like breakouts. The grain stiffness depends on the grain mineralogy. Sandstones are mainly composed of quartz and feldspar. Quartz is stiffer than feldspar. This could be the reason that the fracture-like breakout has been observed in drilling experiments in quartz-rich sandstones such as Berea sandstone and Mansfield sandstone (Haimson, 2007; Haimson and Lee, 2004).

Next, the corresponding macromechanical properties of each of the parametric analysis cases were calculated by DEM simulation of triaxial tests using the micro-properties. Figure 6.3 shows the stress-strain plots at confining stresses of 0, 2.41, and 5.17 MPa with varying particle contact moduli.

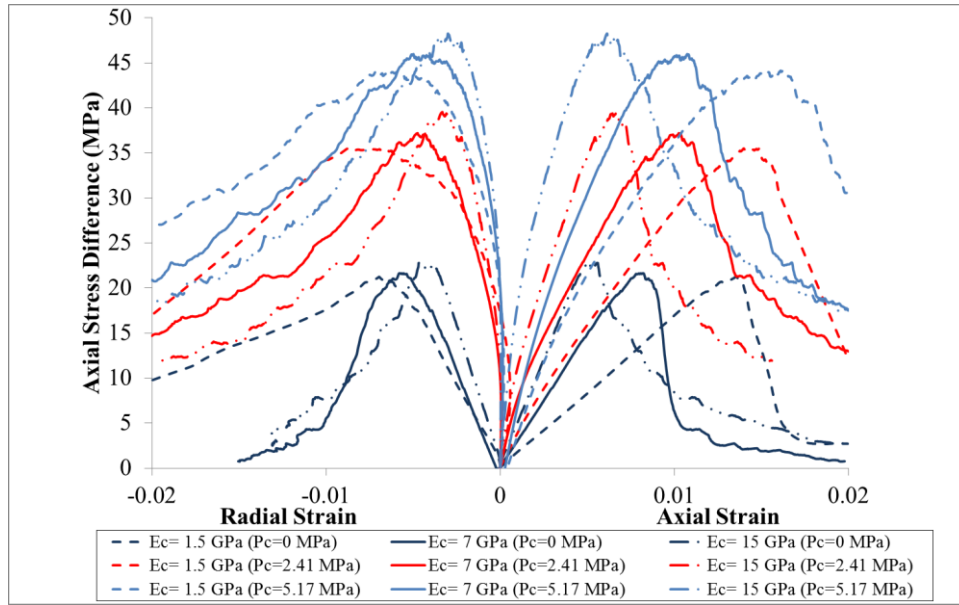


Figure 6.3 Stress-strain curves with varying E_c at different confining stresses

Table 6.2 shows that the macro Young's modulus of the specimen increased with an increase in the particle contact modulus, while the dilation angle decreased. Other macro-parameters did not change significantly with a change in the particle contact modulus.

Table 6.2 Mechanical properties for investigating the effect of E_c

	Test 1 ($E_c=1.5$ GPa)	The base case	Test 2 ($E_c=15$ GPa)
Young's modulus (GPa)	2.5	5.1	10
Poisson's ratio	0.17	0.17	0.18
Friction angle $^\circ$	45.8	46.5	47
Cohesion (MPa)	4.2	4.3	4.2
Dilation angle $^\circ$	9	5	2.3
Post-peak modulus (GPa)	8.3	8.5	8.5
Residual stress (MPa)	11.5	11	10.5
Uniaxial compressive strength (MPa)	21	21.5	21.5

The parametric study on the particle contact modulus shows that variation of the dilation angle or macro Young's modulus can coincide with the variation of the breakout type. The likelihood of fracture-like breakouts increases with the increase of Young's modulus and/or decrease of the dilation angle. On the other hand, the tendency for V-shaped breakouts increases at a higher dilation angle and lower Young's modulus.

6.3.2 Effect of cement strength

Table 6.3 shows the variation of S_{pb}^N and S_{pb}^S in a series of parametric analyses to investigate their impact on the breakout geometry and failure mechanism.

Table 6.3 Simulation investigating the effect of bond strengths

Test	S_{pb}^N (MPa)	S_{pb}^S (MPa)
3	120	270
4	200	450
The base case	400	900
5	600	1350

Figure 6.4a shows that parallel bonds were broken in either tension or shear (red and blue lines, respectively) in a uniform pattern around the hole face when the parallel bond strength was 30% of that of the base case. The total number of broken bonds was 18,000, while only 112 particles were broken at the tip of the breakout in the direction of σ_h (black particles). With a decrease in the parallel bond strength, the parallel bonds could break at a lower stress. The average porosity measurement in the failed zone was approximately 0.42, which is higher than the initial porosity (0.34). Thus, the failure mechanism is dilatant as expected in a uniform breakout.

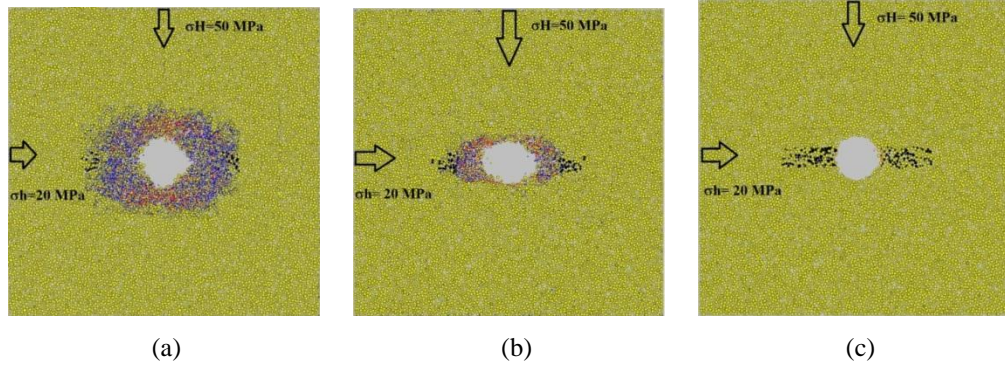


Figure 6.4 Borehole cross section (a) test 3 ($S_{pb}^N = 120$ MPa, $S_{pb}^S = 270$ MPa) (b) test 4 ($S_{pb}^N = 200$ MPa, $S_{pb}^S = 450$ MPa) (c) test 5 ($S_{pb}^N = 600$ MPa, $S_{pb}^S = 1350$ MPa)

In the next test, the parallel bond strength was reduced to 50% of that of the base case. Figure 6.4b shows the V-shaped breakout for this case. The total number of broken bonds amounted to 6,000, and 190 particles were broken at the tip of the breakout. The failure mechanism was also dilatant, and the average porosity in the failed zone was approximately 0.43.

With an increase in the parallel bond strength to 1.5 times that of the base case, the breakout type changed to a fracture-like breakout (Figure 6.4c). Fewer parallel bonds (total number of broken bonds = 85) and particles (total number of broken particles = 1,200) were broken in this test compared to the base case. The length of the compaction band from the center of the hole was 3.9 cm, which is less than the length of the compaction band in the base case (4.3 cm).

The results show that cement strength can affect the type of breakout around the hole. Stronger cements could result in fracture-like breakouts, while weaker cements could result in either uniform or V-shaped breakouts. The cement strength depends on the cement minerals. In general, three types of cement have been observed in sandstones: (1) silica cement; (2) carbonate cement; and (3) clay cement. Silica cement is usually stronger than the other two; therefore, based on our numerical studies, we expect fracture-like breakouts during drilling experiments for sandstones with silica cement.

Next, the macromechanical properties of the samples with varying parallel bond strengths were calculated and listed in Table 6.4.

Table 6.4 Mechanical properties for investigating the effect of bond strengths

	Test 3	Test 4	The base case	Test 5
Young's modulus (GPa)	5.7	5.5	5.1	4.8
Poisson's ratio	0.16	0.15	0.17	0.18
Friction angle °	23	37	46.5	52
Cohesion (MPa)	3.47	3.6	4.3	7.5
Dilation angle °	4	5	5	6.2
Post-peak modulus (GPa)	7.9	8.3	8.5	8.7
Residual stress (MPa)	8.6	9.5	11	16
Uniaxial compressive strength (MPa)	10	14	21.5	44

The table shows that the friction angle, the cohesion, and, therefore, the UCS of the specimen and the residual strength increased with an increase in the parallel bond strength, while the dilation angle, the post-peak modulus, and elastic macromechanical properties did not change significantly.

With an increase in the parallel bond strength, higher deformation at the contacts is required to create large enough stresses to break the stronger bonds. It increases the axial and radial strains at which the onset of bond breakage is observed. For instance, the volumetric strain at maximum contraction for a triaxial test at a confining pressure of 2.41MPa was assessed to be 0.01, 0.017, 0.035, and 0.062 when the parallel bond strengths were 30%, 50%, 100%, and 150% of the strength in the base case, respectively. Therefore, with an increase in the bond strength, a higher peak strength and higher macro friction angle can be mobilized.

The conclusion is that the material strength (friction, cohesion, and residual stress) is related to the type of breakouts that will occur. Relatively weak sandstones (in our case, UCS < 10 MPa) tend to develop uniform failure around the hole, while stronger sandstones (in our case, UCS > 20 MPa) tend to develop fracture-like

breakouts. Moderately strong sandstones (in our case, UCS \sim 14 MPa) also tend to develop V-shaped breakouts.

6.3.3 Effect of the percentage of bonded contacts (λ)

The effect of the percentage of bonded contacts (λ) was studied by choosing $\lambda = 20\%$ and 45% (base case was $\lambda = 30\%$) and investigating the breakout geometry and failure mechanism.

Figure 6.5 shows that the breakout type for the tests with different degrees of bonding did not change, and fracture-like breakouts for all three tests were observed.

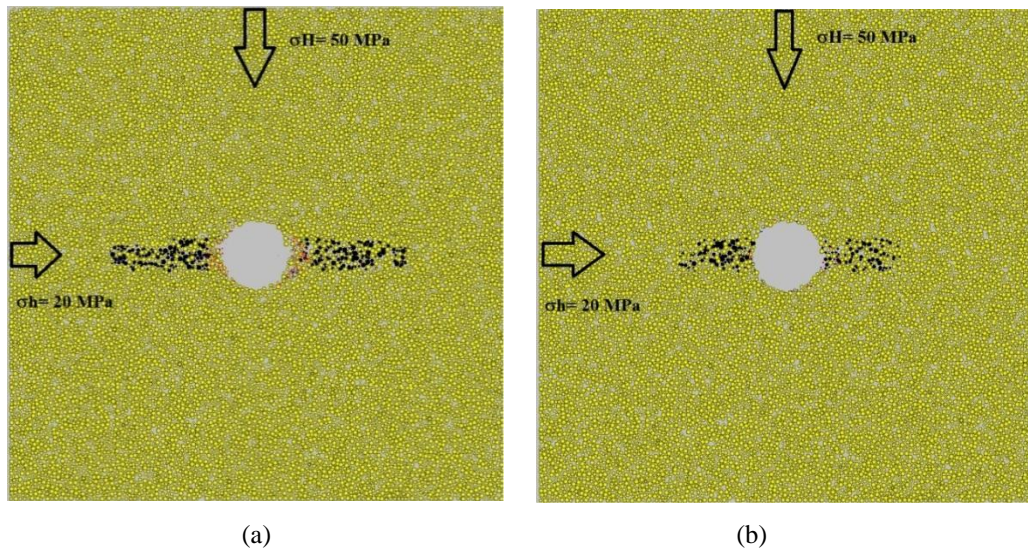
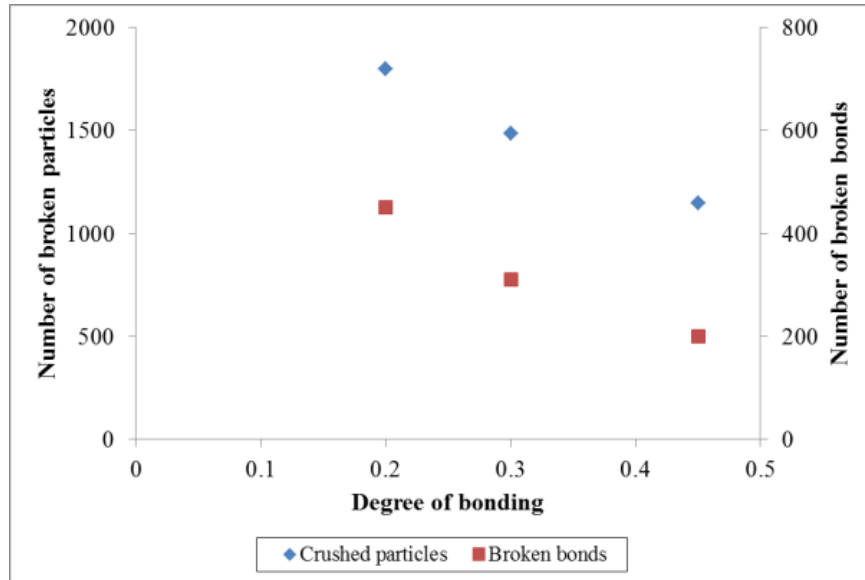
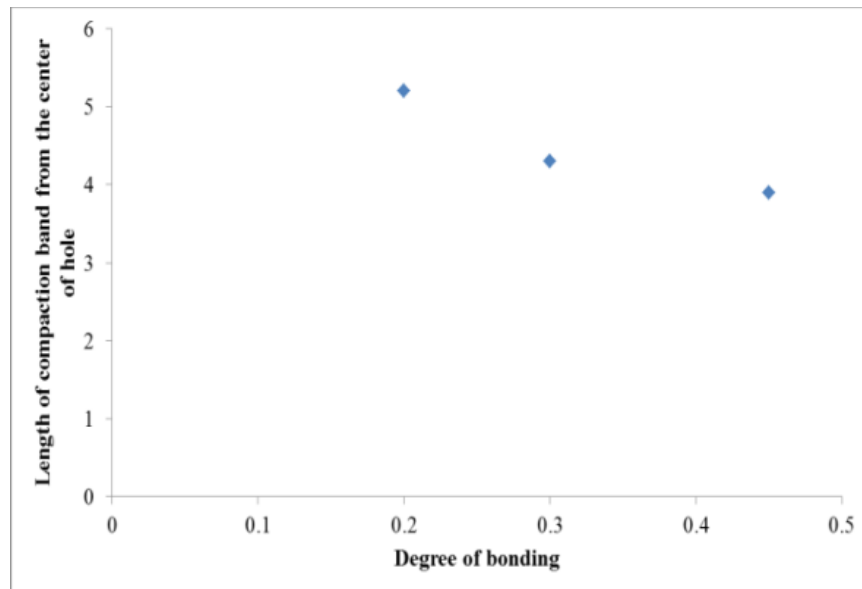


Figure 6.5 Borehole cross section (a) test 6 ($\lambda=0.2$) (b) test 7 ($\lambda=0.45$)

However, with an increase in the percentage of bonded contacts, the total number of broken particles and broken bonds (Figure 6.6a) and, therefore, the length of the compaction band (Figure 6.6b) decreased. The reason seems to lie in the fact that an increase in the percentage of bonded contacts (increasing the total number of parallel bonds in the model) at the constant far-field stress conditions leads to a decrease in the amount of load carried by each parallel bond. Also the distribution of the load carried by the particles becomes more uniform. Thus, fewer numbers of particles crush and fewer parallel bonds break.



(a)



(b)

Figure 6.6 The effect of degree of bonding on (a) broken bonds and broken particles (b) the length of the compaction band

Table 6.5 shows the corresponding macromechanical properties of the samples with varying percentages of bonded contacts. An increase in λ (1) increased the macro-Young's modulus; (2) decreased the Poisson's ratio; (3) increased the cohesion and residual strengths; and (4) resulted in a more distinct peak stress followed by sharper strain softening (higher post-peak modulus). As λ increases, lower loads are attracted to each parallel bond at any axial load, boosting the peak

strength. These general trends were also numerically predicted by Schöpfer et al. (2009). In addition, the dilation angle increases with an increase in the percentage of bonded contacts.

Table 6.5 Mechanical properties for investigating the effect of the percentage of bonded contacts

	Test 6 ($\lambda=20\%$)	The base case ($\lambda=30\%$)	Test 7 ($\lambda=45\%$)
Young's modulus (GPa)	4.5	5.1	6.47
Poisson's ratio	0.2	0.17	0.14
Friction angle °	47	46.5	46.5
Cohesion (MPa)	3	4.3	9.5
Dilation angle °	-4	5	12
Post-peak modulus (GPa)	3.4	8.5	13
Residual stress (MPa)	8.4	11	16.2
Uniaxial compressive strength (MPa)	16	21.5	48

The results of this parametric study show that the variations in the cohesion (from 3 to 9.5 MPa), the UCS (from 16 to 48 MPa), the dilation angle (from -4° to 12°), and the post-peak modulus (from 3.4 to 13 GPa) caused by the variation of λ did not correlate with the type of fracture-like breakout for our parametric cases.

6.3.4 Effect of the friction coefficient between particles (μ)

The effect of the friction coefficient between particles on the failure pattern was also studied by varying μ ($\mu = 0.56$ and 3 ; base case was $\mu = 1.5$).

From Figure 6.7, it is clear that the breakout geometry for the tests with different friction coefficients between particles is in the form of a compaction band.

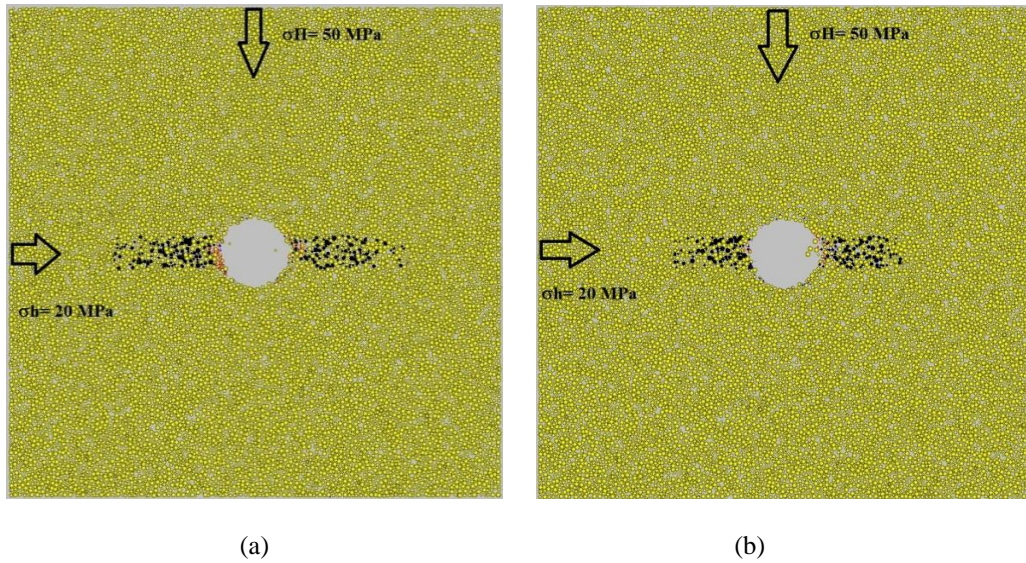
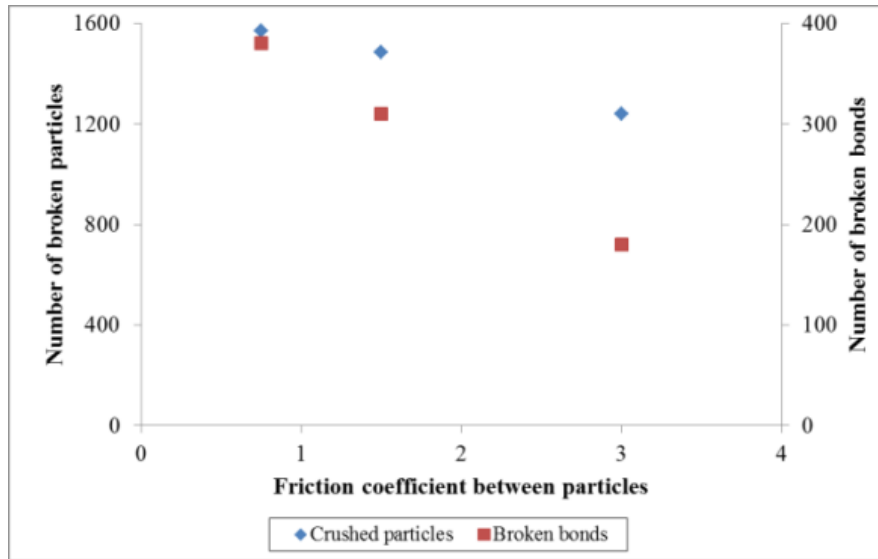
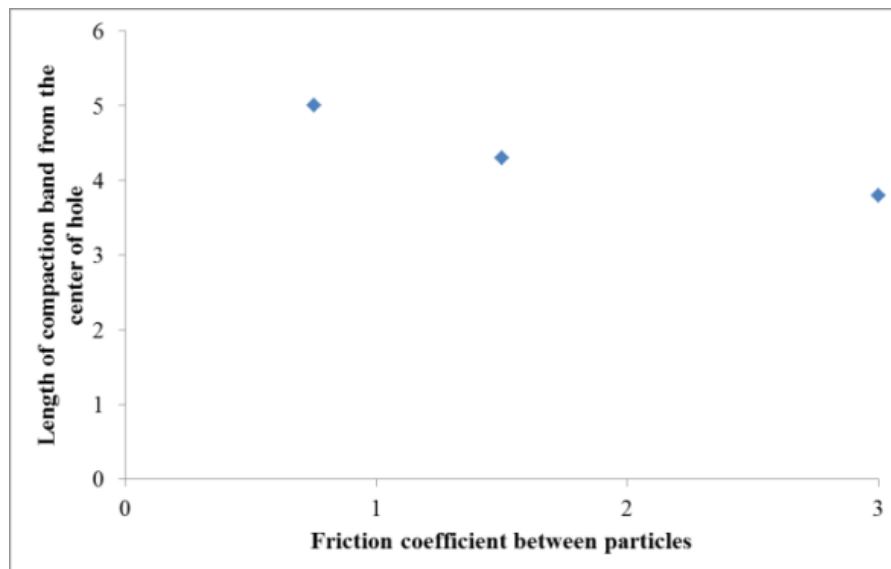


Figure 6.7 Borehole cross section (a) test 8 ($\mu=0.75$) (b) test 9 ($\mu=3$)

However, with a decrease in the friction between particles, the total number of broken particles and broken bonds (Figure 6.8a) and, therefore, the length of the compaction band, increased (Figure 6.8b). This can be attributed to the fact that for higher values of inter-particle friction, the particles can resist higher shear forces. Therefore, the normal inter-particle contact forces decrease and fewer particles break.



(a)



(b)

Figure 6.8 The effect of inter-particle friction on (a) broken bonds and broken particles (b) the length of the compaction band

Table 6.6 shows the corresponding macromechanical properties of each sample with varying friction coefficients between particles. It is evident that the macro Young's modulus increases with an increase in the friction coefficient between the particles. This can be explained as follows: as inter-particle friction increases, the particles are less free to slide and roll over each other. Therefore, less lateral strain is possible leading to a lower Poisson's ratio. With the increase in the

friction between particles, the sample becomes stronger, which results in the increase in the macro friction angle, cohesion, USC, and residual stress. It is interesting to note the impact of inter-particle friction on cohesion, which is conventionally thought to represent the rock cement strength.

Table 6.6 Mechanical properties for investigating the effect of the friction coefficient between particles

	Test 8 ($\mu=0.75$)	The base case ($\mu=1.5$)	Test 9 ($\mu=3$)
Young's modulus (GPa)	3.9	5.1	8.9
Poisson's ratio	0.28	0.17	0.12
Friction angle °	39	46.5	53
Cohesion (MPa)	3.75	4.3	4.65
Dilation angle °	-2	5	9
Post-peak modulus (GPa)	7.6	8.5	9.4
Residual stress (MPa)	5	11	21.3
Uniaxial compressive strength (MPa)	15.2	21.5	28

Careful examination of Table 6.6 shows that macro friction angles of specimens do not increase proportionally with the increase in the friction between particles. This can be attributed to fewer parallel bond failures with the increase in the friction coefficient between particles during loading. The total number of broken bonds at the peak strength of the uniaxial test was 400, 310, and 205 for μ values of 0.75, 1.5, and 3, respectively. Therefore, fewer particles could slip over each other, resulting in a lower macro friction angle at peak strength.

The results of this parametric study show that the variations in the Young's modulus (from 3.9 to 8.9 GPa), the Poisson's ratio (from 0.12 to 0.28 MPa), the macro friction angle (from 39° to 53°), and the residual stress (from 5 to 21.3 MPa) did not change the type of fracture-like breakout for our test case examples.

6.3.5 Effect of particle crushing strength

The effect of particle crushing strength on the breakout geometry was also studied by decreasing the average particle crushing strength to 40 MPa. The base case in this parametric study was different than that for other parametric studies so far. The new base case included a particle contact modulus of 1.5 GPa, which had resulted in V-shaped failure pattern (Figure 6.2a).

With a decrease in the particle crushing strength (from 60 to 40 MPa), the breakout type changed to a fracture-like breakout (Figure 6.9). The total number of broken particles was 1,510 (black particles), while 486 parallel bonds failed either in tension or shear, and the length of the compaction band from the center of the hole was assessed to be 4.5 cm.

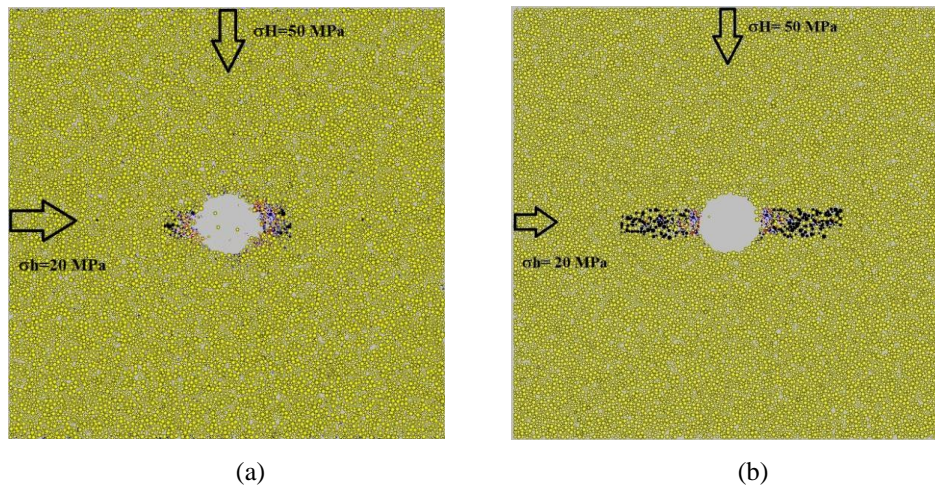


Figure 6.9 Borehole cross section for (a) particle crushing strength = 60 MPa, (b) particle crushing strength = 40 MPa

The results show that particle crushing strength can affect the type of breakout around the hole. Weaker particles could increase the tendency of fracture-like breakouts.

6.3.6 Effect of porosity

The effect of porosity on breakout geometry was also investigated using more uniform PSD (particle radius was chosen randomly between 0.7 and 0.8 mm) that resulted in an initial average porosity of 0.40. The base case in this parametric study was the case with the particle contact modulus of 1.5 GPa (initial average porosity = 0.34) for which the breakout was V-shaped (Figure 6.2a).

With an increase in the porosity, the breakout type changed to a fracture-like breakout with 1,580 broken particles and 345 broken parallel bonds (Figure 6.10). With an increase in porosity, hence decreasing the solid content in the sample, the particles carry higher loads, which increase the possibility of particle breakage. The average porosity measurement in the failed zone was around 0.37, which is lower than the initial porosity (0.40), indicating a compactive failure mechanism.

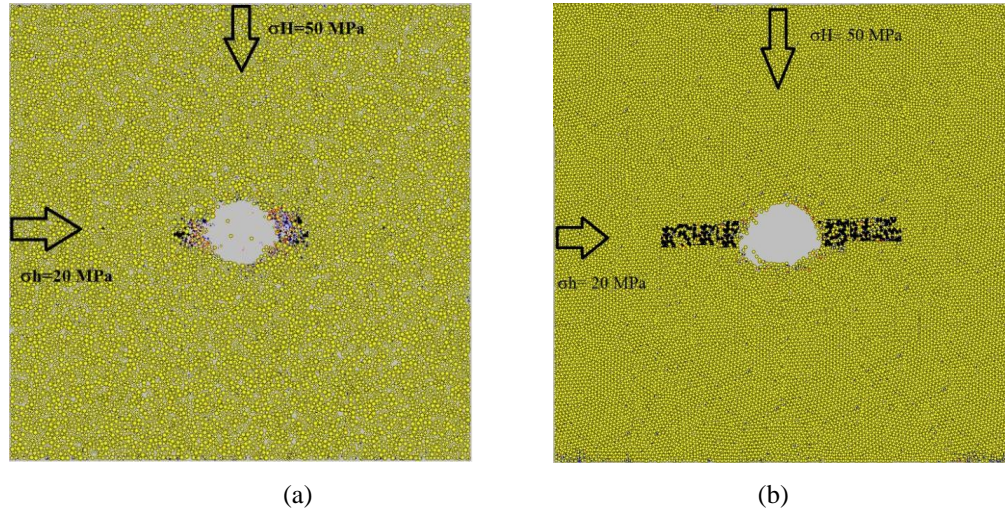


Figure 6.10 Borehole cross section for the sample with (a) initial porosity of 0.34, (b) initial porosity of 0.40

The result shows a higher tendency for fracture-like breakouts for higher porosity sandstones. The same has been observed in laboratory tests for high-porosity sandstones such as Berea sandstone and Mansfield sandstone (Haimson, 2007; Haimson and Lee, 2004).

6.3.7 Discussion

Figure 6.11 summarizes the effect of micro-parameters on the breakout morphology around the hole as determined from this research. It shows that lower bond strengths, which result in weaker rock, increase the likelihood of uniform breakouts. We saw nearly uniform breakout for this rock type despite anisotropic stress conditions. It also shows sandstones with weak, but stiff grains and strong bond strengths tend to develop fracture-like breakouts. This can be attributed to the higher potential for the development of a compaction band in these rocks. The grain crushing strength for a particle decreases with increasing particle diameters

(Nakata et al., 2001), while the particle contact modulus does not change. Therefore, there is a higher tendency of fracture-like breakouts for sandstones with higher mean grain sizes. Rocks with moderate bond strength (stronger than bond strengths that result in uniform breakouts, but weaker than the levels that result in fracture-like breakouts) tend to develop V-shaped breakouts particularly in anisotropic stress conditions.

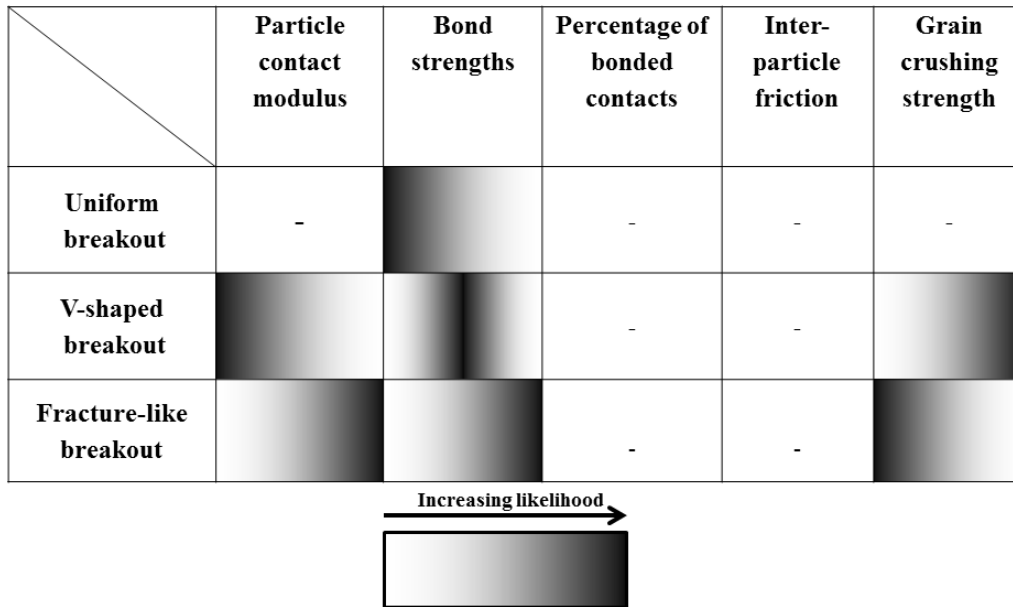


Figure 6.11 The effect of micro-parameters on borehole breakouts

Figure 6.12 summarizes the relationship between various macro-parameters and the type of breakout morphology around the hole as determined in this research. Figure 6.12 shows that the tendency for V-shaped breakouts increases with an increased dilation angle and/or decreased porosity. These results are consistent with the observations in drilling experiments for limestone, dolomite, and granite with low porosity (Guenot, 1989; Lee and Haimson, 1993; Shen et al., 2002; Zoback et al., 1985) and for dilatant sandstones (Cerasi et al., 2005; Li et al., 2006). It is to be noted that some of the relationships between the macro-parameters and the breakout morphology are of direct cause and effect nature (e.g., higher porosity increases the possibility of fracture-like breakout due to the higher tendency to developing compaction bands), while some others are simply correlations (e.g, it appears the relationship between dilation angle and V-shaped

breakout is a simple correlation). The relationship between the breakout type and dilation angle was concluded from the investigation on the effect of particle contact modulus. The tendency for V-shaped breakouts increases at lower particle contact modulus that also results in higher dilation angle.

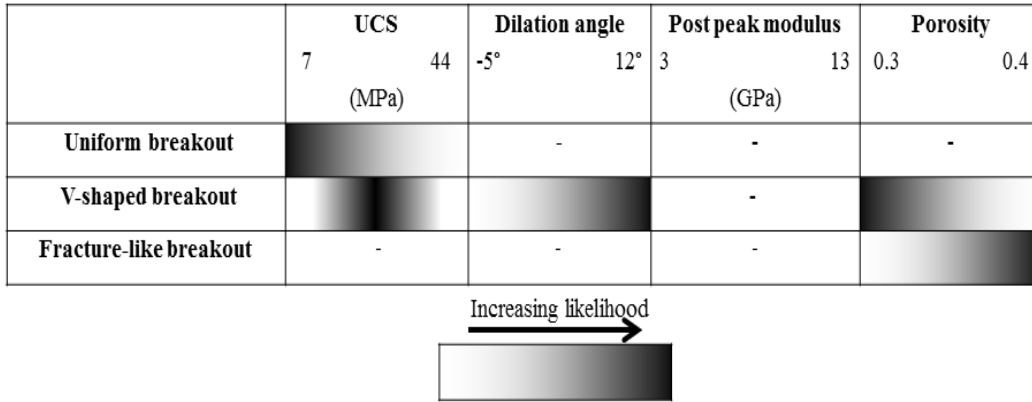


Figure 6.12 The effect of macro-parameters on borehole breakouts from DEM studies

The parallel bond strength simulations show that relatively weak sandstones tend to develop uniform failure around the hole, while moderately strong ones (in our case, UCS ~ 14 MPa) tend to develop V-shaped breakouts. Based on their experimental results, Cerasi et al. (2005) and Li et al. (2006) showed the development of uniform hole failure for relatively weak sandstones. Also Cerasi et al. (2005) experimentally showed that moderately strong sandstones tend to develop V-shaped breakouts.

Figure 6.12 also shows that higher porosity results in a higher likelihood of fracture-like breakout. Based on laboratory results, this type of breakout was observed in high-porosity sandstones such as Berea, Mansfield, and St. Peter (Haimson, 2007).

6.4 Conclusions

A 3D numerical model has been developed to investigate the effect of the particle and cement micro-parameters on the failure mechanism and geometry of the breakout. The model is based on the discrete element method and improved by implementing a grain-crushing algorithm. The numerical tool was verified against analytical solutions.

In the borehole breakout simulations, constant maximum horizontal, vertical, and minimum horizontal stresses (50, 30, and 20 MPa, respectively) were applied on the specimen. The results showed that the breakout morphology was affected by material micro-parameters such as the particle contact modulus, parallel bond normal and shear strengths, particle crushing strength, and PSD. The main findings are as follow:

- Stiffer particles, therefore higher particle contact moduli, increase the likelihood of fracture-like breakouts.
- Stronger cements increase the likelihood of fracture-like breakouts, while weaker cements could result in either uniform or V-shaped breakouts. The cement strength depends on the cement minerals deposited between the particles.
- Weaker particles could increase the tendency for fracture-like breakouts.

In addition, we conducted a series of triaxial tests to determine the effect of each micro-property on the macromechanical response of the sample. This allowed the examination of the relationship between the rock macro-properties and the breakout type. The main findings are as follows:

- Higher porosity sandstones tend to develop fracture-like breakouts.
- The tendency for V-shaped breakouts increases with either an increase in the dilation angle or a decrease in porosity.
- Moderately strong sandstones (in our case, UCS ~ 14 MPa) tend to develop V-shaped breakouts.
- Relatively weak sandstones (in our case, UCS < 10 MPa) tend to develop uniform failure around the hole.
- Young's modulus is not just affected by the particle contact modulus, but also by the friction coefficient between the particles and the percentage of bonded contacts.
- The dilation angle is a function of particle contact modulus, percentage of bonded contacts, and inter-particle friction.

- The friction angle is not just affected by the friction coefficient between the particles, but also by bond strengths.
- Cohesion is not just affected by bond strengths, but also by the friction coefficient between the particles.
- Post-peak modulus is affected by the percentage of bonded contacts and inter-particle friction.

Chapter 7: Conclusion

This thesis has described the micromechanical study of the borehole breakout using the discrete element method. The research methodology consists of numerical model development, model verification against analytical solutions, model validation against laboratory testing data, and an investigation of borehole breakouts around a borehole at the laboratory scale. This chapter summarizes the key points that can be concluded from this research.

7.1 DEM sandstone model development and calibration

A calibration methodology for 3D DEM models using a bonded particle model was presented. The proposed calibration procedure is based on a systematic trial-and-error method and comparison of laboratory and simulated triaxial tests. To minimize the number of iterations, the effect of micromechanical parameters was investigated on the macro responses of the simulated triaxial tests. The parametric studies showed that although the calibration was based on trial and error, different micro-parameters lead to different macromechanical responses. Identification of such trends allows an efficient calibration process with minimal trial and error.

DEM simulations were carried out to analyse SWS sandstone triaxial testing. In spite of its simplicity, the model reproduced the macro responses of SWS sandstone such as elastic behavior, peak stress, and post-peak behavior observed in laboratory testing.

The calibration was validated against TWC measurements for SWS sandstone and also verified against analytical solutions. The numerical results were quantitatively in agreement with the analytical and experimental results.

7.2 DEM model development for the simulation of borehole breakouts

A 3D numerical model has been developed to investigate fracture-like breakouts around wellbores due to drilling. The model is based on the discrete element method and improved by implementing a grain-crushing algorithm to investigate

the fracture-like breakout mechanism at the microscopic particle scale. The numerical tool was verified against analytical solutions.

The DEM model was used to simulate drilling in Castlegate sandstone in which the applied stresses were sufficiently high to generate breakout around the hole. The results show that a fracture-like breakout develops as a result of grain crushing and grain repacking in the direction of σ_h . Contrary to V-shaped breakout, the failure mechanism in fracture-like breakouts is non-dilatant, and the failure zone has a lower porosity than the intact rock. This is manifested in the formation of a compaction band along the σ_h springline.

A stress analysis was conducted to explore the relationship between far-field stresses and the size of the fracture-like breakout. It was found that the slit-facture length depends on both the mean stresses and the extent of stress anisotropy. It was also found that the width of the fracture-like breakout does not significantly change with a change in far-field stresses.

The development of V-shaped and fracture-like breakouts at isotropic stress conditions was investigated using the DEM model. It was found that these breakouts could develop even under isotropic stress conditions possibly due to the rock anisotropy or heterogeneity or both.

7.3 Micromechanical study of borehole breakout mechanism

The results showed that breakout morphology was affected by material micro-parameters, such as the particle contact modulus, parallel bond normal and shear strengths, particle crushing strength, and PSD. The main findings are as follows:

- Stiffer particles, therefore higher particle contact moduli, increase the likelihood of fracture-like breakouts.
- Stronger cements increase the likelihood of fracture-like breakouts, while weaker cements could result in either uniform or V-shaped breakouts. The cement strength depends on the cement minerals deposited between the particles.
- Weaker particles could increase the tendency for fracture-like breakouts.

In addition, we conducted a series of triaxial tests to determine the effect of each micro-property on the macromechanical response of the sample. The main findings are as follows:

- Higher porosity sandstones tend to develop fracture-like breakouts.
- The tendency for V-shaped breakouts increases with either an increase in dilation angle or a decrease in porosity.
- Moderately strong sandstones (in our case, UCS \sim 14 MPa) tend to develop V-shaped breakouts.
- Relatively weak sandstones (in our case, UCS $<$ 10 MPa) tend to develop uniform failure around the hole.
- Young's modulus is not just affected by particle contact modulus, but also the friction coefficient between the particles and the percentage of bonded contacts.
- The dilation angle is a function of particle contact modulus, percentage of bonded contacts and inter-particle friction.
- The friction angle is not just affected by the friction coefficient between the particles, but also by the bond strengths.
- Post-peak modulus is affected by the percentage of bonded contacts and the inter-particle friction.

7.4 Recommendations for future work

For further DEM model studies on borehole breakouts, the following future research is recommended:

- The idealization of spherical particles requires further review. More complex DEM models that contain denser packing by using non-spherical particles would enhance the model.
- As discussed in Chapter 1, fluid flow could also affect the breakout failure mechanism and geometry. Therefore, fluid flow analysis could be coupled with the mechanical DEM analysis.
- To study the borehole breakout problem at the field scale, hybrid models could be developed. DEM models are computationally inefficient, but

when combined with continuum models could be used for practical problems at the field scale.

Bibliography

- Alassi, H.T., Holt, R., 2011. Relating discrete element method parameters to rock properties using classical and micropolar elasticity theories. *International Journal for Numerical and Analytical Methods in Geomechanics*, Vol. 36, No. 10, pp. 1350–1367.
- Alvarado, G., 2007. Influence of late cementation on the behaviour of reservoir sands. PhD thesis, University of London, London.
- Barton, C.A., 1988. Development of in situ stress measurement techniques for deep drillholes, PhD thesis, Stanford University.
- Bazant, Z.P., Lin, F.B., Lippman, H., 1993. Fracture energy release and size effect in borehole breakout. *Int. J. Num. Anal. Meth. Geomech.*, Vol. 17, No. 1, pp. 1-14.
- Bazant, Z. P., Oh, B. H., 1983. Crack band theory for fracture of concrete. *Materials and structures (RILEM, Paris)*, Vol. 16, pp. 155-177.
- Belheine, N., Plassiard, J.-P., Donzé, F.-V., Darve, F., Seridi, A., 2009. Numerical simulation of drained triaxial test using 3D discrete element modeling. *Computers and Geotechnics*, Vol. 36, No. 1-2, pp. 320-331.
- Bell, J.S. and Gough, D.I., 1979. Northeast-southwest compressive stress in Alberta: Evidence from oil wells. *Earth and Planet Sci. Let*, Vol. 45, pp. 475-482.
- Bell, J.S., 1990. Investigating stress regimes in sedimentary basins using information from oil industry wireline logs and drilling records. *Geological society special publications*, Vol. 48, pp. 305-325.
- Bell, J.S., Caillet, G., Le Marrec, A., 1992. The present-day stress regime of the southwestern part of the Aquitaine Basin, France, as indicated by oil well data, *J. Structural Geology*, Vol. 14, pp. 1019-1032.
- Bell, J.S. and Babcock, E.A., 1986. The stress regime of the western Canadian basin and implication for hydrocarbon production. *Bull. Can. Petrol. Geol.*, Vol. 34, pp. 364-378.

- Bianco, L.C.B. and Halleck, P.M., 2001. Mechanisms of arch instability and sand production in two-phase saturated poorly consolidated sandstones. SPE 68932, SPE European Formation Damage Conference, Hague, Netherlands.
- Bratli, R. K., Risnes, R., 1979. Stability and failure of sand arches. SPE 8427, 54th Annual Fall Technical Conference and Exhibition of the Society of Petroleum Engineers of AIME, Las Vegas, NV, USA.
- Cerasi, P., Papamichos, E., Stenebraten, J.F., 2005. Qualitative sand-production prediction: friction-dominated flow model, SPE 94791.
- Charlez, Ph. A., Edition 1997. Rock mechanics: petroleum applications. Vol. 2, Edition Technips.
- Charlez, P.H., Segal, A, Heugas, O., Quenault, O., Chevreuse, S.T.R., 1989. Development of a microstatistical model for deep borehole ovalization in brittle rocks. ISRM International Symposium, Pau, France, Aug. 30 – Sep. 2.
- Cheng, C., 2011. Influence of discontinuities on post-peak behavior of rock in uniaxial compressive test by numerical study, International Conference on Multimedia Technology (ICMT), Hangzhou, July 26-28, pp. 6406-6409.
- Cheng, Y.P., Nakata, Y., Bolton, M.D., 2003. Discrete element simulation of crushable soil. *Geotechnique*, Vol. 53, No. 7, pp. 633–641.
- Cheung L.Y.G., 2010. Micromechanics of sand production in oil wells, PhD Thesis, Imperial College of London.
- Cheung, L.Y.G, O'Sullivan, C., 2008. Effective simulation of flexible lateral boundaries in two- and three-dimensional DEM simulations. *Particuology*, Vol. 6, No. 6, pp. 483-500.
- Cho, N., Martin, C.D., Sego, D.C., 2007. A clumped particle model for rock. *International Journal of Rock Mechanics and Mining Sciences*, Vol. 44, No. 7, pp. 997-1010.
- Coates, D.R., Denoo, S.A., 1981. Mechanical properties program using borehole analysis and Mohr's circle. *Proceeding SPW/La 22nd annual logging symposium*. pp. 23-26.

- Couroyer, C., Ning, Z., Ghadiri, M., 2000. Distinct element analysis of bulk crushing: effect of particle properties and loading rate. *Powder Technology*, Vol. 109, No. 1-3, pp. 241–254.
- Crook, T., Willson, S., Yu, J. G., Owen, R., 2003. Computational modeling of the localized deformation associated with borehole breakout in quasi-brittle materials, *Journal of Petroleum Science and Engineering*, Vol. 38, No.3, pp. 177-186.
- Crough, S.L., Staffield, 1983. *Boundary element methods in solid mechanics*, George allen & Unwin, London.
- Cui, L., 2006. Developing a virtual test environment for granular materials using discrete element modeling. PhD thesis, University College Dublin.
- Cundall, P. A., 1971. A computer model for simulating progressive large scale movement in blocky rock systems. *Proceeding Symposium in international society of rock mechanics*, No. 11-8, Nancy, France.
- Cundall, P.A., Damjanac, B., Pestman, B.J., 1999. Compression cracks observed in numerical simulations of a thick wall cylinder in porous sandstone. *EOS Trans AGU*, Union 80:F1068.
- Cundall, P.A., Strack, O.D.L., 1979. A discrete numerical model for granular assemblies. *Geotechnique*, Vol. 29, No.1, pp. 47-65.
- Detournay, C., 2009. Numerical modelling of the slit mode of cavity evolution associated with sand production. *SPEJ*, Vol. 14, No. 4, pp. 797-804.
- Dusseault, M., 1993. Cold production and enhanced oil recovery. *Journal of Canadian Petroleum Technology*, Vol. 32, No. 4, pp 16-18.
- Edwards, D. P., Sharma, Y., Charron, A., 1983. Zones of sand production identified by log-derived mechanical properties: a case study. *Proceeding SPWLA 8th European formation evaluation symposium*, London.
- Eringen, A.C., 1966. *Mechanics of micromorphic materials*, Proc. 11th Int. Congr. Appl. Mech., Munich, Germany, Springer-Verlag, Berlin, pp. 131-138.
- Fakhimi, A., Villegas, T., 2007. Application of dimensional analysis in calibration of a discrete element model for rock deformation and fracture. *Rock Mechanics and Rock Engineering*, Vol. 40, No. 2, pp. 193-211.

- Geilikman, M.B., Dusseault, M.B., Dullien, F.A.L., 1994. Fluid-saturated solid flow with propagation of a yielding front. SPE/ISRM Rock Mechanics in Petroleum Engineering Conference, Delft, The Netherlands.
- Germanovich, L.N., Dyskin, A.V., 2000. Fracture mechanisms and instability of openings in compression, *International Journal of Rock Mechanics and Mining Sciences*, Vol. 37, No. 1-2, pp. 263-284.
- Gough, D.I. and Bell, J.S., 1981. Stress orientations from oil-well fractures in Alberta and Texas, *Can. J. Earth Sci.*, Vol. 18, pp. 638-645.
- Gough, D.I., Bell, J.S., 1982. Stress orientations from borehole wall fractures with examples from Colorado, east Texas, and Northern Canada. *Can. J. of Earth Sci.*, Vol. 19, No. 7, pp. 1358-1370.
- Guenot, A., 1989. Borehole breakouts and stress fields. *International Journal of Rock Mechanics and Mining Sciences and Geomechanics*, Vol. 26, No. 3, pp 185-195.
- Haimson, B.C., 2001. Fracture-like borehole breakouts in high-porosity sandstone: Are they caused by compaction bands, *Physics and Chemistry of the Earth Part A Solid Earth and Geodesy*, Vol. 26, No. 1, 2, pp. 15-20.
- Haimson, B.C., 2007. Micromechanisms of borehole instability leading to breakouts in rocks, *Int. J. Rock. Mech. Min. Sci.*, Vol. 44, pp. 157-17.
- Haimson, B.C., Herrick, C.G., 1989. Borehole breakouts and in situ stress, *Proc. 12th Annual Energy-Sources Technology Conf. and Exhib., Drilling Symp.*, 22, 17-22, Houston, TX.
- Haimson, B.C., Kovacich, J., 2003. Borehole instability in high-porosity Berea sandstone and factors affecting dimensions and shape of fracture-like breakouts. *Engineering Geology*, Vol. 69, No. 3-4, pp. 219-231.
- Haimson, B., Lee, H., 2004. Borehole breakouts and compaction bands in two high-porosity sandstones. *Int. J. Rock Mech. Min. Sci.*, Vol. 41, pp. 287-301.
- Haimson, B.C., Song, I., 1993. Laboratory study of borehole breakouts in Cordova Cream: a case of shear failure mechanism. *Int. J. Rock Mech. Min. Sci. Geomech. Abstr.*, Vol. 30, No. 7, pp. 1047-1056.

- Haimson, B.C., Song, I., 1998. Borehole breakouts in Berea sandstone: two porosity-dependent distinct shapes and mechanism of formation. *Rock Mechanics in Petroleum Engineering*, Trondheim, Norway, July 8-10.
- Herrick, C.G. and Haimson, B.C., 1994. Modeling of episodic failure leading to borehole breakouts in Alabama limestone, *Rock mechanics: models and measurements* (P. Nelson and S. Launbach, Eds), Austin, Balkema, Rotterdam.
- Hickman, S.H., Healy, J.H., Zoback, M.D, 1985. In situ stress, natural fracture distribution, and borehole elongation in the Auburn geothermal well, Auburn, New York, *J. Geophys. Res.*, Vol. 90, pp. 5497-5512.
- Holt, R.M., Kjolaas, J., Larsen, I., Li, L., Gotusso Pillitteri, A., Sonstebo, E.F., 2005. Comparison between controlled laboratory experiments and discrete particle simulations of the mechanical behaviour of rock. *International Journal of Rock Mechanics and Mining Sciences*, Vol. 42, No. 7-8, pp. 985-995.
- Itasca Consulting Group, Inc. PFC2D, Version 4.0. Minneapolis: Itasca, 2004.
- Itasca Consulting Group, Inc. PFC3D, Version 4.0. Minneapolis: Itasca, 2008.
- Itasca Consulting Group, Inc. UDEC, Minneapolis: Itasca, 2000.
- Jafarpour, M., Rahmati, H., Azadbakht, S., Nouri, A., Chan, D., Vaziri, H., 2012. Determination of Mobilized Strength Properties of Degrading Sandstone. *Journal of Soils and Foundations*, Vol. 52, No. 4, pp. 658-667.
- Jing, L., Stephansson, edition 2007. *Fundamentals of discrete element methods for rock engineering, theory and applications*. Elsevier.
- Joseph, T.G., Barron, K., 2003. The post-failure characteristics of rock. *Canadian Institute of Mining, Metallurgy and Petroleum*, Vol. 96, No. 1070, pp. 66-74.
- Kenter, C.J., Currie, P.K., 1998. Past and future of rock mechanics research to petroleum engineering, *SPE/ISRM Rock Mechanics in Petroleum Engineering*, 8-10 July 1998, Trondheim, Norway.
- Klaetch, A.R., Haimson, B.C., 2002. Porosity-dependent fracture-like breakouts in St. Peter sandstone. Hammah R, et al., editor. *Mining and tunneling*

- innovation and opportunity. University of Toronto Press, Toronto, pp. 1365-71.
- Kulatilake, P.H.S.W., Malama, B., Wang, J., 2001. Physical and particle flow modeling of jointed rock block behavior under uniaxial loading. *Int. J. of Rock Mechanics & Mining Sciences*, Vol. 38, No. 5, pp. 641-657.
- Kurt, R.S., Rudnicki, J.W., Pollard, D.D., 2005. Anticrack inclusion model for compaction bands in sandstone. *Journal of Geophysical Research*, Vol. 110.
- Kutter, H.K. and Rehse, H., 1996, Laboratory investigation of factor affecting borehole breakouts. *Eurock'96*, Barla (ed.), Balkema, Rotterdam, pp. 751-758.
- Kwong, A, Kaiser, P.K., 1989. Stability of tunnels in rock with localized weaknesses. In: Lo E, editor. *Proceedings of the international congress on progress innovation in tunneling*, Vol. 1, pp. 341-358.
- Lavrov, A., Cerasi, P., Papamichos E., 2005. Numerical modeling of sand production mechanisms with displacement discontinuity method. *SPE Europec/EAGE Annual Conference*, Madrid, Spain, June 13-16.
- Lee, M., Haimson, B., 1993. Laboratory study of borehole breakouts in Lac du Bonnet granite: a case of extensile failure mechanism. *Int. J. Rock Mech. Min. Sci. Geomech. Abstr.*, Vol. 30, No. 7, pp. 1039-1045.
- Leeman, E.R., 1964. The measurement of stress in rock: I. the principles of rock stress measurement; II. Borehole rock stress measuring instruments; III. The results of some rock stress investigations. *J. S. Afr. Inst. Min. Met.*, Vol. 65, pp. 254-284.
- Li, L., Holt, R., 2002. Particle scale reservoir mechanics. *Oil and Gas Science and Technology Rev. IFP*, Vol. 57, No. 5, pp. 525-538.
- Li, L., Papamichos, E., Cerasi, P., 2006. Investigation of sand production mechanisms using DEM with fluid flow, Multiphysics Coupling and Long Term Behaviour in Rock Mechanics *ISRM Eurock 2006*, Liège, Belgium.
- Marketos, G., Bolton, M.D., 2009. Compaction bands simulated in discrete element models. *Journal of Structural Geology*, Vol. 31, pp. 479-490.

- Martin, C.D., Martino, J.B., Dzik, E.J., 1994. Comparison of borehole breakouts from laboratory and field tests, Proc. EUROCK '94 Rock Mechanics in Petroleum Engineering, Delft, Balkema, Rotterdam.
- Mastin, L.G, 1984. Development of borehole breakouts in sandstone. MSc thesis, Stanford University.
- Mastin, L.G., Heinemann, B.B., Kremmer, K., Fuchs, K., Zoback, M.D., 1991. Stress orientation in the KTB pilot hole determined from wellbore breakouts. *Scientific drilling*, Vol. 2, pp. 1-12.
- McDowell, G.R., Amon, A., 2000. The application of Weibull statistics to the fracture of soil particles. *Soils and Foundations*, Vol. 40, No. 5, pp. 133-141.
- Muhlhaus, H.B., Aifantis, E. C., 1991. A variational principle for gradient plasticity. *Int. J. Solids Struct.*, Vol. 28, pp. 845-857.
- Muhlhaus, H.B., Vardoulakis, I., 1987. The thickness of shear bands in granular materials. *Geotechnique*, Vol. 37, No. 3, pp. 271-283.
- Nakata, Y., Kato, Y., Hyodo, M., Hyde, A.F.L., Murata, H., 2001. One-dimensional compression behaviour of uniformly graded sand related to single particle crushing strength. *Soils and Foundations*, Vol. 41, No. 2, pp. 39-51.
- O'Sullivan, C., 2002. The application of discrete element modelling to finite deformation problems in geomechanics. PhD thesis, University of California, Berkeley.
- O'Sullivan, C., Bray, J.D., Li, S., 2003. A new approach for calculating strain for particulate media. *International Journal for Numerical and Analytical Methods in Geomechanics*, Vol. 27, No. 10, pp.859-877.
- Pamin, J., 1994. Gradient-dependent plasticity in numerical simulation of localization phenomena. MSc thesis, Delft University of Technology, Delft.
- Papamichos, E., 2009. Borehole failure analysis in a sandstone under anisotropic stresses, *Int. J. Numer. Anal. Math. Geomech.*, Vol. 34, pp. 581-603.

- Papamichos, E., Malmanger, E. M., 2001. A sand erosion model for volumetric sand predictions in a North Sea reservoir. *SPE Reservoir Evaluation and Engineering Journal*, Vol. 4, No. 1, pp. 44-50.
- Papamichos, E., Tronvoll, J., Skjaerstein, A., Unander, T. E., 2010, Hole stability of Red Wildmoor sandstone under anisotropic stresses and sand production criterion, *JPSE*, Vol. 72, pp.78-92.
- Papamichos, E., Tronvoll, J., Skjaerstein, A., Unader, T.E., Vardoulakis, I., Sulem, J., 1996. The effect of plane-strain and isotropic loading in hollow-cylinder strength, *ISRM International Symposium- EUROCK 96*, September 2-5, Turin, Italy.
- Papamichos, E., Vardoulakis, I., Tronvoll, J., Skjaerstein, A., 2001. Volumetric sand production model and experiment. *International journal for numerical and analytical methods in geomechanics*, pp 789-808.
- Papanastasiou, P., Vardoulakis, I., 1992. Numerical treatment of progressive localisation in relation to borehole stability. *International journal of numerical analysis and methods in geomechanics*, Vol. 16, No. 6, pp. 389-424.
- Plumb, R.A., Hickman, S.H., 1985. Stress induced borehole elongation: A comparison between the four-arm dipmeter and the borehole televiewer in the Auburn geothermal well, *J. Geophys. Res.*, Vol. 90, pp. 5513-5521.
- Potyondy, D. O., Cundall, P.A., 2004. A bonded particle model for rock. *International journal of rock mechanics & mining science*, Vol. 41, No. 8, pp. 1329-1364.
- Rahmati, H., Nouri, A., Vaziri, H., Chan, D., 2012. Validation of predicted cumulative sand and sand rate against physical model test, *JCPT*, Vol. 51, No. 5, pp. 403-410.
- Rawlings, C.G., Barton, N.R., Bandis, Addis, M.A., Gutierrez, M.S., 1993, Laboratory and numerical discontinuum modelling of wellbore stability, *J. Pet. Technol.*, Vol. 45, No. 11, pp. 1086-1092.
- Risnes, R., Bratli, R. k., 1982. Sand stresses around a wellbore. *SPEJ*, Vol. 22, No. 6, pp. 883-898.

- Santarelli, F.J., Brown, E.T., 1989. Failure of three sedimentary rocks in triaxial and hollow cylinder compression tests. *Int. J. Rock Mech. Min. Sci. & Geomech. Abstr.*, Vol. 26, pp. 401-413.
- Sazzad Md. Mahmud, Islam, Md. Shafiqul, 2008. Macro and micro mechanical responses of granular material under varying interparticle friction. *Journal of Civil Engineering*, Vol. 32, No. 2, pp. 87-96.
- Schöpfer, M. P. J., Abe, S., Childs, C. & Walsh, J. J. 2009. The impact of porosity and crack density on the elasticity, strength and friction of cohesive granular materials: Insights from DEM modelling. *International Journal of Rock Mechanics and Mining Sciences*, Vol. 46, No. 2, pp. 250-261.
- Schöpfer, M.P.J, Childs, C, Walsh, J., 2006. Localisation of normal faults in multilayer sequences. *Journal of Structural Geology*, Vol. 28, No. 5, pp. 816-833.
- Shen, B., Stephansson, O., Rinne, M., 2002. Simulation of borehole breakouts using FRACOD2D, *Oil & Gas Science and Technology Journal*, Vol. 57, No. 5, pp. 579-590.
- Simpson, B. and Tatsuoka, E., 2008. Geotechnics: the next 60 years, *Geotechnique Journal*, Vol. 58, No. 5, pp. 357-368.
- Sluys, L.J., 1992. Wave propagation, localisation and dispersion in softening solids, PhD thesis, Delft University, Netherlands.
- Stein, N., 1988. Calculate drawdown that will cause sand production. *world oil*, pp. 48-49.
- Sulem, J., Vardoulakis, I., Papamichos, E., 1995. Continuum models for materials with micro-structure, John Wiley, pp. 201-237.
- Tawadrous, A. S., DeGagné, D., Pierce, M. & Mas Ivars, D. 2009. Prediction of uniaxial compression PFC3D model micro-properties using artificial neural networks. *International Journal for Numerical and Analytical Methods in Geomechanics*, Vol. 33, No. 18, pp. 1953-1962.
- Tronvoll, j., Fjaer, E., 1994. Experimental study of sand production from perforation cavities. *International Journal of Rock Mechanics and Mining Sciences & Geomechanics Abstracts*, Vol. 31, No. 5, pp 393-410.

- Tronvoll, J., Papamichos, E., Kessler, N., 1993. Perforation cavity stability: Investigation of failure mechanisms. *Journal of geotechnical engineering of hard soils-soft rocks*, pp 1687-1693.
- Tsoungui, O., Vallet, D., Charmet, J.C., 1999. Numerical model of crushing of grains inside two-dimensional granular materials. *Powder Technology*, Vol. 105, No. 1-3, pp. 190–198.
- van den Hoek, P. J., Hertogh, G. M. M., Kooijman, A. P., Kenter, C. J., Papamichos, E., 2000. A new concept of sand production prediction: Theory and laboratory experiments. *SPE Drilling & Completion J.*, Vol. 15, No. 4, pp. 261-273.
- van den Hoek, P.J., Smith, D.J., Kooijman, A.P., de Bree, Ph., Kenter, Khodaverdian, M., 1994. Size dependency of hollow-cylinder stability, *Rock Mechanics in Petroleum Engineering*, 29-31 August 1994, Delft, Netherlands.
- Vardoulakis, I., Sulem, J., Guenot, A., 1988, Borehole instabilities as bifurcation phenomena, *Int. J. Rock. Mech. Min. Sci. & Geomech. Abstr.*, Vol. 25, No. 3, pp. 159-170.
- Vaziri, H.H., Lemoine, E.M., Xiao, Y., 2002. Quantification of Sand Production Induced Improvement in Productivity Index, *Canadian Geotechnical Journal*, Vol. 39, No. 5, pp. 1088-1102.
- Vermeer, P. A., de Borst, R., 1984. Non-associated plasticity for soils, concrete and rock, *HERON*, Vol. 29, No. 3, pp. 1-62.
- Wang, C., Tannant, D.D., Lilly, P.A., 2003. Numerical analysis of the stability of heavily jointed rock slopes using PFC2D, *International Journal of Rock Mechanics and Mining Sciences*, Vol. 40, No. 3, pp. 415-424.
- Wu, B., Choi, S.K., Tan, C.P., 2005. Effect of stress anisotropic on cavity strength and implications in wellbore stability and sand production analyses, *Proc. 40th U.S. Symp. on Rock Mechanics*, Anchorage, AK.
- Yoon, J., 2007. Application of experimental design and optimization to PFC model calibration in uniaxial compression simulation. *International Journal of Rock Mechanics and Mining Sciences*, Vol. 44, No. 6, pp. 871-889.

- Zdravkovic, L., Carter, J., 2008. Contributions to geotechnique 1948 to 2008: Constitutive and numerical modelling. *Geotechnique Journal*, Vol. 58, No. 5, pp.405-412.
- Zheng, Z., Kemeny, J., Cook, N.G.W., 1989. Analysis of borehole breakouts. *Journal of Geophysical Research*, Vol. 94, No. B6, pp. 7171-7182.
- Zhou, Z.Y., Kuang, S.B., Chu, K.W., Yu, A.B., 2010. Discrete particle simulation of particle–fluid flow: model formulations and their applicability, *J. Fluid Mech.*, Vol. 661, pp. 482-510.
- Zoback, M.D., Moos, L., Mastin, L.G., Anderson, R.N., 1985. Wellbore breakouts and in situ stress, *J. Geophys. Res.*, Vol. 90, pp. 5523-5538.
- Zoback, M., Magee, M., 1991. Stress magnitudes in the crust: Constraints from stress orientation and relative magnitude data. *Phil. Trans. R. Soc. Lond. A*, Vol. 337, No. 1645, pp. 181-194
- Zoback, M., 2007. *Reservoir geomechanics*. Cambridge University Press.

Appendix A: Analytical expressions for the stresses around a wellbore

A.1 Analytical solutions for the effective stresses

Stress distribution around a vertical well drilled parallel to the vertical principal stress, σ_v , in an isotropic, elastic medium was described by Zoback (2007).

Zoback (2007) presented the effective stresses at the wellbore wall by using a cylindrical coordinate system as follows:

$$\sigma_{\theta\theta} = \sigma_h + \sigma_H - 2(\sigma_H - \sigma_h) \cos 2\theta - 2P_o - \Delta P \quad (\text{A.1})$$

$$\sigma_{rr} = \Delta P \quad (\text{A.2})$$

$$\sigma_{zz} = \sigma_v - 2\vartheta(\sigma_H - \sigma_h) \cos 2\theta - P_o \quad (\text{A.3})$$

where ΔP is the difference between the wellbore pressure and the pore pressure, P_o ; ϑ is the Poisson's ratio; and θ is measured from the azimuth of σ_H .

A.2 Analytical solutions for the stresses around a wellbore developed by Risnes et al. (1982)

Risnes et al. (1982) derived analytical expressions for the stresses around a wellbore or cavity using continuum-based elasticity and plasticity theories. They assumed axial symmetry around the well axis and that the material obeys the MC failure criterion. They considered a vertical cylindrical hole through a horizontal layer of porous and permeable rock. The geometry of the problem is shown in Figure A.1. It illustrates a disk of sand with an inner radius (R_i), outer radius (R_o), and height (h). The radius of the plastic zone is R_c , and P_o and P_i are the outer and inner fluid pressures, respectively.

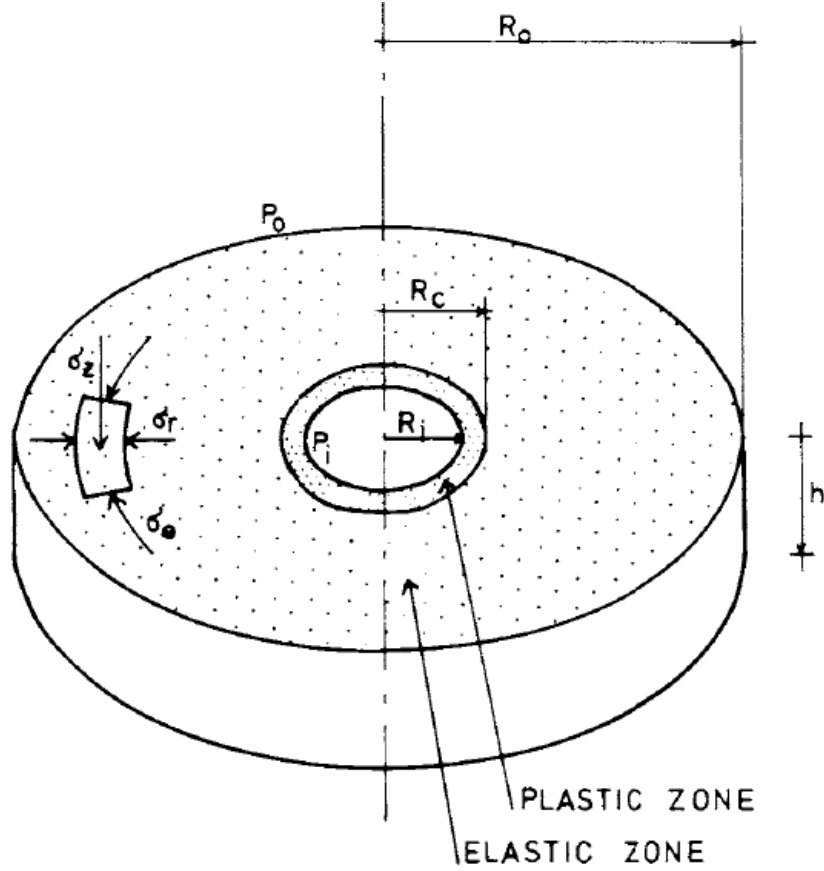


Figure A.1 Configuration of problem (Risnes et al., 1982)

The stress solutions in the elastic zone are given by

$$\sigma_r = \sigma_{ro} + (\sigma_{ro} - \sigma_{ri}) \frac{R_i^2}{R_o^2 - R_i^2} \left[1 - \left(\frac{R_o}{r} \right)^2 \right] - (P_o - P_i) \frac{1-2\nu}{2(1-\nu)} \beta \left\{ \frac{R_i^2}{R_o^2 - R_i^2} \times \left[1 - \left(\frac{R_o}{r} \right)^2 \right] + \frac{\ln(R_o/r)}{\ln(R_o/R_i)} \right\} \quad (\text{A.4})$$

$$\sigma_\theta = \sigma_{ro} + (\sigma_{ro} - \sigma_{ri}) \frac{R_i^2}{R_o^2 - R_i^2} \left[1 + \left(\frac{R_o}{r} \right)^2 \right] - (P_o - P_i) \frac{1-2\nu}{2(1-\nu)} \beta \left\{ \frac{R_i^2}{R_o^2 - R_i^2} \times \left[1 + \left(\frac{R_o}{r} \right)^2 \right] + \frac{1}{\ln(R_o/R_i)} \left[\ln \left(\frac{R_o}{r} \right) - 1 \right] \right\} \quad (\text{A.5})$$

$$\sigma_z = \sigma_{zo} + 2\vartheta(\sigma_{ro} - \sigma_{ri}) \frac{R_i^2}{R_o^2 - R_i^2} - (P_o - P_i) \frac{1-2\vartheta}{2(1-\vartheta)} \beta \left\{ \vartheta \frac{2R_i^2}{R_o^2 - R_i^2} + \frac{2}{\ln(R_o/R_i)} \left[\ln\left(\frac{R_o}{r}\right) - \frac{\vartheta}{2} \right] \right\} \quad (\text{A.6})$$

where ϑ is Poisson's ration; and β depends on the rock matrix and rock bulk compressibilities, and normally has a value close to one.

The stress solutions in the plastic zone are given by

$$\sigma_r = P_i + \frac{q\mu}{2\pi hk} \ln\left(\frac{r}{R_i}\right) + \frac{1}{t} \left(2C \tan \alpha - \frac{q\mu}{2\pi hk} \right) \left[\left(\frac{r}{R_i}\right)^t - 1 \right] \quad (\text{A.7})$$

$$\sigma_\theta = P_i + \frac{q\mu}{2\pi hk} \left(1 + \ln\left(\frac{r}{R_i}\right) \right) + \frac{1}{t} \left(2C \tan \alpha - \frac{q\mu}{2\pi hk} \right) \left[(t+1) \left(\frac{r}{R_i}\right)^t - 1 \right] \quad (\text{A.8})$$

$$\sigma_z = [2\vartheta(1-\beta) + \beta] \left(P_i + \frac{q\mu}{2\pi hk} \ln\left(\frac{r}{R_i}\right) \right) + \vartheta \frac{q\mu}{2\pi hk} + \frac{(1+\vartheta)(1-2\vartheta)}{1-\vartheta} (\sigma_{zo} - \beta P_o) + \frac{\vartheta}{t} \left(2C \tan \alpha - \frac{q\mu}{2\pi hk} \right) \left[(t+2) \left(\frac{r}{R_i}\right)^t - 2 \right] \quad (\text{A.9})$$

$$t = \tan^2 \alpha - 1 \quad (\text{A.10})$$

$$\alpha = \pi/4 + \varphi/2 \quad (\text{A.11})$$

where C is cohesion; φ is friction angle; q is flow rate; and μ is fluid viscosity.

Appendix B: Summary of 3D DEM calibration for Castlegate sandstone

This appendix summarizes the calibration of the 3D DEM model using laboratory experiments for Castlegate sandstone.

The set of DEM input parameters required to capture the macro-scale response of the Castlegate sandstone was selected using the algorithm described in Chapter 4. These micro-properties were calibrated such that a match was obtained between the DEM responses and the laboratory measurements. The calibration was validated against a series of triaxial tests performed on Castlegate sandstone. Figure B.1 shows the result of drained triaxial tests conducted at confining stresses of 0, 2.41, 5.17, and 7.58 MPa.

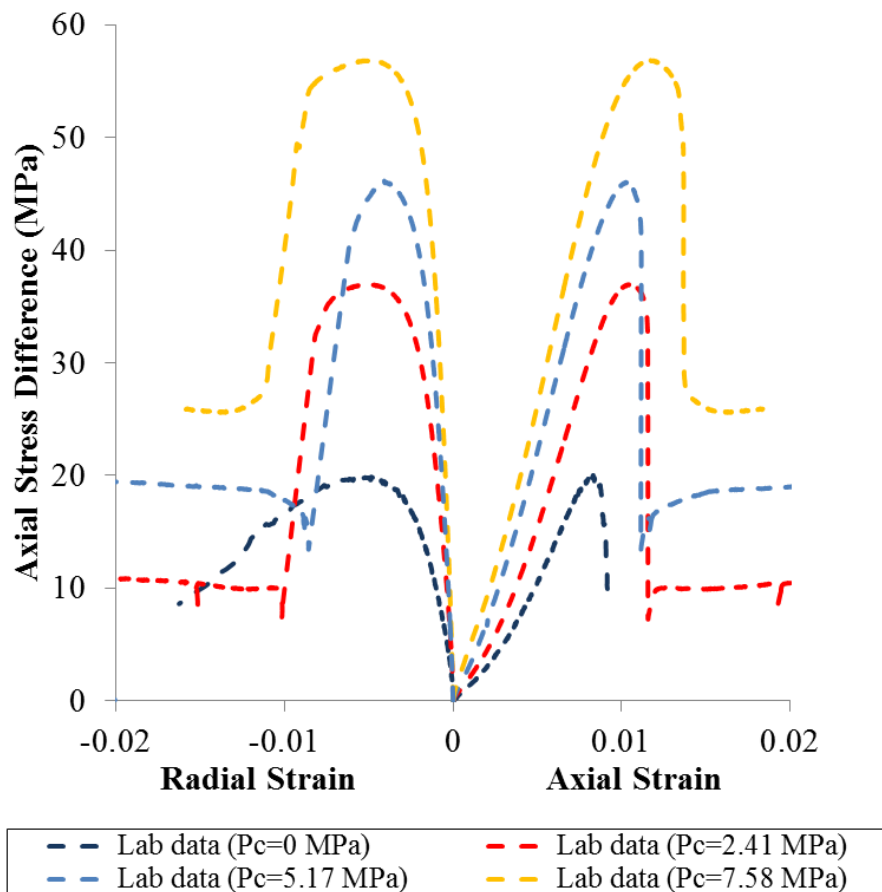


Figure B.1 Stress-strain curves for Castlegate sandstone at different confining stresses

B.1 Calibration process

The DEM particles were generated in a rectangular box of $0.1 \text{ m} \times 0.1 \text{ m} \times 0.2 \text{ m}$ bounded by rigid walls using the algorithm described in Chapter 4. The specimen particle sizes were chosen randomly between 0.4 and 1.3 mm, which approximately captures the PSD of the Castlegate sandstone (Figure B.2).

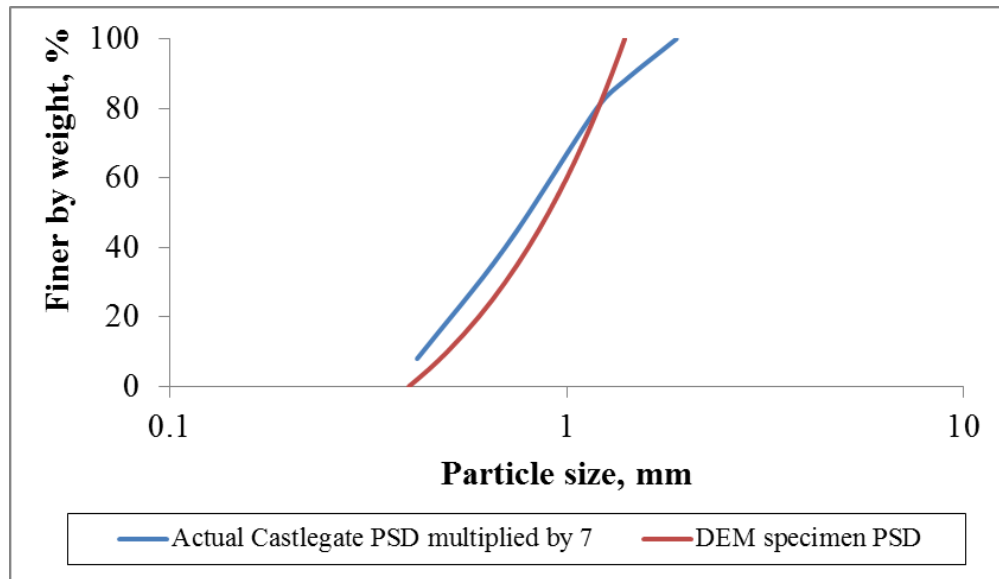


Figure B.2 Comparison between the actual Castlegate PSD and the DEM specimen PSD

The walls were moved slowly using a servo control algorithm, until the block reached an isotropic stress state of 0.2 MPa. This low value of isotropic stress is around 1% of UCS. Parallel bonds were randomly installed at 30% of the contacts detected at this stage, and the bond radius multiplier was varied randomly between 0 and 1 based on the observations from the SEM images for the Castlegate sandstone (Cheung, 2010). From the SEM image of Castlegate sandstone (Figure B.3), it is evident that not every grain-grain contact in the Castlegate sandstone is cemented. For example, Location A is a cemented contact, Location B is an uncemented contact, and the cement is cracked at Location C. It also shows that the degree of cementation varies at the contacts. A friction coefficient was assigned to all particles.

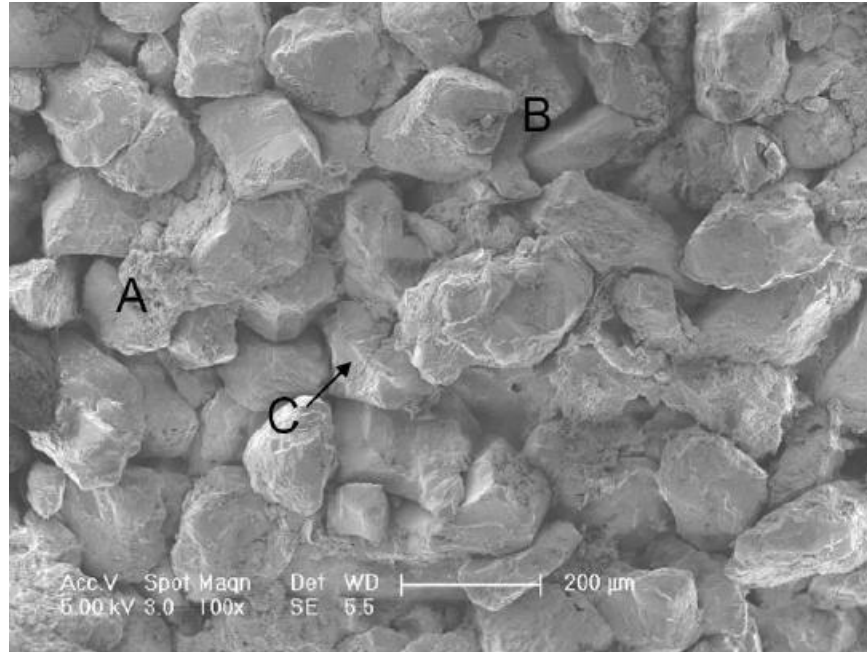


Figure B.3 The SEM image for the Castlegate sandstone (Cheung, 2010)

Finally, in order to reduce the boundary effects on the specimen generation process, a cylindrical specimen with a diameter of 50 mm and height of 100 mm was cut from the block.

Calibration of the DEM model parameters is based on trial and error and comparison of laboratory and simulated triaxial tests. In order to minimize the number of iterations, the calibration sequence developed in Chapter 4 was used.

The set of DEM micro-parameters found to capture the overall behavior of the Castlegate sandstone is summarized in Table B.1.

Table B.1 Calibrated micro-parameters for the Castlegate sandstone DEM model

Particle properties		Parallel bond properties	
Particle contact modulus, E_c (GPa)	7	Cement Young's modulus, E_{pb} (GPa)	20
The ratio of normal to shear stiffness of the particles, $\frac{K^N}{K^S}$	0.2	The ratio of normal to shear stiffness of the cement, $\frac{K_{pb}^N}{K_{pb}^S}$	0.2
The particle friction coefficient, μ	1.5	Normal strength of the cement, S_{pb}^N (MPa)	400
Particle radius (mm)	0.4 to 1.3	Shear strength of the cement, S_{pb}^S (MPa)	900
Particle density, ρ_s (kg/m ³)	2650	The percentage of bonded contacts, λ (%)	30
		The radius multiplier, α	Randomly distributed between 0 and 1

B.2 Triaxial test simulation

The triaxial test simulations were performed using a procedure described in Section 4.3.

Figure B.4 compares the macro responses of the 3D DEM model under different confining stresses with the corresponding laboratory results.

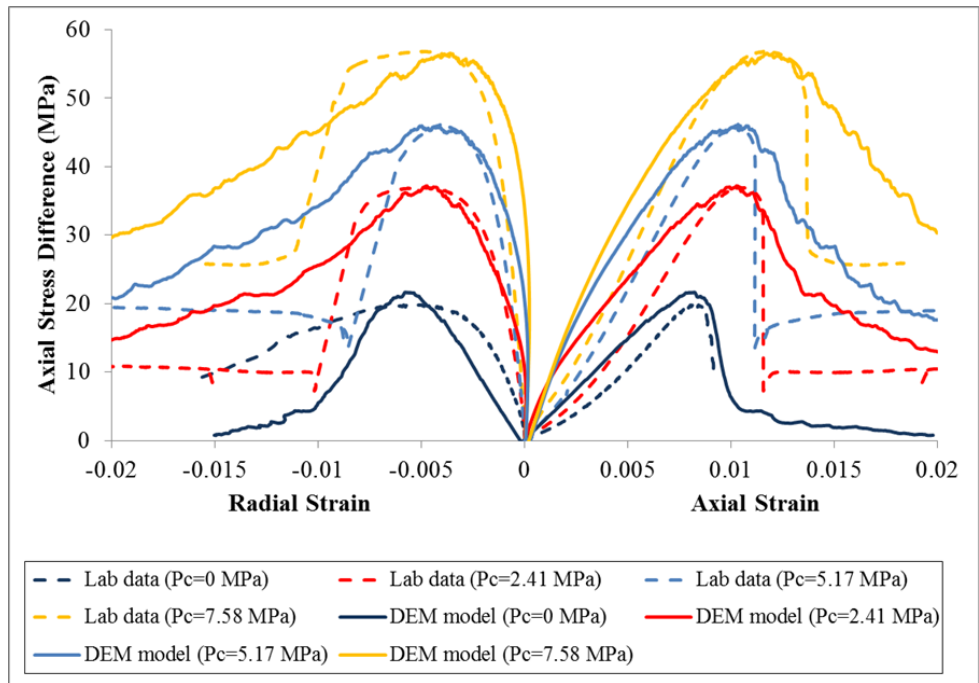


Figure B.4 Comparison between triaxial DEM model and laboratory results

Appendix C: The evaluation of macromechanical properties for the base case

In this appendix, the macromechanical properties for the base case were calibrated using triaxial testing data at different confining stresses.

Figure C.1 shows the stress-strain curves for the base case.

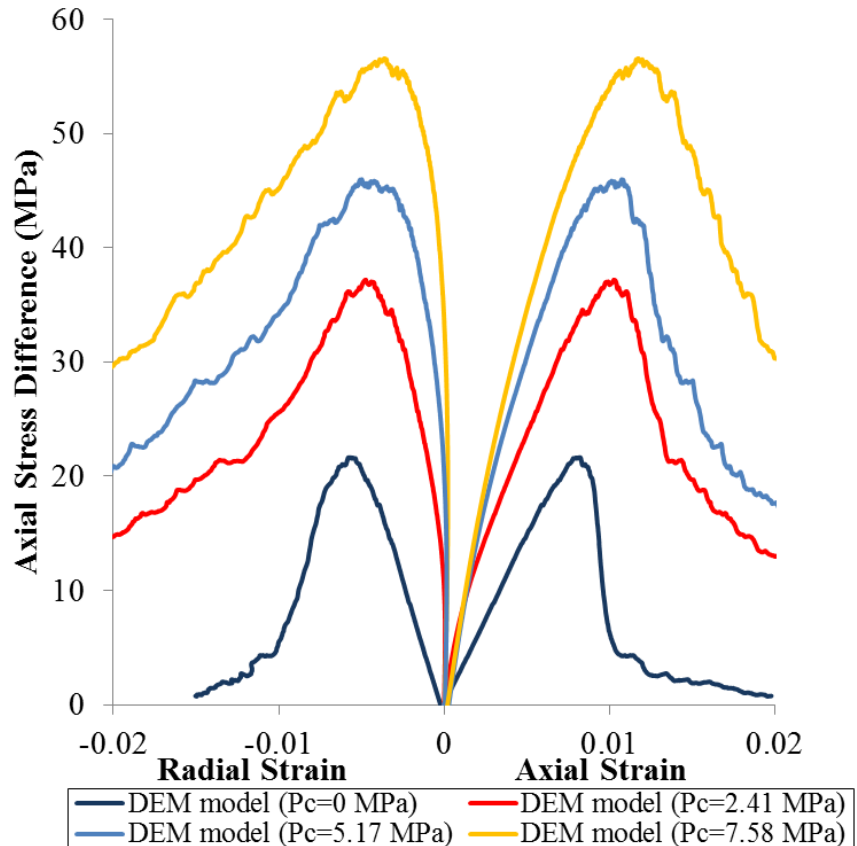


Figure C.1 Stress-strain curves for the base case at different confining stresses

C.1 Elastic properties

Stress- and damage-dependent elasticity is commonly observed in sandstone and more generally in granular materials. For simplicity, elastic parameters are assumed to depend only on the effective confining stress (Jafarpour et al., 2012).

In the simulations, elastic properties were determined at 50% of the peak stress for the triaxial test at a confining stress of 2.41 MPa as recommended by Jafarpour et al. (2012).

The Young's modulus and Poisson's ratio for the base case were calculated using:

$$\vartheta = -\frac{\Delta\varepsilon_r}{\Delta\varepsilon_a} \rightarrow \vartheta_{base\ case} = 0.17 \quad (C.1)$$

$$E = \frac{\Delta\sigma_a}{\Delta\varepsilon_a} \rightarrow E_{base\ case} = 5.1\ \text{GPa} \quad (C.2)$$

where ε_r is radial strain; ε_a is axial strain; and σ_a is axial stress.

C.2 Plastic properties

Plastic properties were calculated at the peak stress assuming the material obeys the MC model.

The MC failure criterion is given by

$$\sigma_1 = \sigma_3 \tan^2 \left(\frac{\pi}{4} + \frac{\varphi}{2} \right) + 2C \tan \left(\frac{\pi}{4} + \frac{\varphi}{2} \right) \quad (C.3)$$

where σ_1 is the greatest principal effective stress; σ_3 is the smallest principal effective stress; C is the cohesion; and φ is the friction angle.

Cohesion, C , and the friction angle, φ , were calculated by plotting the peak stresses at different confining stresses and drawing the best line through the data points (Figure C.2).

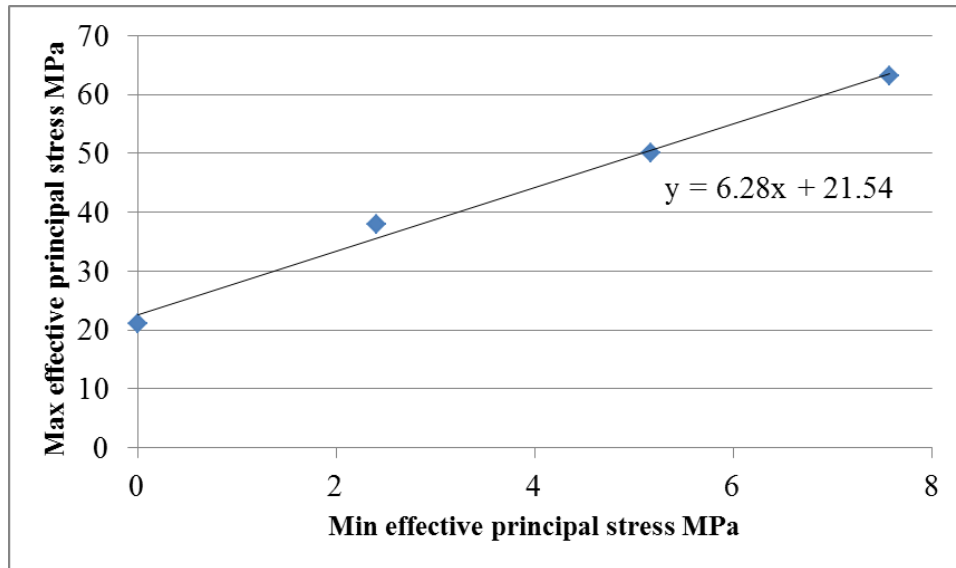


Figure C.2 Peak stresses for the base case at different confining stresses

According to Eq. (C.3)

$$\text{Slope} = \tan^2 \left(\frac{\pi}{4} + \frac{\varphi}{2} \right) \rightarrow 6.28 = \tan^2 \left(\frac{\pi}{4} + \frac{\varphi}{2} \right) \rightarrow \varphi_{base\ case} = 46.5^\circ \quad (C.4)$$

$$\text{Intercept} = 2C \tan\left(\frac{\pi}{4} + \frac{\varphi}{2}\right) \rightarrow 21.54 = 2C \tan\left(\frac{\pi}{4} + \frac{46.5^\circ}{2}\right) \rightarrow C_{base\ case} = 4.3\ \text{MPa}$$

The dilation angle is defined by (Vermeer and de Borst, 1984)

$$\sin \psi = \frac{-(\dot{\varepsilon}_1^p + \dot{\varepsilon}_2^p + \dot{\varepsilon}_3^p)}{\dot{\varepsilon}_1^p - \dot{\varepsilon}_3^p} \rightarrow \psi_{base\ case} = 5^\circ \quad (\text{C.5})$$

where ψ is the dilation angle and $\dot{\varepsilon}_1^p$, $\dot{\varepsilon}_2^p$, and $\dot{\varepsilon}_3^p$ are the plastic components of the principal strain rates.

The plastic component of the principal strain rates can be calculated by decomposing the total strain rate into the elastic and plastic parts given by

$$\dot{\varepsilon}_i = \dot{\varepsilon}_i^p + \dot{\varepsilon}_i^e \quad (\text{C.6})$$

where $\dot{\varepsilon}_i$ is the total principal strain rate and $\dot{\varepsilon}_i^e$ is the elastic component of the principal strain rate.

For simplicity, the dilation angle was calculated at the peak strength for the triaxial test at a confining stress of 2.41 MPa.

The post-peak modulus was determined using the slope of the tangent line at half way between the peak stress and the residual stress (Figure C.3). The absolute value was adopted for the ease of comparison (Cheng, 2011).

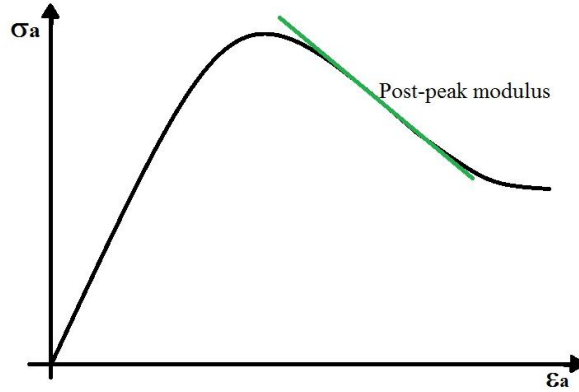


Figure C.3 Post-peak modulus

$$\text{Post-peak modulus} = \left| \frac{\Delta \sigma_a}{\Delta \varepsilon_a} \right| \rightarrow \text{post-peak modulus}_{base\ case} = 8.5\ \text{GPa} \quad (\text{C.7})$$